

**DEVELOPMENT OF A CONDUCTIVE LIGNIN-BASED CURRENT COLLECTOR
FOR WEARABLE BATTERIES**

by

Mahdiah Eghtesad

B.A.Sc., The University of British Columbia, 2018

A THESIS SUBMITTED IN PARTIAL FULFILLMENT OF
THE REQUIREMENTS FOR THE DEGREE OF

MASTER OF APPLIED SCIENCE

in

THE FACULTY OF GRADUATE AND POSTDOCTORAL STUDIES
(Materials Engineering)

THE UNIVERSITY OF BRITISH COLUMBIA
(Vancouver)

September 2021

© Mahdiah Eghtesad, 2021

The following individuals certify that they have read, and recommend to the Faculty of Graduate and Postdoctoral Studies for acceptance, a thesis entitled:

Development of A Conductive Lignin-based Current Collector for Wearable Batteries

submitted by Mahdieh Eghtesad in partial fulfillment of the requirements for

the degree of Master of Applied Science

in Materials Engineering

Examining Committee:

Prof. Frank Ko, Materials Engineering, UBC

Co-supervisor

Prof. John Madden, Electrical and Computer Engineering, UBC

Co-supervisor

Prof. Rizhi Wang, Materials Engineering, UBC

Supervisory Committee Member

Prof. Peyman Servati, Electrical and Computer Engineering, UBC

Additional Examiner

Abstract

The continuing demand for wearable electronics requires the development of lightweight and low-volume energy storage systems as the source of power. We consider the integration of a solar cell and a battery as a continuous power source for wearables. This thesis focuses only on the battery. The current collector of batteries currently used in wearables are heavy and bulky; thus, a metalized nanofibrous network is proposed to retain functionality (high electrical conductivity and support) of the current collector, while possessing lower weight and volume. Furthermore, compared to state-of-the-art lithium-ion batteries, zinc – manganese dioxide (Zn-MnO₂) batteries are of interest due to their lower cost, environmentally-friendliness, and abundance of materials.

To fabricate the metalized nanofibrous network, lignin, a natural polymer, is used as the precursor for electrospinning. The produced fibers are thermally stabilized and electroless plated with copper to meet the conductivity requirements. Finally, a layer of MnO₂ paste is brush-coated on the copper plated fibers and the electrochemical performance of the assembled Zn-MnO₂ battery is analyzed.

This work harnesses the optimization of the electrospinning solution, thermal stabilization, and electroless copper plating solution. The electrospinning solution is optimized by varying its viscosity. In general, higher viscosity results in larger diameters and fewer beads. Thermal stabilization optimization involves changing the final temperature of the process. Higher final temperature allows for more cross-linking and cleavage of bonds; however, above thermal

degradation, fiber fusion is observed. These two optimizations allow for achievement of smallest fiber diameter for lightweight and low-volume applications. The plating solution is optimized for attainment of highest conductivity, by adjusting the reducing agent amount, sonication time, and plating time. Generally, conductivity increases by increasing these parameters. However, above a certain threshold, higher formaldehyde amount reduces the reaction rate and longer sonication can break down the sample.

This lignin current collector is assessed with respect to the currently used carbon paper current collector. It is evident that lignin current collector has a higher conductivity and longer cycle life, while possessing smaller initial capacity. For wearable batteries, lifespan (cycle life) is a significant factor. Hence, the lignin current collector shows promise for wearable batteries.

Lay Summary

The power requirements of wearable electronic devices can be met by reducing the size of their battery. Here, we investigate the reduction of size of current collectors of batteries, which are the interface between the active material – material that participates in the reactions within the battery – and the external circuit. As one can expect, current collectors need to be conductive. Therefore, we designed a conductive ($> 575 \text{ S/cm}$) nanofibrous mat from a natural material called lignin. Nanotechnology can help with the size reduction. The conductivity is achieved by coating the lignin fibers with copper. Finally, a layer of active material is added to the copper coated lignin and the assembled battery is tested against the currently used current collectors. The results show the superior lifespan of lignin fibers, despite their lower initial capacity (due to higher loss). Thus, lignin current collector shows promise for wearable batteries, which require long lifespan.

Preface

The author was responsible for all designs of experiments, performing those experiments, and data analysis. The experiments were conducted on the traditional, ancestral, and unceded territory of the Musqueam people at UBC's Advanced Fibrous Materials Laboratory under the co-supervision of Prof. Frank Ko and Prof. John Madden.

Thermogravimetric analysis was performed by Diana Kim from UBC's Mehrkhodavandi group. Fourier transform infrared spectroscopy was performed by April Wu from UBC's Advanced Fibrous Materials Laboratory. X-ray diffraction data was collected by Anita Lam from UBC's Department of Chemistry. X-ray photoelectron spectroscopy data was collected and partially analyzed by Michael Wang from 4D LABS at Simon Fraser University (unceded Traditional Coast Salish Lands of the Tsleil-Waututh, Kwikwetlem, Squamish, and Musqueam Nations).

Table of Contents

Abstract.....	iii
Lay Summary	v
Preface.....	vi
Table of Contents	vii
List of Tables	xii
List of Figures.....	xiv
List of Abbreviations	xvii
Acknowledgements	xx
Dedication	xxi
Chapter 1: Motivation and Literature Review	1
1.1 Motivation.....	1
1.1.1 Energy Harvesting Systems	3
1.1.2 Energy Storage Systems	3
1.1.2.1 Battery vs. Supercapacitor	3
1.1.2.2 Current Collectors.....	5
1.2 Electrocardiograms (ECGs).....	6
1.3 Zinc – Manganese Dioxide (Zn-MnO ₂) Batteries.....	7
1.4 Metalized (Nano)fibers	8
1.4.1 Electrospinning	10
1.4.1.1 Lignin.....	12
1.4.2 Electroless Plating.....	14

1.4.2.1	Electroless Copper Plating	15
1.4.2.1.1	Catalyst for Electroless Plating	17
1.5	Objectives	18
Chapter 2: Materials and Experimental Methods.....		22
2.1	Materials	22
2.1.1	Electrospinning Solution.....	22
2.1.2	Copper Plating Solution	22
2.1.3	MnO ₂ Paste	22
2.1.4	Other Battery Components	23
2.1.5	Control Samples.....	23
2.2	Electrospinning Process	23
2.3	Thermal Stabilization Process.....	24
2.4	Electroless Copper Plating Process.....	24
2.5	Deposition of MnO ₂	25
2.6	Characterization Techniques.....	25
2.6.1	Scanning Electron Microscope (SEM)	25
2.6.2	Thermogravimetric Analysis (TGA).....	25
2.6.3	Fourier Transform Infrared Spectroscopy (FTIR)	26
2.6.4	Energy Dispersive Spectroscopy (EDS or EDX).....	26
2.6.5	X-ray Diffraction (XRD)	26
2.6.6	X-ray Photoelectron Spectroscopy (XPS)	27
2.6.7	4-Point Probe Sheet Resistance and Conductivity Measurement	27
2.6.8	Electrochemical Performance Measurement	28

2.6.8.1	Cyclic Voltammetry (CV).....	28
2.6.8.2	Galvanostatic Charge/Discharge (GCD).....	28
2.6.8.3	Electrochemical Impedance Spectroscopy (EIS).....	29
Chapter 3: Preparation of Lignin-Based Fibers for Electroless Copper Plating.....		30
3.1	Introduction.....	30
3.2	Lignin Fiber Diameter Optimization	30
3.2.1	Design of Experiments (DoE) for Diameter Optimization of 69 BCP	30
3.2.2	Diameter Optimization of 157 BCP.....	33
3.2.3	Addition of Palladium (II) Acetylacetonate (Pd(acac) ₂).....	34
3.3	Thermal Stabilization (Thermostabilization) of Lignin Fibers.....	35
3.3.1	Thermogravimetric Analysis of Lignin	36
3.3.2	Energy Dispersive Spectroscopy of Thermostabilized Lignin	38
3.3.3	Fourier Transform Infrared Spectroscopy of Thermostabilized Lignin	40
3.3.4	X-ray Diffraction of Thermostabilized Lignin	43
3.3.5	X-ray Photoelectron Spectroscopy of Thermostabilized Lignin	44
3.4	Concluding Remarks.....	46
Chapter 4: Electroless Copper Plating Optimization Based on Electrical Conductivity		
Measurements		47
4.1	Introduction.....	47
4.2	Examining Thermostability of Lignin Fibers in Electroless Plating Solution.....	47
4.3	Electroless Plating Solution Optimization of Conductivity.....	48
4.3.1	Formaldehyde Amount and Ultrasonication.....	49
4.3.2	Plating Time.....	50

4.4	Confirmation of Copper Deposition	53
4.4.1	Energy Dispersive Spectroscopy of Plated 175 °C Lignin	53
4.4.2	X-ray Diffraction of Plated 175 °C Lignin	55
4.4.3	X-ray Photoelectron Spectroscopy of Plated 175 °C Lignin	56
4.5	Concluding Remarks.....	57
Chapter 5: Deposition of MnO₂ on Copper Plated Lignin and Electrochemical		
Performance of the Lignin-based Zn-MnO₂ Battery.....59		
5.1	Introduction.....	59
5.2	Deposited MnO ₂ on Plated 175 °C Lignin.....	59
5.2.1	Energy Dispersive Spectroscopy of the Deposited MnO ₂ on Plated 175 °C Lignin	61
5.2.2	X-ray Diffraction of the Deposited MnO ₂ on Plated 175 °C Lignin	62
5.2.3	X-ray Photoelectron Spectroscopy of the Deposited MnO ₂ on Plated 175 °C Lignin	63
5.3	Electrochemical Performance of the Lignin-based Zn-MnO ₂ Battery	65
5.3.1	Cyclic Voltammetry (CV).....	65
5.3.2	Galvanostatic Charge – Discharge (GCD).....	67
5.3.3	Rate Capability.....	68
5.3.4	Cycle Life.....	69
5.3.5	Electrochemical Impedance Spectroscopy (EIS).....	71
5.3.6	Source of Loss.....	73
5.4	Concluding Remarks.....	76
Chapter 6: Conclusion and Future Work.....77		
6.1	Conclusion	77

6.2	Future Work	79
6.2.1	N.N-dimethylformamide (DMF) Alternatives	79
6.2.2	Further Weight Reduction of the Zn-MnO ₂ Battery	79
6.2.3	Solid-State Electrolyte	80
6.2.4	Higher Viscosity of Electrospinning Solution	80
6.2.5	Flexibility	80
Bibliography		81
Appendices.....		111
	Appendix A Calculation of Surface-to-Volume Ratio.....	111
	Appendix B Normalized FTIR Peak Values.....	112
	Appendix C Cross Section of Carbon Paper Coated with MnO ₂	114
	Appendix D 200 °C Cycle Life.....	115
	Appendix E Control Sample: PAN-co-MA	117
E.1	Morphology of Copper Plated PAN-co-MA.....	118
E.2	Energy Dispersive Spectroscopy of Copper Plated PAN-co-MA	118
E.3	X-Ray Diffraction of Copper Plated PAN-co-MA	120

List of Tables

Table 1.1 Sheet resistance/conductivity of some current collectors in literature. * Calculated from given thickness values in accordance to Equation 2.3 and Equation 2.4 presented in section 2.6.7.	5
Table 1.2 Comparison of lithium, zinc, and manganese. Note that abundance is given as a rank – the higher the number, the less abundant the element. Cost values are from 2018.	8
Table 1.3 Universal electrochemical mechanism. M is the metal to be plated and n is the number of charges of metal M.	15
Table 1.4 Mechanism for electroless copper plating with formaldehyde as the reducing agent. Subscription “ads” denotes adsorption of species. Adapted from reactions in ref. [117], [120]. Note that the overall reaction is achieved from $2 \times \text{Eq. 00.} + 2 \times \text{Eq. 0.} + 2 \times \text{Eq. 1.} + 2 \times \text{Eq. 2.} + 2 \times \text{Eq. 4.} + \text{Eq. 5.} + \text{Eq. 6.}$	16
Table 1.5 Influence of pH on formaldehyde reactions [125]......	17
Table 3.1 DoE for optimization of 69 BCP lignin. * The references had MW close to either 900 k or 4 M and same lignin: PEO ratio and solid content. The MW values in this thesis were chosen due to their availability in our lab. The control samples, denoted by C, provide a systematic approach to optimization.....	31
Table 3.2 EDS elemental mass % of 175 and 200 °C thermostabilized lignin.....	40
Table 3.3 FTIR band assignments for organosolv lignin [100], [111], [171]......	42
Table 3.4 Interplanar parameters of XRD plots of thermostabilized lignin at different temperatures.	43

Table 4.1 Electroless plating optimization based on formaldehyde amount and sonication time. Total plating time is 2.5 hours for all samples. The units are in Ω/\square (S/cm). The control samples, denoted by C, provide a systematic approach to conductivity optimization.	50
Table 4.2 Conductivity and sheet resistance of optimized sample (5-min sonication and 0.05 mL/mL solution of formaldehyde) for different plating times.	51
Table 4.3 EDS elemental mass % on the surface of copper plated 175 °C lignin.	55
Table 4.4 Comparison of conductivity/sheet resistance of current collectors.	58
Table 5.1 EDS elemental mass % on the surface of deposited MnO ₂ on copper plated 175 °C lignin.	61
Table 5.2 Equivalent circuit parameters.	73
Table 5.3 EDS elemental mass % on the back of deposited MnO ₂ on copper plated 175 °C lignin.	74

List of Figures

Figure 1.1. In 2005, 61% of deaths were due to chronic diseases [6]. This amount has increased to above 70% in more recent years (2019 and 2020) [4], [5]. Image from the World Health Organization – licensed under CC BY-NC-SA 3.0 IGO	1
Figure 1.2 Ragone Plot [21]. Reprinted from Supercapacitors, Chapter 2, Pandolfo <i>et al.</i> , General Properties of Electrochemical Capacitors, 72, Copyright (2013), with permission from John Wiley and Sons. Added Zn-MnO ₂ range based on ref. [22]–[24].	4
Figure 1.3. Electrospinning setup.	11
Figure 1.4 Three monomer structure within lignin [107]. Reprinted from Reactive & Functional Polymers, 85, Duval and Lawoko, A Review on Lignin-based Polymeric, Micro-and Nano-structured Materials, 79, Copyright (2014), with permission from Elsevier.	13
Figure 1.5 Proposed button structure for a wearable energy harvesting/energy storage system integrated with an electrocardiogram.....	19
Figure 1.6 Research plan.....	21
Figure 3.1 69 BCP optimization. (a) 30-95-5-900k. (b) 40-95-5-900k. (c) 30-99-1-900k. (d) 40-99-1-900k. (e) 30-95-5-4M. (f) 40-95-5-4M. (g) 30-99-1-4M. (h) 40-99-1-4M.....	32
Figure 3.2 157 BCP optimization. (a) 30-95-5-900k. (b) 30-99-1-900k. (c) 40-99-1-900k.....	34
Figure 3.3 157BCP-40-99-1-900k after addition of Pd(acac) ₂	35
Figure 3.4 TGA of 157BCP-40-99-1 with and without Pd(acac) ₂ at 10 K/min. Inset is zoomed in between 210 – 260 °C.....	37
Figure 3.5 Thermal stabilization of 157BCP-40-99-1-with-Pd(acac) ₂ at (a) 200 °C. (b) 175 °C. (c) 150 °C.....	38

Figure 3.6 EDS of 175 and 200 °C thermostabilized lignin. (a) spectrum. (b) elemental mapping of 175 °C cross section. (c) elemental mapping of 200 °C cross section. C_K α and O_K α values are from ref. [167], [168]. 39

Figure 3.7 FTIR spectrum of thermostabilized lignin at different temperatures. (a) full spectrum. (b) 1800 – 800 cm⁻¹ range, normalized based on peak 6 (the first aromatic vibration peak) – see Appendix B for exact normalized values. 41

Figure 3.8 XRD of thermostabilized lignin at different temperatures. 44

Figure 3.9 XPS of thermostabilized lignin at different temperatures. (a) survey scan. (b) Pd 3d narrow scan. O 1s, C 1s, Pd 3d values were provided by 4D LABS and confirmed through ref. [173]–[175]. 45

Figure 4.1 Stability of thermostabilized samples with 0.005 mL formaldehyde per mL of solution. (a) 150 °C. (b) 175 °C (after only 3 minutes in the solution). 48

Figure 4.2 Conductivity of lignin samples over time in optimized plating solution (5-min sonication and 0.05 mL/mL solution of formaldehyde). 51

Figure 4.3 SEM (BSE) images of copper plated 175 °C lignin after different plating times (5-min sonication and 0.05 mL/mL solution of formaldehyde): (a) 30 mins. (b) 1.5 hrs. (c) 2.5 hrs. 52

Figure 4.4 EDS mapping of copper plated on 175 °C lignin after different plating times (5-min sonication and 0.05 mL/mL solution of formaldehyde): (a) 30 mins. (b) 1.5 hrs. (c) 2.5 hrs. 53

Figure 4.5 EDS of copper plated 175 °C lignin. (a) spectrum on the surface. (b) elemental mapping of the cross section. C_K α , O_K α , Cu_L α , Au_M, Cu_K α , Cu_K β , Au_L α values are from ref. [167], [168], [186]. 54

Figure 4.6 XRD of plated 175 °C lignin. 55

Figure 4.7 XPS of plated 175 °C lignin. (a) Cu 2p narrow scan. (b) O 1s narrow scan. Cu 2p, and O 1s values were provided by 4D LABS and confirmed through ref. [188], [190]–[194].	57
Figure 5.1 SEM of deposited MnO ₂ on plated 175 °C lignin. (a) surface. (b) cross section.	60
Figure 5.2 EDS of deposited MnO ₂ on copper plated 175 °C lignin. (a) elemental mapping of the cross section. (b) spectrum on the MnO ₂ surface. C_K _α , O_K _α , Au_M, Mn_K _α , Mn_K _β , Au_L _α values are from ref. [167], [168], [186].	62
Figure 5.3 XRD of deposited MnO ₂ on plated 175 °C lignin.	63
Figure 5.4 XPS of deposited MnO ₂ on copper plated 175 °C lignin. (a) Mn 2p narrow scan. (b) O 1s narrow scan. Mn 2p, and O 1s values were provided by 4D LABS and confirmed through ref. [148], [202]–[206].	64
Figure 5.5 CV curves of lignin and carbon paper batteries at scan rate of 0.1 mV/s.	66
Figure 5.6 GCD curves of lignin and carbon paper batteries at current density of 0.1 A/g (per active MnO ₂).	67
Figure 5.7 Rate capabilities of (a) lignin battery. (b) carbon paper battery. Current densities are chosen based on ref. [149], [212] and are based on mass of active MnO ₂ .	68
Figure 5.8 Cycling performance of (a) lignin battery. (b) carbon paper battery. at 200 mA/g (per active MnO ₂).	70
Figure 5.9 EIS of lignin and carbon paper batteries. Inset is zoomed in to about 500 Ω on the real axis.	72
Figure 5.10 Equivalent circuit for fitting to EIS data.	72
Figure 5.11 EDS elemental mapping of the back side of deposited MnO ₂ on copper plated 175 °C lignin.	75

List of Abbreviations

ABC3D: Advanced BioCarbon 3D

BSE: Backscatter Electrons

$C_4H_4KNaO_6 \cdot 4H_2O$: Potassium Sodium Tartrate Tetrahydrate

CH_2O : Formaldehyde

Cu_2O : Copper (I) Oxide

CuO : Copper (II) Oxide

$CuSO_4 \cdot 5H_2O$: Copper (II) Sulfate Pentahydrate

CV: Cyclic Voltammetry

DMF: N,N-dimethylformamide

DoE: Design of Experiment(s)

ECG: Electrocardiogram

EDS: Energy Dispersive Spectroscopy

EDX: Energy Dispersive Spectroscopy

EIS: Electrochemical Impedance Spectroscopy

FTIR: Fourier Transform Infrared Spectroscopy

G unit: Guaiacyl

GCD: Galvanostatic Charge – Discharge

H unit: p – hydroxyphenyl

ITO: Indium Tin Oxide

LiCl: Lithium chloride

Li-ion: Lithium-ion

MnO₂: Manganese (IV) oxide

MnSO₄·H₂O: Manganese (II) Sulfate Monohydrate

MW: Molecular Weight

NaOH: Sodium Hydroxide

NMP: 1-Methyl-2-pyrrolidinone

PAN-co-MA: Polyacrylonitrile-co-methyl-acrylate

Pd(acac)₂: Palladium (II) acetylacetonate

Pd(C₅H₇O₂)₂: Palladium (II) acetylacetonate

Pd: Palladium

PEO: Poly (ethylene oxide)

PVA: Polyvinyl Alcohol

PVDF: Poly (vinylidene fluoride)

S unit: Syringyl

SEM: Scanning Electron Microscope/Microscopy

TGA: Thermogravimetric Analysis

Thermostabilization: Thermal Stabilization

TiO₂: Titanium Dioxide

WHO: World Health Organization

XPS: X-ray Photoelectron Spectroscopy

XRD: X-ray Diffraction

ZnCl₂: Zinc Chloride

Zn-MnO₂: Zinc – Manganese Dioxide

ZnSO₄·7H₂O: Zinc Sulfate Heptahydrate

Acknowledgements

I would like to offer my enduring gratitude to Prof. Frank Ko for bringing me into the Advanced Fibrous Materials Laboratory and supporting me, Dr. Addie Bahi for continued support, Prof. John Madden for continued guidance, Dr. Tan Nguyen and Bahar Iranpour for training me in performing electrochemical tests and making MnO₂ paste blend, Dr. Saeid Soltanian for allowing me to use the 4-point probe electrical conductivity measurement tool and electrochemical testing station in the Centre for Flexible Electronics and Textiles Laboratory, Katherine Le for training me in measuring conductivity using the 4-point probe, UBC's Composites Research Network for permitting me to use the furnace, Li-Ting Lin for showing me how to operate the tube furnace, Heli Eunike for permitting me to use the scanning electron microscope, Anita Lam for collecting X-ray diffraction data, Michael Wang for collecting X-ray photoelectron spectroscopy data, and Dr. Elham Zabihi for continued support and guidance. This research would not be possible without the supplier of lignin, Advanced BioCarbon 3D and its CEO, Darrel Fry.

I would like to thank my colleagues, Diana Kim for performing thermogravimetric analysis, April Wu for performing Fourier transform infrared spectroscopy, Delphine Rey and Safoora Khosravi for their continued support, and all members of the Advanced Fibrous Materials Lab for their support and guidance.

Special thanks to my family and friends for their support and keeping me sane during the rough times!

Dedication

To my sister, dad, and mom, without whom I might not have survived the past two years to write this thesis.

Chapter 1: Motivation and Literature Review

1.1 Motivation

With the advancement of treatments for acute illnesses, individuals are more likely to live longer, which in turn increases the possibility of developing chronic illnesses [1]. Chronic illnesses are one of the most common and costly of all health problems; however, they are the most preventable [2]. In Canada, two-thirds of all deaths are due to one of the following major chronic diseases: cardiovascular diseases, cancer, chronic respiratory diseases, and diabetes [3]. Moreover, the World Health Organization (WHO) reported that 60 – 70% of all global deaths are due to these chronic diseases (Figure 1.1) [4], [5]. Thus, chronic disease prevention and management have become important challenges.

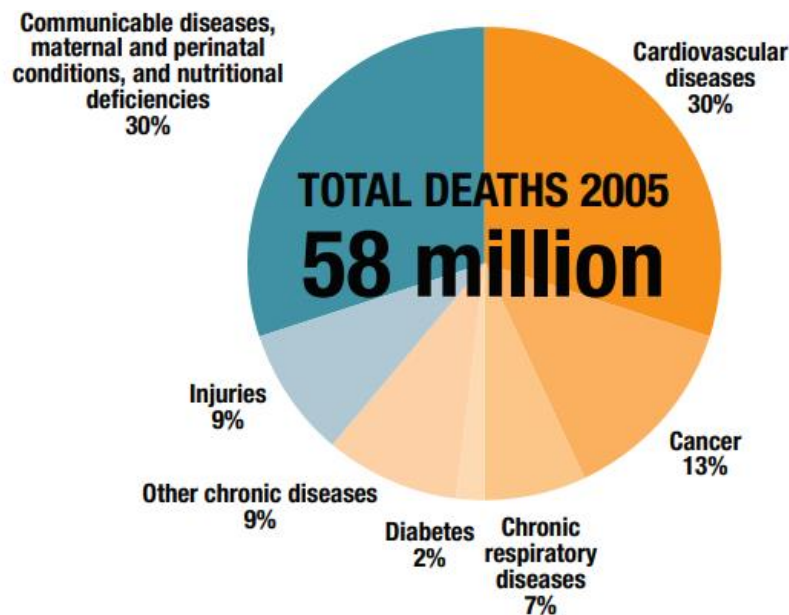


Figure 1.1. In 2005, 61% of deaths were due to chronic diseases [6]. This amount has increased to above 70% in more recent years (2019 and 2020) [4], [5]. Image from the World Health Organization – licensed under [CC BY-NC-SA 3.0 IGO](https://creativecommons.org/licenses/by-nc-sa/3.0/).

Wearables with real-time and continuous monitoring can help prevent, delay, or reduce the aggravation of chronic diseases [1], [6]. Moreover, having a smart energy system which includes both energy harvesting and energy storage is essential for these continuously monitoring wearables [7]. Solar energy can be a no-cost source for the harvesting system (see section 1.1.1). For energy storage systems, because of the proposed structure in section 1.5 and the continuity requirement for power, batteries are chosen (see sections 1.1.2 and 1.1.2.1). As for choices of batteries, one can start by looking at the state-of-the-art lithium-ion (Li-ion) batteries. Li-ion batteries, unfortunately, use organic electrolytes, which are flammable and can cause safety issues. Aqueous batteries, on the other hand, are free of such safety issues. However, a new problem arises when considering aqueous batteries. Present aqueous batteries use current collectors that are heavy and bulky [8], [9]. More specifically, the batteries in wearables have two main issues: (a). limited lifespan due to quick drainage of their energy, and (b). lack of lightweight solutions [10]. Thus, to overcome these issues and create a continuous monitoring system, we need to reduce the size of the current collector, while maintaining its functionality (high electrical conductivity and support for active material [11]), as well as integrating with energy harvesting systems. In this thesis, we aim to develop a conductive ($> 575 \text{ S/cm}$ – section 1.1.2.2), lightweight, and low-volume (through nanofibrous structure – sections 1.4) current collector from natural sources (i.e., lignin – section 1.4.1.1). Furthermore, since the largest percentage of deaths due to chronic disease ($\sim 30\%$) is caused by cardiovascular diseases (Figure 1.1), wearable electrocardiogram is chosen as a potential application.

1.1.1 Energy Harvesting Systems

Several energy sources can be considered for powering wearable devices, such as solar, mechanical (triboelectric, piezoelectric, and electromagnetic sources), thermal (e.g., temperature of body), chemical (e.g., biofuel cells), and radio frequency energy [12], [13].

Solar energy in particular is interesting, because it is said that “the amount of energy supplied to the Earth in one day by the sun is sufficient to power the total energy needs of the Earth for one year” [14]. However, solar energy is intermittent, unreliable, and depends on weather conditions. For these reasons, solar energy needs to be stored in an energy storage system [15].

1.1.2 Energy Storage Systems

One can start narrowing down the specific energy storage system, given that a suitable, lightweight, and low-volume energy storage system is vital to advancement of wearables [8], [9], [16]. For wearable/electronic textile applications, it seems reasonable to look at small-scale electrical energy storage systems. Such energy storage systems include batteries, supercapacitors, and hydrogen fuel cells [17]. Fuel cells require continuous flow of fuel [17], which is challenging to employ, considering the proposed structure in section 1.5; thus not valid for this wearable application. The following section further analyzes the choice between batteries and supercapacitors.

1.1.2.1 Battery vs. Supercapacitor

Supercapacitors and batteries are both dependent on electrochemical processes; however, the mechanisms in each result in different power/energy densities. Batteries provide long-term

power to devices (i.e., high energy density), as opposed to supercapacitors, where short-term power is delivered (i.e., high power density) [18], [19]. Figure 1.2 is a Ragone plot (specific energy vs. specific power plot) illustrating the difference in energy and power densities of batteries and supercapacitors. For this research, where continuous power is to be delivered to the wearable system, batteries are the obvious choice. The ideal case is to charge the system while the sun is shining and discharge the battery between sunset and sunrise. The time between sunset and sunrise varies depending on location; for instance, in Vancouver, BC, Canada, the longest night took about 16 hours during the winter solstices of 2020 [20].

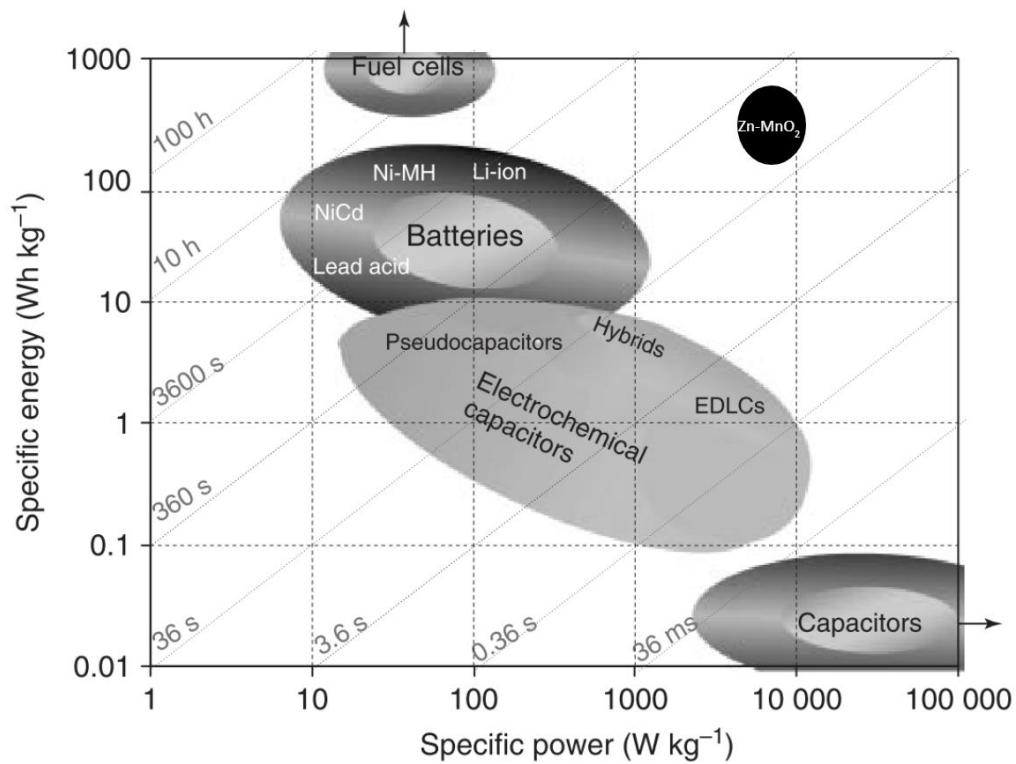


Figure 1.2 Ragone Plot [21]. Reprinted from Supercapacitors, Chapter 2, Pandolfo *et al.*, General Properties of Electrochemical Capacitors, 72, Copyright (2013), with permission from John Wiley and Sons. Added Zn-MnO₂ range based on ref. [22]–[24].

Batteries generally consist of anode, cathode, electrolyte, separator, and current collectors, where anode and cathode are supported [25]. The anode is oxidized and loses electrons, while the cathode is reduced and gains electrons (during discharge). The electrolyte is the ionic conductor, which allows the ions to move between the two electrodes. The separator prevents internal short-circuiting by separating the anode and cathode electrodes [26] (see section 1.1.2.2 for more information on current collectors).

1.1.2.2 Current Collectors

Current collectors' main roles are: (a) to support the active materials, and (b) to electrically connect the electrodes to the external circuit (i.e. gather/supply electrons from/to electrodes) [27]–[29]. Traditionally, current collectors have been viewed as dead weight (i.e., limited power/energy density) and only recently research has grown to explore performance improvement through current collectors [29]–[31]. According to the role of current collector, high conductivity (low sheet resistance; see section 2.6.7 for calculation of the two parameters) and efficient electron transport of current collectors can improve the batteries' performance [29]. Table 1.1 includes a list of current collector materials and their sheet resistance.

Table 1.1 Sheet resistance/conductivity of some current collectors in literature. * Calculated from given thickness values in accordance to Equation 2.3 and Equation 2.4 presented in section 2.6.7.

Current Collector Material	Sheet resistance	Ref
Conformal coating of CNT and Ag nanowire on paper	$1 \frac{\Omega}{\square}$	[32]
Reduced graphene oxide film on polyethylene naphthalate substrate	$1.28 \frac{\Omega}{\square}$	[33]

Indium tin oxide (ITO) nanowires array	$0.34 \frac{\Omega}{\square}$	[34]
Double-walled carbon nanotube on polyethylene naphthalate paper	$5 \frac{\Omega}{\square}$	[35]
Ag microflakes on CNT/carbon black/poly(styrene)-block-poly(ethylene-ran-butylene)-block-poly(styrene) composite	$2.7 \frac{\Omega}{\square}$	[36]
CNT film	$5 \frac{\Omega}{\square}$	[37]
100 layers of superaligned carbon nanotube	$11 \frac{\Omega}{\square}$	[38]
Al coated on CNT film by electron-beam evaporation	$0.33 \frac{\Omega}{\square}$	[39]
Reduced graphene oxide nanosheets	$0.8 \frac{\Omega}{\square}$	[9]
Ultrathick 3D carbon framework	$1.1 * \frac{\Omega}{\square} (13.75 \frac{S}{cm})$	[40]
Carbon nanotube/cellulose nanofiber composite	$0.575 * \frac{\Omega}{\square} (575 \frac{S}{cm})$	[8]

To the best of our knowledge, no literature focuses on developing current collectors produced from environmentally friendly and sustainable materials, while having low-volume and lightweight. We propose a nanofibrous lignin-based (see section 1.4) current collector to fill this knowledge gap.

1.2 Electrocardiograms (ECGs)

ECG is a test, which measures the electrical activity of the heartbeat. With each heartbeat, an electrical impulse travels through the heart causing the heart to squeeze and inject blood. ECGs

can help detect abnormalities and monitor heart-related recovery [41], [42]. To the best of our knowledge, wearable ECGs use Li-ion batteries [43]–[45]. Li-ion batteries have an energy density of 100 – 265 Wh/kg (per mass of cell) and cycle life of around 300-500 cycles [46], [47]. In addition, commercial Li-ion batteries have a capacity of around 310 mAh/g (per mass of lithium anode at C/5 rate [48]). To be able to develop more environmentally cautious solutions for batteries, which also satisfy power requirements of ECGs, we considered Zn-MnO₂ batteries in this work (see section 1.3). Here, wearable ECGs are a potential application for the continuous energy harvesting/storage integrated system.

1.3 Zinc – Manganese Dioxide (Zn-MnO₂) Batteries

As previously mentioned, Li-ion batteries can be flammable and unsafe. Table 1.2 further illustrates the disadvantages of lithium (i.e., high cost and low abundance). Moreover, for extraction of every tonne of lithium from underground reservoirs, 469 m³ of drinking water is needed. Toxic chemicals are also required in lithium production. Hence, lithium is considered environmentally costly [49]–[51]. In this research, to fabricate a safer, more abundant, less costly, and more environmentally friendly battery, Zn-MnO₂ battery is chosen [23], [26], [52]. Primary and rechargeable alkaline Zn-MnO₂ batteries have been developed commercially. For purposes of this thesis, primary batteries (non-rechargeable [26]) are avoided, since the solar cell is to charge the battery for a continuous source of power. The rechargeable alkaline Zn-MnO₂ battery suffers from zinc corrosion in the alkaline electrolyte, irreversible reduction of MnO₂, and environmental unfriendliness of the alkaline electrolyte [23], [53]. Neutral/mild(ly acidic) aqueous Zn-MnO₂ batteries are considered here due to their safe nature and inexpensiveness [23], [54].

Table 1.2 Comparison of lithium, zinc, and manganese. Note that abundance is given as a rank – the higher the number, the less abundant the element. Cost values are from 2018.

Element	Abundance	Cost	Ref
Lithium	33	\$16,500.00 / metric ton	[55]–[58]
Zinc	25	\$2,573.40 / metric ton	[55]–[57], [59]
Manganese	12	\$2,060.00 / metric ton	[55]–[57], [60]

Zn-MnO₂ battery uses zinc as anode and MnO₂ as cathode during discharge. These batteries have been shown to have high enough energy density and capacity that meets the ECGs requirements. For instance, Zhang *et al.* [24] reports a Zn-β-MnO₂ with 158.5 Wh/kg energy density (225 mAh g⁻¹ capacity at 0.2 A g⁻¹). Chao *et al.* [52], more recently, has been able to achieve an energy density of 409 Wh/kg (capacity of 570 mAh g⁻¹ at ~0.6 A g⁻¹) for high voltage (1.7 – 2 V Zn⁺²/Zn) region Zn-MnO₂ (energy densities are based on active material of anode and cathode and capacities are based on active MnO₂).

1.4 Metalized (Nano)fibers

To address the roles of current collectors (i.e., high conductivity and supportive structure), we consider metalized nanofibers. Metalized nanofibers provide a way towards hybrid nanomaterials, which allows one to combine properties of organic polymers, which are one of the most frequently utilized materials in nanofibers [61], with inorganic metals [62]. This combination can benefit from the high surface-to-volume ratio of nanofibers [63], [64] as well as the high conductivity of metals [63]. Nanofibers – defined as fibers (aspect ratio > 1000:1) with diameter below 1 μm [65] – serve as a supportive network for active material of the battery. To understand the high surface-to-volume ratio associated with nanofibers, consider transitioning

from a cube with 1 cm sides to 10^{21} cubes with 1 nm sides (same volume). The surface area of the second cube would increase by a factor of 10^7 (see Appendix A for derivation) [66]. With high surface-to-volume ratio, low-volume applications are possible. In addition, nanomaterials can produce lightweight structures to replace the traditional heavy ones [67]–[69]. Another advantage of nanofibers with high surface-to-volume ratio is their enhanced reactivity [65], which would help with electroless plating. Hence, metalized nanofibers have the potential to provide a conductive, low-volume, and lightweight structure as the current collector providing support for the active material of batteries.

Metalized nanofibers have vast applications, such as transparent conducting electrodes, filtration, artificial muscles, antibacterial and antimicrobial coatings, electromagnetic interference shielding, endovascular coil material, active material or current collector in energy storage systems, anti-static agent, etc. [63], [70]–[78]. Transparent conducting electrodes have been produced from copper electroplated polyacrylonitrile nanofibers with improved performance due to removal of junction resistance at the intersection of wires [75]. Zeolite/palladium coated on polyacrylonitrile-co-methyl-acrylate nanofibers have been shown to function as an ammonia filter [76]. In a recent study by Ebadi *et al.* [63], polyurethane nanofibers electroplated with copper were used to enhance the actuation performance of artificial muscles. Phan *et al.* [73] studied the antibacterial influence of silver-polyacrylonitrile nanofiber composites against *Escherichia coli* and *Bacillus subtilis*. Ji *et al.* [71] investigated the high-performance electromagnetic interference shielding effect of electroless plated and crosslinked polyacrylonitrile, where the metalized nanofiber outperformed the pure metal foil and most synthesized shielding materials. Platinum coated polyacrylonitrile nanofibers have shown great

promise as endovascular coil material for preventing extravasation of blood after aneurysmal subarachnoid hemorrhage [74]. Studies have illustrated that nickel/carbon composite (from carbonized polyacrylonitrile or polyacrylonitrile/polyvinyl pyrrolidone) can be used as the active material in supercapacitors [77], [78]. Lastly, nickel coated polyacrylonitrile-co-methyl-acrylate nanofibers have been studied as current collectors for pseudocapacitors [72].

Furthermore, metalized fibers are also commercially available. For instance, X-STATIC® yarns and threads benefit from anti-static property of silver bonded nylon fibers [79]. AgFlex, an Indian company focused on developing silver-based solutions, produces fine chopped silver-coated nylon fibers for antibacterial protection [80]. Ionic+™ combines the antibacterial effect of silver ions with nylon, cotton, wool, polyester, acrylic, and other fibers [81]. ARACON® fibers are silver- or nickel-plated KEVLAR® used as electromagnetic and radio frequency interference shields [82].

In this work, metalized fibers are used as the current collector of batteries to replace the heavy and bulky current collectors currently employed in wearables. Electrospinning and electroless plating methods for fabrication of these metalized fibers are discussed in sections 1.4.1 and 1.4.2.

1.4.1 Electrospinning

There are several techniques that can produce nanofibers, such as chemical vapor deposition (reaction/decomposition of volatile precursor on a substrate), self-assembly (self-arrangement of pre-existing components into desired patterns and functions), template synthesis (use of nanoporous membrane as template), and electrospinning [83]. Electrospinning is chosen in this

research due to its wide range of benefits, including: large scale nanofiber production [84], [85], simplicity [72], robustness [86], and low-cost [87], [88]. Electrospinning can produce fibers that are a few nanometers (2 nm) to several microns (10 μm) in diameter [83], [86], [89].

A typical electrospinning setup involves: a syringe with a metallic needle filled with polymer solution, syringe pump, high voltage supply, and a grounded metallic target/collector (Figure 1.3) [72]. An electric field forms between the high voltage supply connected to the needle and the grounded target. Once the electrospinning process starts, a droplet of polymer solution at the tip of the needle transforms to a hemispherical shape. If one applies a high voltage such that the intensity of the electric field overcomes the influence of surface tension of the polymer solution, the hemispherical shape turns into a cone-shape (Taylor cone) and a uniform jet of solution is ejected towards the target. The cone-shaped jet is stretched and elongated by electrically induced bending instabilities [90]. Solvent quickly evaporates during elongation, thus reducing the fiber diameter, and the nonwoven fiber mat can be collected on the target [83], [87], [91].

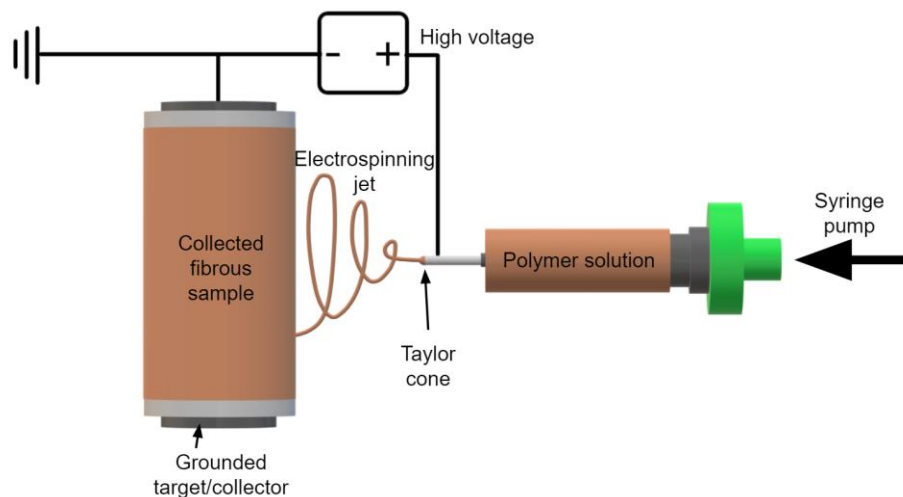


Figure 1.3. Electrospinning setup.

Multifunctional composite nanofibers can be derived from mixing functional compounds into the polymer/electrospinning solution [72], [92]. For instance, carbon nanotubes have been shown to enhance mechanical [87], [91] and electrical [93] performance of lignin and polyacrylonitrile nanofibers. TiO₂ can be added to polyacrylonitrile nanofibers to improve the photocatalytic behavior [94], [95]. In bone tissue engineering applications, hydrophilicity of poly(vinyl alcohol) nanofibers can be improved by adding nanohydroxy apatite and cellulose nanofibers [96]. Palladium (II) acetylacetonate added to polyacrylonitrile-co-methyl-acrylate can act as a catalyst for electroless plating [72]. In this thesis, the latter method is used for lignin to improve the catalytic behavior while plating (see section 1.4.2 for more information on plating).

1.4.1.1 Lignin

Lignin is the second most abundant natural polymer, surpassed only by cellulose; however, unlike cellulose, lignin has not been adapted in large-scale value-added products. It is considered to be the major biorenewable source of aromatic functionality [97]–[99]. Lignin facilitates water and solute transfer by providing hydrophobicity to the plant vascular system [100], [101].

Furthermore, lignin gives rigidity to the cell wall, ensures resistance to bending, compression, and impact, and provides resistance against chemical and biological degradation by microorganisms [101]–[104].

Lignin is an attractive precursor for carbonous structure due to its low cost, abundance, high carbon content (around 60 wt%, as opposed to 44% for cellulose [105]), and lack of toxic byproducts during heat treatment [98], [99]. Additionally, much of the extracted lignin during production of cellulose for the paper industry is regarded as waste or burnt as low-value-added

fuel. Less than 2% of the 70 million ton of extracted lignin is used as concrete additives, stabilizing agents or dispersants, surfactants, and adhesives [98], [100], [104].

Lignin is an amorphous, heterogenous, and aromatic biopolymer. It is created from polymerization of three phenylpropane monomers: coniferyl, sinapyl, and p-coumaryl alcohols; where in the lignin structure, these are termed as guaiacyl (G), syringyl (S), and p-hydroxyphenyl (H) units, respectively (Figure 1.4) [87], [98], [100], [101], [104], [106]. The configuration of these units within lignin depends on plant species and environment [98]. Softwood lignin comprises of G units and low levels of H units, while hardwood lignin consists of equal amounts of G and S units, and small amounts of H units [98]–[100], [106]. In this thesis, hardwood lignin is used (see section 3.3.3 for FTIR peaks of G, S, and H units).

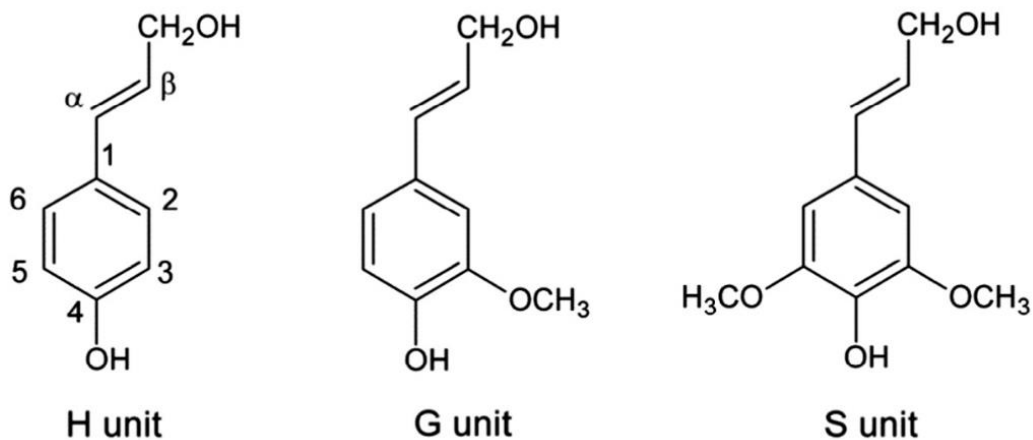


Figure 1.4 Three monomer structure within lignin [107]. Reprinted from *Reactive & Functional Polymers*, 85, Duval and Lawoko, A Review on Lignin-based Polymeric, Micro- and Nano-structured Materials, 79, Copyright (2014), with permission from Elsevier.

Compared to the highly condensed softwood lignin structure, hardwood lignin is considered to possess higher spinnability [108], [109]. In addition, several techniques can be employed to

extract lignin from various biomass feedstock, such as kraft, organosolv, lignosulfonate, alkali (soda), etc. Organosolv process is considered the most straightforward, economically promising, and eco-friendly [98], [100], [106], [110], [111]. Compared to the kraft process – which is dominant in pulp and paper processes due to high yield of pulp (90 kt per year), pulp strength, and chemical recovery [107], [112] – organosolv lignin, with its high purity and low sulfur content [100], [106], allows for better spinnability [113]–[115]. Therefore, for this thesis, hardwood organosolv lignin is studied as the current collector precursor.

1.4.2 Electroless Plating

Electroless plating or autocatalytic metal plating is a method for deposition from solution without a need for power supply [116], [117]. The minimum requirements for such solutions are a metal salt and a suitable reducing agent [116], [118]. The history behind electroless plating is not clear. Some argue that the first electroless solution was used for silvering glass mirrors [118], while others believe that such homogeneous chemical reduction is not considered electroless plating [116]. If we add the requirement of a suitable catalyzed surface to our definition, the former argument is no longer valid. In such cases, plating is initiated by the catalyst and sustained by the plated metal itself [116]. Therefore, spontaneous plating on all surfaces (e.g., silver mirroring) is not electroless plating. In any case, the first commercial electroless copper plating was used for printed circuits in the 1950s [116], [118]. For the purposes of this research, having a catalyst is a requirement.

One should note that electroless plating is slower and more expensive than electroplating; hence, it is only used when unique properties are required, such as even thickness on complex surfaces

and deposition on non-conductors [116], [119]. Here, electroless plating is chosen due to its ability to evenly coat complex (non-woven) and non-conductive lignin fibers.

Van Den Meerakker [117], [120] proposed the universal electrochemical mechanism for any reducing agent, R, as illustrated in Table 1.3.

Table 1.3 Universal electrochemical mechanism. M is the metal to be plated and n is the number of charges of metal M.

Anodic reactions in alkaline solution	1. Dehydrogenation:	$RH \rightarrow \dot{R} + \dot{H}$
	2. Oxidation:	$\dot{R} + OH^- \rightarrow ROH + e$
	3. Recombination:	$\dot{H} + \dot{H} \rightarrow H_2$
	4. Oxidation:	$\dot{H} + OH^- \rightarrow H_2O + e$
Cathodic reactions in alkaline solution	5. Metal deposition:	$M^{n+} + ne \rightarrow M$
	6. Hydrogen evolution:	$2H_2O + 2e \rightarrow H_2 + 2OH^-$

For this research, we will narrow the abovementioned generalization to the specific case for copper.

1.4.2.1 Electroless Copper Plating

Copper is the second most conductive metal (5.96×10^5 S/cm at 20 °C); surpassed only by silver (6.3×10^5 S/cm) [121], [122]. Compared to silver, copper is less expensive [123]. Due to its high conductivity and reasonable price, copper is the material of choice for electroless plating in this research.

For electroless copper plating, a copper salt (e.g. copper sulfate) and a reducing agent (e.g. formaldehyde, dimethylamine borane, borohydride, glyoxylic acid, etc.) are needed [116], [120], [124]. Despite the environmental issues of formaldehyde, it is the chosen material in commercial settings due to its effectiveness and low cost [116]. Glyoxylic acid has been shown to serve as a more environmentally friendly reducing agent [124]. In this research, we follow the commercial standard of using formaldehyde. One can re-write the reactions in Table 1.3 for the specific case of formaldehyde and copper, as shown in Table 1.4. Note that Eq. 3 and 4 in Table 1.3 are competing reactions. The pH and type of metal determine which reaction proceeds [120]. For the case of copper, desorption of adsorbed hydrogen occurs on deposited copper surface [117].

Table 1.4 Mechanism for electroless copper plating with formaldehyde as the reducing agent. Subscription “ads” denotes adsorption of species. Adapted from reactions in ref. [117], [120]. Note that the overall reaction is achieved from (2 × Eq. 00.) + (2 × Eq. 0.) + (2 × Eq. 1.) + (2 × Eq. 2.) + (2 × Eq. 4.) + Eq. 5. + Eq. 6..

Anodic reactions	00. Hydrolysis of formaldehyde:	$H_2CO + H_2O \rightarrow H_2C(OH)_2$
	0. Dissociation of methylene glycol:	$H_2C(OH)_2 + OH^- \rightarrow H_2C(OH)O^- + H_2O$
	1. Dissociative adsorption:	$H_2C(OH)O^- \rightarrow [HC(OH)O^-]_{ads} + H_{ads}$
	2. Oxidation:	$[HC(OH)O^-]_{ads} + OH^- \rightarrow HCOO^- + H_2O + e$
	4. Desorption of adsorbed hydrogen on copper surface:	$H_{ads} + OH^- \rightarrow H_2O + e$
Cathode reaction	5. Metal deposition:	$Cu^{2+} + 2e \rightarrow Cu$
	6. Hydrogen evolution:	$2H_2O + 2e \rightarrow H_2 + 2OH^-$
Overall	$Cu^{2+} + 2H_2CO + 4OH^- \rightarrow Cu + 2HCOO^- + 2H_2O + H_2$	

When considering formaldehyde as the reducing agent, higher pH results in higher reduction potential [117] (Table 1.5).

Table 1.5 Influence of pH on formaldehyde reactions [125].

Reaction	pH	Standard half-cell potential
$HCOOH + 2H^+ + 2e \leftrightarrow HCHO + H_2O$	0	+ 0.056 V vs. SHE
$HCOO^- + 2H_2O + 2e \leftrightarrow HCHO + 3OH^-$	14	- 1.070 V vs. SHE

Given that the standard half-cell potential of the cathodic reaction $Cu^{2+} + 2e \rightarrow Cu$ is + 0.340 V vs. SHE [125], to have a more spontaneous and more thermodynamically favorable electrochemical reaction ($\Delta_{cell}G^0 < 0$ or $\Delta_{cell}E^0 > 0$), higher pH levels are desirable ($\Delta_{cell}E^0 = E_{cathode}^0 - E_{anode}^0 = 0.34 - (-1.07) = 1.41$ V). To achieve a higher pH, one can add an alkali salt, such as sodium hydroxide. However, in high pH levels, copper precipitates; thus complexants (e.g. sodium potassium tartrate, ethylenediamine tetraacetic acid, etc.) are added [125]. Complexants lower the free metal ion concentration [125], [126]. Nonetheless, the concentration of complexant should be carefully determined, otherwise, there will not be sufficient metal ions for deposition [125]. Tartrate salts are used for low-plating rate ($\leq \frac{0.5\mu m}{20 \text{ min}}$) and near room temperature settings. Tartrates allow for easier waste treatment as well [116]. For this application, sodium potassium tartrate is chosen as the complexant.

1.4.2.1.1 Catalyst for Electroless Plating

Electroless plating only initiates in presence of hydrogenation-dehydrogenation catalysts (as per the definition in section 1.4.2) [118], [120]. Earlier reports believe that palladium metal is the most efficient dehydrogenation catalyst [118], [120]. However, more recent papers (for copper plating, specifically) [124], [127] state that less expensive options (e.g., silver) are available. For

purposes of this research, palladium is chosen as the catalyst, since it has been the traditional catalyst of choice and has been shown to work with nanofibrous structures [72].

Traditionally, catalysts are introduced to the surface in 2 steps: (1) applying a stannous chloride/hydrochloric acid solution to the surface and then (2) immersion in palladium chloride/hydrochloric acid solution. These two steps result in the following reaction (Equation 1.1), which produces palladium metal.



More recently, the 2 steps are combined, and a solution of stannous chloride, palladium chloride, and hydrochloric acid is used [128]. In this research, however, the immersion method in colloidal particle solution may result in uneven and non-uniform plating [72]. Therefore, less expensive palladium (II) acetylacetonate (compared to palladium chloride) is added to the electrospinning solution directly to create a multifunctional metal fiber (see section 2.2 for the method).

1.5 Objectives

This research is part of a series of projects involving integration of an energy harvesting system (i.e., perovskite solar cell) and an energy storage system (i.e., Zn-MnO₂ battery) assembled on top of a button, with a wearable electrocardiogram (Figure 1.5). With a focus on batteries as the energy storage system, the goal of this thesis is to develop a lightweight, low-volume, and conductive current collector from copper plated lignin fibers.

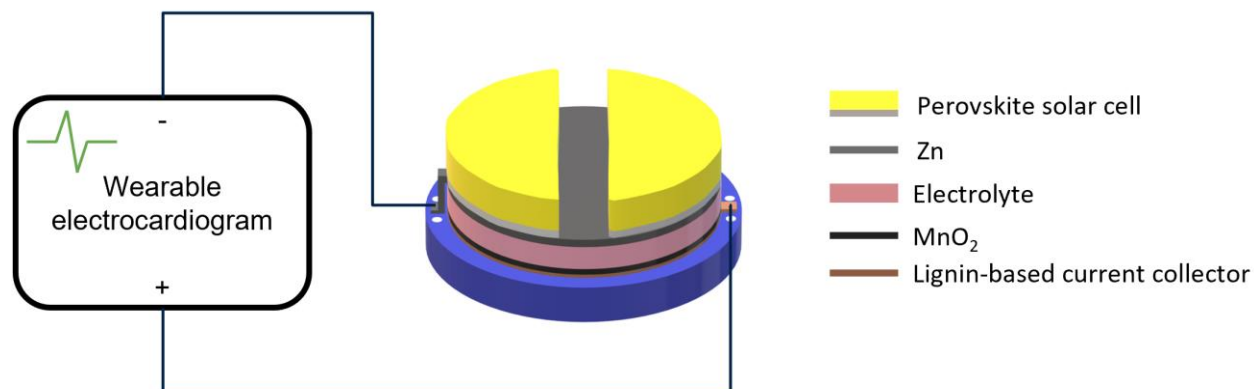


Figure 1.5 Proposed button structure for a wearable energy harvesting/energy storage system integrated with an electrocardiogram.

The nanofibrous structure of lignin serves as the support of the current collector with high surface-to-volume ratio, which helps with reduction of volume and weight. In addition, the copper coating allows for a conductive surface. Specifically, as shown in Figure 1.6, the objectives of this work are:

1. To investigate and optimize the electrospinning process of hardwood organosolv lignin using factorial design of experiments (DoE) for three electrospinning parameters: plasticizer molecular weight, lignin: plasticizer ratio, and solid content to fabricate fibers with smallest diameter, which result in the highest surface-to-volume ratio. These parameters influence the viscosity of the polymer solution. Viscosity is one of the main factors of influence on fiber diameter during electrospinning [83], [87].
2. To optimize the thermal stabilization process after the integration of palladium (II) acetylacetonate – the catalyst precursor for electroless copper plating – into the fibers during electrospinning. This diameter optimization is done by characterization using

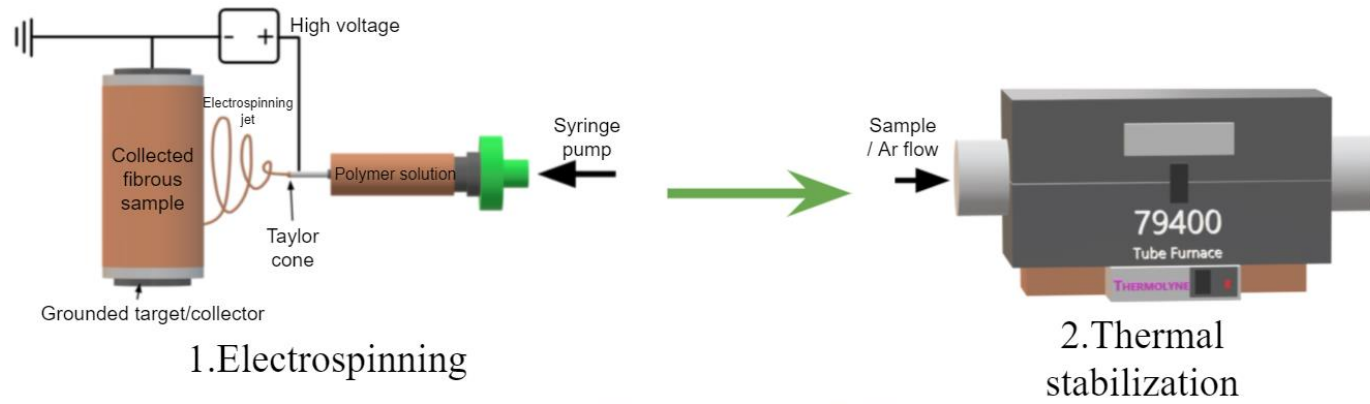
scanning electron microscopy (SEM) and visually inspecting the chemical stability in the plating solution.

3. To evaluate whether lignin can be plated and optimize the electroless plating solution using a factorial experimental design of two parameters: sonication time and amount of formaldehyde (i.e., reducing agent). The solution is optimized by measuring the sheet resistance/conductivity. Plating time also plays a role in conductivity; thus, it is lastly optimized.
4. To deposit MnO_2 on the plated lignin by brush-coating, and
5. To assess the current collector's electrochemical performance within a Zn- MnO_2 battery.

The chemical/crystal structure and morphology of lignin samples are studied and characterized after thermal stabilization, copper plating, and deposition of MnO_2 using scanning electron microscopy (SEM), energy dispersive spectroscopy (EDS), Fourier transform infrared spectroscopy (FTIR), X-ray diffraction (XRD), and X-ray photoelectron spectroscopy (XPS).

The electrochemical performance of the assembled battery is studied using cyclic voltammetry (CV), galvanostatic charge discharge curves (GCD), and electrochemical impedance spectroscopy (EIS).

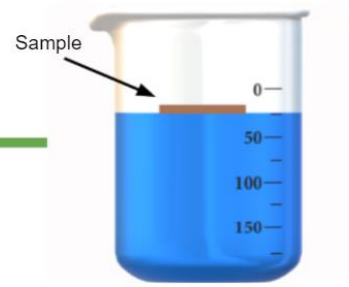
Chapter 3



1. Electrospinning

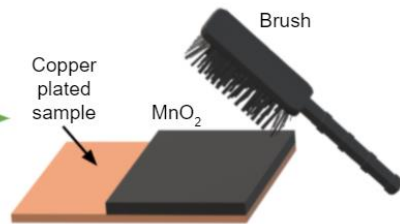
2. Thermal stabilization

Chapter 4

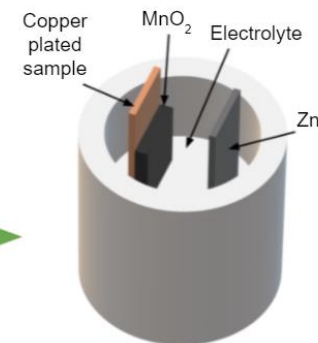


3. Electroless copper plating

Chapter 5



4. MnO₂ deposition (Brush-coating)



5. Battery assembly

Figure 1.6 Research plan.

Chapter 2: Materials and Experimental Methods

2.1 Materials

2.1.1 Electrospinning Solution

Hardwood organosolv lignin was supplied by the sponsor of this thesis, Advanced BioCarbon 3D (ABC3D). The received lignin was dried at 50 °C overnight to remove moisture. Poly (ethylene oxide) (PEO) with approximate molecular weights of 900 k and 4 M g/mol were purchased from Scientific Polymer Products Inc., used as received, and served as plasticizer. N,N-dimethylformamide (DMF) was obtained from Sigma-Aldrich. Palladium (II) acetylacetonate ($\text{Pd}(\text{C}_5\text{H}_7\text{O}_2)_2$ or $\text{Pd}(\text{acac})_2$) was obtained from Aladdin.

2.1.2 Copper Plating Solution

Copper (II) sulfate pentahydrate ($\text{CuSO}_4 \cdot 5\text{H}_2\text{O}$) was bought from VWR International. Potassium sodium tartrate tetrahydrate ($\text{C}_4\text{H}_4\text{KNaO}_6 \cdot 4\text{H}_2\text{O}$) and sodium hydroxide (NaOH) were purchased from Sigma-Aldrich. Formaldehyde was supplied from Fisher Scientific. All reagents were used as received.

2.1.3 MnO_2 Paste

Manganese (IV) oxide (MnO_2), 1-Methyl-2-pyrrolidinone (NMP), and poly (vinylidene fluoride) (PVDF – 534 k g/mol) were purchased from Sigma-Aldrich. Carbon black was bought from Fisher Scientific. All reagents were used as received.

2.1.4 Other Battery Components

Manganese (II) sulfate monohydrate ($\text{MnSO}_4 \cdot \text{H}_2\text{O}$) and zinc sulfate heptahydrate ($\text{ZnSO}_4 \cdot 7\text{H}_2\text{O}$) were used as the electrolyte and purchased from Sigma-Aldrich and Fisher Scientific, respectively. The anode, zinc foil, was also obtained from Fisher Scientific. All reagents were used as received.

2.1.5 Control Samples

Carbon paper was purchased from Fuel Cell Store. Carbon cloth was from Rock West Composites. Polyacrylonitrile-co-methyl-acrylate (PAN-co-MA) was obtained from Scientific Polymer Products Inc, with an approximate molecular weight of 100 k g/mol.

2.2 Electrospinning Process

Electrospinning solution is prepared by mixing $\text{Pd}(\text{acac})_2$ with DMF in an oil bath at 90 °C until fully dissolved. Then, PEO is added and blended into the solution while heated in the oil bath until fully dissolved. Lastly, lignin is added and stirred in the DMF/PEO/ $\text{Pd}(\text{acac})_2$ solution in the oil bath for 2.5 hrs, during which the solution is vortexed for a minute every 30 minutes [87]. The first step is clearly ignored for samples without $\text{Pd}(\text{acac})_2$. Sections 3.2.1 and 3.2.2 provide design of experiments for solution optimization to achieve the smallest diameter. During optimization, molecular weight of PEO, lignin: PEO ratio, and solid content (PEO + lignin / DMF) are chosen to be 900 k or 4 M g/mol, 99:1 or 95:5, and 30 or 40%, respectively [87], [101], [129]–[132]. In section 3.2.3, the solid content ($\text{Pd}(\text{acac})_2$ + PEO + lignin / DMF) and lignin: PEO ratio are 40% and 99:1, respectively, while $\text{Pd}(\text{acac})_2$: lignin ratio is kept at 0.057,

similar to Pd(acac)₂: PAN-co-MA ratio (control sample in accordance to ref. [72] – no PEO, PAN-co-MA: DMF ratio of 0.11).

Once blended, the solution is taken off the heat and cooled to room temperature before electrospinning with Nanofiber Electrospinning Unit (NEU – Kato Tech Co., Ltd.). For electrospinning, needle to target distance of 15 cm, voltage of 17 kV, pump rate of 0.1 mm/min (0.03 mL/min), and relative humidity < 30% are selected [87], [101], [130]. The collected fibers are placed in a vacuum oven at 100 °C overnight to remove residual DMF.

2.3 Thermal Stabilization Process

Thermal stabilization process involves heating up the dried fibers at 1 °C/min from room temperature to 3 different final temperatures of 150, 175, and 200 °C. This final temperature is kept constant for 2 hrs in a tube furnace (79400 – Thermolyne) under argon gas [72], [87], [98], [133]. For PAN-co-MA, thermal stabilization occurs at around 250 °C and other parameters are the same as for lignin [72].

2.4 Electroless Copper Plating Process

To produce the electroless plating solution, 5 g/L of CuSO₄·5H₂O is first dissolved in deionized water (laboratory reagent). Then 28.57 g/L of C₄H₄KNaO₆·4H₂O is added to the mixture and stirred until dissolved. Finally, 7 g/L of NaOH is added and blended until dissolved. Plating will not start until formaldehyde is added. For optimization of electrical conductivity, 0.005, 0.025, and 0.05 mL formaldehyde per mL of solution are added to the plating solution under the fume

hood. The solution is at room temperature and plated for up to 2.5 hrs. Lastly, the plated samples are rinsed with deionized water and dried at room temperature overnight [72], [117].

2.5 Deposition of MnO₂

MnO₂, PVDF, and carbon black with a mass ratio of 80:10:10, respectively, are mixed with an appropriate amount of NMP to form a paste. The paste is coated on the fibers and allowed to dry at 60 °C overnight [134], [135].

2.6 Characterization Techniques

2.6.1 Scanning Electron Microscope (SEM)

The morphology of the electrospun fibers can be examined with SEM (FEI Quanta 650). SEM operates under high vacuum with 20 kV acceleration voltage and 10 mm working distance. Average fiber diameter and standard deviation are determined by taking 100 measurements across the samples using ImageJ software (U.S. National Institutes of Health).

2.6.2 Thermogravimetric Analysis (TGA)

To confirm the suitability of the chosen thermal stabilization temperature, TGA (NETZSCH TGA) is performed. The dried fibers are heated from room temperature to about 600 °C, while the mass is accurately measured. The flow rate is set to be 10 °C/min under nitrogen inert atmosphere [72], [133], [136].

2.6.3 Fourier Transform Infrared Spectroscopy (FTIR)

FTIR analysis can convey the type of bonds within the sample as well as the intensity of the species [136]. In this work, FTIR (PerkinElmer Frontier FT-IR) is performed using 4 scans over 4000 – 650 cm^{-1} , with a resolution of 4 cm^{-1} [87].

2.6.4 Energy Dispersive Spectroscopy (EDS or EDX)

EDS can identify and quantify the elements present within a sample. It can also generate elemental distribution maps. SEM instruments are often equipped with EDS detectors (FEI Quanta 650 with large area EDX) with 0 – 10 keV range [137], [138] and an acceleration voltage of 20 kV.

2.6.5 X-ray Diffraction (XRD)

Crystal structure of samples is characterized by XRD (Malvern-Panalytical Empyrean 3) within 5 – 80° (2θ) range using a Cu $K\alpha$ ($\lambda = 1.54 \text{ \AA}$) incident beam. The incident beam is diffracted in accordance to Bragg's law (Equation 2.1).

$$\lambda = 2d \sin\theta \quad \text{Equation 2.1}$$

In Bragg's law, d is the spacing between atomic planes, λ is the incident X-ray wavelength, and 2θ is the diffraction angle [72], [136].

2.6.6 X-ray Photoelectron Spectroscopy (XPS)

XPS is a surface-specific (penetration depth of 5 – 20 Å) chemical analysis method. Binding energy of excited electrons is calculated from Equation 2.2.

$$BE = h\nu - KE - \varphi \quad \text{Equation 2.2}$$

BE is the excited electron's binding energy, $h\nu$ is the energy of incident beam (h is Planck's constant and $\nu = c/\lambda$ is frequency, c is the velocity of light, λ is the wavelength of the incident beam), KE is the kinetic energy of excited electrons, and φ is the work function of the spectrometer [139], [140]. XPS (Kratos Analytical Axis ULTRA spectrometer) is performed with an aluminum source (Al $K\alpha$, $h\nu = 1486.6$ eV) over 0.7×0.3 mm² area of samples, with a pass energy of 160 eV for survey and 20 eV for narrow scan, averaged over 2 scans.

2.6.7 4-Point Probe Sheet Resistance and Conductivity Measurement

Electrical resistivity is measured using a 4-point probe system, where the current is supplied (KEITHLEY 2400 SourceMeter) to the outer two probes and voltage is measured (Tektronix DMM 4050 6-1/2 Digital Precision Multimeter) from the inner 2 probes. The distance between probes (probe spacing, s) is 1 mm. The sheet resistance (in ohms per square) and conductivity (in siemens per cm) can be calculated from Equation 2.3 and Equation 2.4, respectively.

$$R_s \left(\frac{\Omega}{\square} \right) = \frac{\rho}{t} = k \frac{V}{I} \quad \text{Equation 2.3}$$

$$\sigma \left(\frac{S}{cm} \right) = \frac{1}{\rho} \quad \text{Equation 2.4}$$

R_s is sheet resistance, ρ is resistivity, t is thickness in cm, k is a geometric factor based on width, length, and probe spacing, V is the measured voltage, I is supplied current, σ is conductivity [136], [141]–[143].

2.6.8 Electrochemical Performance Measurement

The following preliminary electrochemical tests are performed after connecting the battery to BioLogic VMP-300 testing station. The working electrode is the lignin-based MnO₂ electrode or carbon paper brush-coated with MnO₂ electrode. The counter electrode is zinc foil. The electrolyte consists of 2 M ZnSO₄ and 0.2 M MnSO₄ [144].

2.6.8.1 Cyclic Voltammetry (CV)

CV allows for the study of reduction and oxidation processes of species by plotting measured current at the working electrode as a function of applied voltage [136], [145]. CV is conducted at a scan rate of 0.1 mV/s over 1 – 1.8 V vs. Zn²⁺/Zn range [24], [135], [146], [147].

2.6.8.2 Galvanostatic Charge/Discharge (GCD)

GCD curves are produced as a result of application of a constant current, then charging to 1.8 V followed by a discharge to 1 V (vs. Zn²⁺/Zn) [87]. The constant current density for GCD is 0.1 mA/g (per mass of active MnO₂) [54], [146]. If GCD is run at varying current densities, rate capability can be ascertained. Here, varying current densities of 0.1, 0.2, 0.5, 1 A/g are used to

develop the rate capability plot [148]. Furthermore, running GCD over many cycles creates cycle life plots. For cycle life, current density of 0.2 A/g is chosen [149], [150].

2.6.8.3 Electrochemical Impedance Spectroscopy (EIS)

EIS applies an AC voltage signal to the cell at different frequencies and measures the resulting current. One can use EIS to determine the impedance of the battery, where different components, processes, and interfaces operate at their own unique time constants (time constants can be separated in frequency domain) [151]. The frequency for the Zn-MnO₂ battery is within 1 MHz – 10 mHz range with a small voltage amplitude of 5 mV [149], [150], [152].

Chapter 3: Preparation of Lignin-Based Fibers for Electroless Copper Plating

3.1 Introduction

This chapter investigates the fiber formation of hardwood organosolv lignin. Due to the limited supply of lignin, we start by optimizing batch named 69 BCP; then move on to batch 157 BCP for next steps (i.e., thermal stabilization and electroless plating). The initial optimization of 69 BCP is to generate fibers with the smallest diameters/highest surface-to-volume ratio. After optimization of fiber diameter, palladium (II) acetylacetonate is added to the electrospinning solution. Recall that palladium metal is the catalyst for electroless copper plating (see section 1.4.2.1.1). Following the addition of palladium (II) acetylacetonate, fibers are thermally stabilized. Fibers are analyzed and characterized with various techniques, such as SEM, TGA, EDS, FTIR, XRD, and XPS.

3.2 Lignin Fiber Diameter Optimization

3.2.1 Design of Experiments (DoE) for Diameter Optimization of 69 BCP

One of the most significant factors in fiber formation and diameter is viscosity of the polymer solution [133]. Viscosity is directly proportional to polymer concentration and molecular weight (MW) of the polymer [83], [87]. Here, the influence of the following three parameters is studied for the case of hardwood organosolv lignin: (a) MW of plasticizer (poly (ethylene oxide) - PEO), (b) lignin: plasticizer ratio, and (c) solid content. Table 3.1 illustrates the design of experiments (DoE) for the study on the 69 BCP batch.

Table 3.1 DoE for optimization of 69 BCP lignin. * The references had MW close to either 900 k or 4 M and same lignin: PEO ratio and solid content. The MW values in this thesis were chosen due to their availability in our lab. The control samples, denoted by C, provide a systematic approach to optimization.

Solvent	DMF							
MW of PEO (g/mol)	900 k				4 M			
Lignin: PEO	95 : 5		99 : 1		95 : 5		99 : 1	
Solid content (wt%)	30	40	30	40	30	40	30	40
Experiment	1	2	3	4	5	6	7	8
Inspired by ref*	[129], [130] 600 k	C	[101] 900 k	[129], [130] 600 k	[131] 2 M	C	[87], [132] 1 M	C

Figure 3.1 shows the morphology of each experiment under scanning electron microscope (SEM). From the morphology, we can see that experiments 2, 5, 6, and 8 do not produce fibers. Recall that fibers have an aspect ratio of 1000:1 (see section 1.4). In experiment 7, fibers are fused together, reducing the surface-to-volume ratio. Thus, experiments 1, 3, and 4 are top choices for further experimentation with the 157 BCP batch of lignin.

None of the top choices form bead-less fibers. In electrospinning, complete stretch of macromolecular chains is induced by a strong elongational flow, which produces bead-less fibers. Therefore, beads-on-a-string is a result of impaired coil-stretch transition of the macromolecules. The string between the beads is still stabilized (and stretched) by the elongational flow [153]–[155].

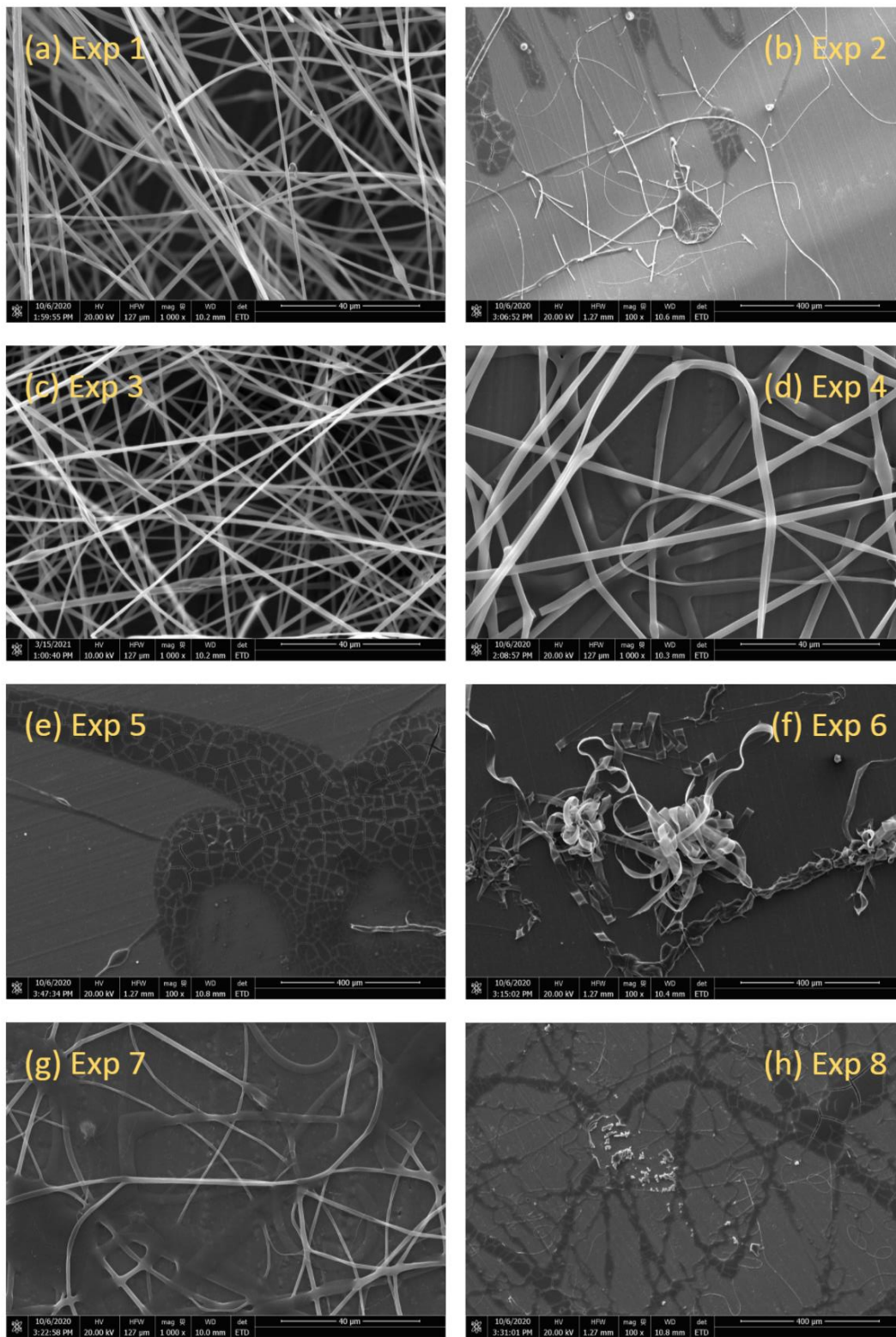


Figure 3.1 69 BCP optimization. (a) 30-95-5-900k. (b) 40-95-5-900k. (c) 30-99-1-900k. (d) 40-99-1-900k. (e) 30-95-5-4M. (f) 40-95-5-4M. (g) 30-99-1-4M. (h) 40-99-1-4M.

As expected, higher concentration (40 wt% - experiment 4) results in larger average diameter ($2.77 \pm 1.81 \mu\text{m}$) [83], [87], [130]. Experiment 1, 30-95-5-900k, has the smallest diameter ($1.24 \pm 0.46 \mu\text{m}$). Experiment 3, 30-99-1-900k, lands in the middle with a diameter of $1.29 \pm 0.69 \mu\text{m}$. In bead-less fibers, larger PEO amounts has been shown to produce larger diameters [130], [154]. However, in beads-on-a-string cases, larger PEO amounts can result in reduction of average diameter (not just string/fiber diameter), which is similar to our observations [154], [156].

3.2.2 Diameter Optimization of 157 BCP

Now, we can move on to the 157 BCP batch given the top 3 choices of 69 BCP. Figure 3.2 demonstrates that 30-95-5-900k and 30-99-1-900k samples have enormous droplets, which influence the diameter size significantly. Hence, the only choice left is 40-99-1-900k.

40-99-1-900k has an average diameter of $2.29 \pm 1.12 \mu\text{m}$. It is evident that the high concentration solution works best for 157 BCP. Since every parameter besides the lignin batch is the same between 69 and 157 BCP samples, the need for higher concentration in 157 BCP's case is likely due to its lower MW. Polymer chain entanglement occurs above a certain threshold concentration. This entanglement is required for fiber formation. Furthermore, MW is proportional to polymer chain entanglement [83]. Therefore, for low MW polymers, entanglement formation, and thus fiber formation is difficult. If concentration is increased, entanglement increases, and fibers form, as is the case for the 157 BCP lignin [130], [157]. ABC3D has kindly confirmed that 157 BCP has lower MW compared to 69 BCP.

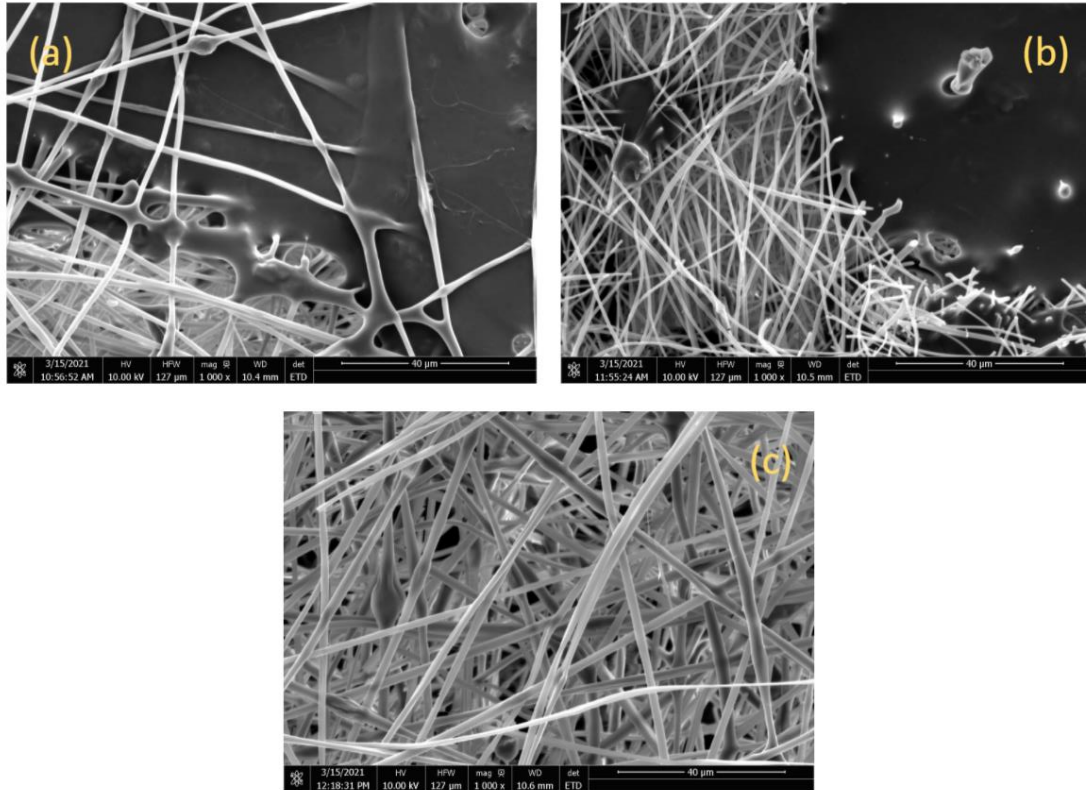


Figure 3.2 157 BCP optimization. (a) 30-95-5-900k. (b) 30-99-1-900k. (c) 40-99-1-900k.

3.2.3 Addition of Palladium (II) Acetylacetonate ($\text{Pd}(\text{acac})_2$)

Given the optimized fibers of the 157 BCP batch, palladium (II) acetylacetonate ($\text{Pd}(\text{acac})_2$) can be added to the electrospinning solution to form multifunctional fibers. Recall that $\text{Pd}(\text{acac})_2$ is used as a catalyst precursor (see section 1.4.2.1.1); with palladium (Pd) metal – Pd (0) – being the actual catalyst for the electroless copper plating.

Figure 3.3 shows the optimized 157 BCP after the addition of $\text{Pd}(\text{acac})_2$. The average diameter of the 40-99-1-900k- $\text{Pd}(\text{acac})_2$ sample is $1.24 \pm 1.59 \mu\text{m}$, which is less than the case without $\text{Pd}(\text{acac})_2$. This is likely due to the added conductivity of Pd, since the concentration is the same as before [83].

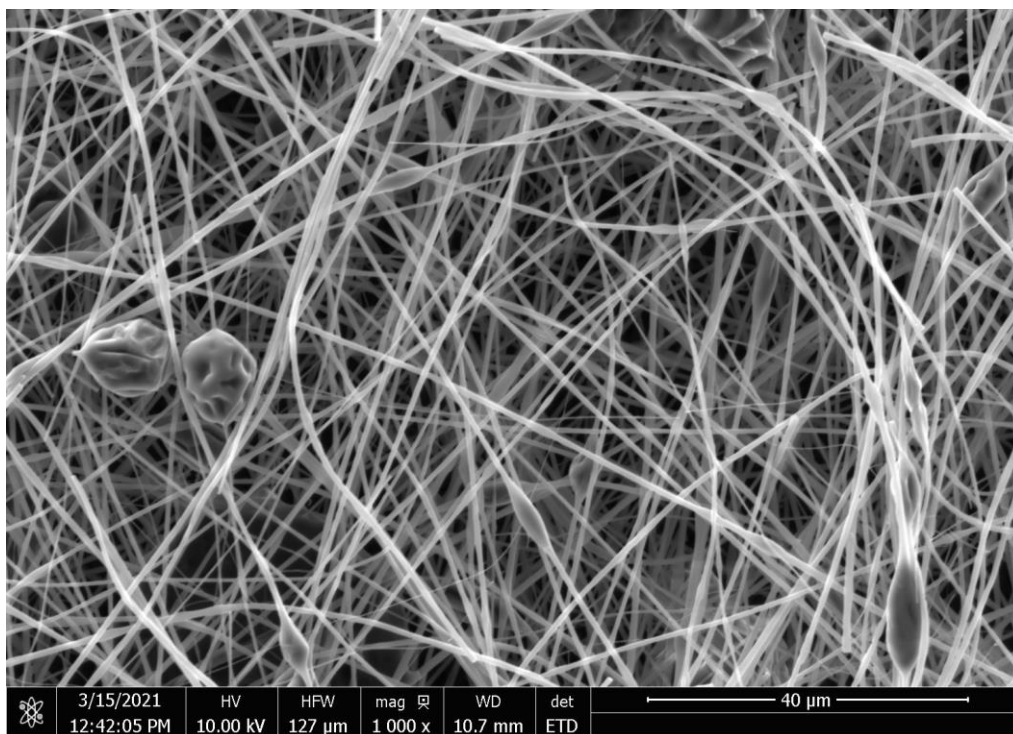


Figure 3.3 157BCP-40-99-1-900k after addition of Pd(acac)₂.

3.3 Thermal Stabilization (Thermostabilization) of Lignin Fibers

The guaiacyl structure (G unit) in lignin, with open positions on the aromatic ring, allows for cross-linking during thermal stabilization [158]. Cross-linked polymers have a wide range of properties, most importantly for this work are resistances to electroless plating solution and solvent in the MnO₂ paste (see sections 4.2 and 5.2) [159], [160]. As shown in Figure 4.1, when 157 BCP lignin is not cross-linked properly, it will dissolve in the plating solution. Thermal stabilization helps prevent this effect. Another important influence of thermal stabilization (temperatures as low as 180 °C for ~ 2 hours) is the conversion/decomposition of Pd(acac)₂ to Pd metal to act as plating catalyst [161], [162] (confirmed with XPS in section 3.3.5).

3.3.1 Thermogravimetric Analysis of Lignin

For thermal stabilization, 3 parameters are usually studied: heating rate, hold time, and final temperature; with final temperature having the most significant influence [158]. For this thesis, only the final temperature is investigated. For lignin, thermal stabilization is usually between 200 – 280 °C [98]. The decomposition temperature of Pd(acac)₂ is 300 °C [163]; with the lowest temperature at which decomposition can be observed being 180 °C [162]. Therefore, from literature, 200 °C seems to be a suitable starting temperature [98], [162], [163]. Furthermore, thermogravimetric analysis (TGA) is performed to confirm that 200 °C is below the degradation temperature of lignin samples (Figure 3.4). The extrapolated onset temperatures – temperature at which thermal degradation, decomposition, and mass loss begins [136], [164], [165] – for without and with Pd(acac)₂ samples are 228.4 and 232.8 °C, respectively. In addition, a mass drop is observed between 100 – 220 °C for the sample with Pd(acac)₂, which is due to the conversion of Pd(acac)₂ to Pd metal [72]. It should be noted that TGA was performed at 10 K/min, while thermal stabilization is to be performed at 1 K/min. We expect the degradation temperature to be lower for 1 K/min case [166] (possibly below 200 °C); but based on initial TGA results, 200 °C is selected as the starting point.

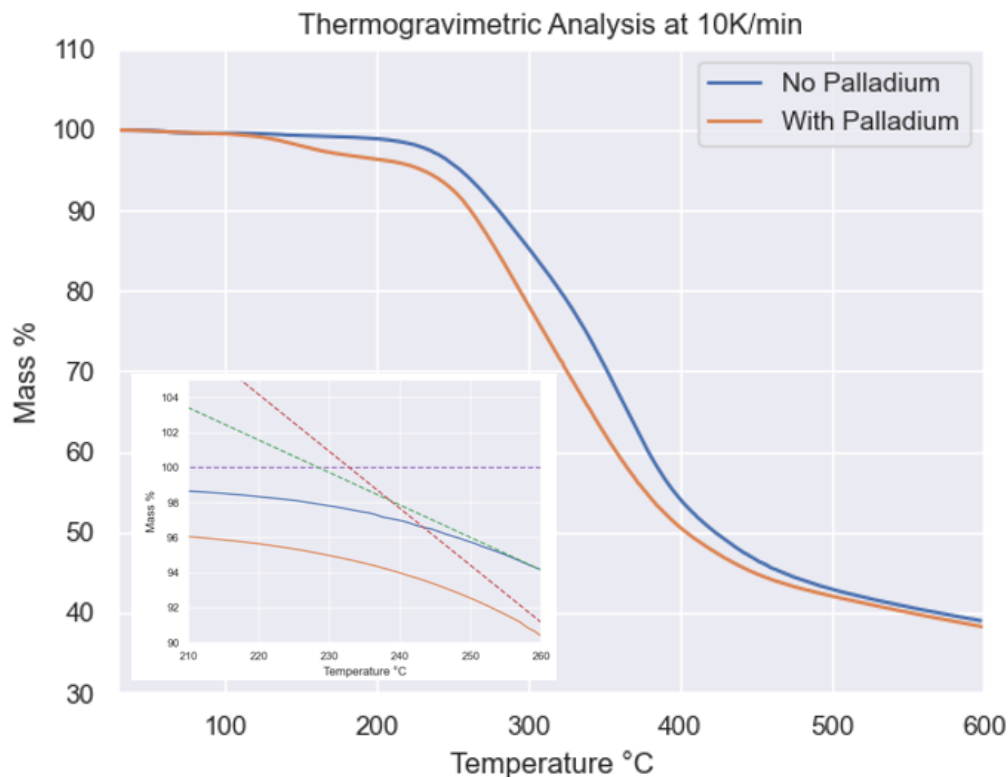


Figure 3.4 TGA of 157BCP-40-99-1 with and without Pd(acac)₂ at 10 K/min. Inset is zoomed in between 210 – 260 °C.

SEM results (Figure 3.5) show that at 200 °C, fibers fuse together and the surface-to-volume ratio is consequently reduced. Therefore, temperature is lowered to 175 °C, where fiber fusion is still evident. The temperature is then lowered to 150 °C, where no fiber fusion is observed; however, cross-linking needs to be confirmed. The easiest method of examining cross-linking is by putting the lignin samples in the electroless plating solution, which is an alkaline solution (see section 1.4.2.1). As illustrated in Figure 4.1, the 150 °C sample dissolves in the solution within a few minutes; thus, it was not properly stabilized. Due to the low surface-to-volume ratio of 200 °C sample, 175 °C is chosen for electroless plating. Following sections further examine the thermostability of 150, 175, and 200 °C samples and emergence of Pd metal.

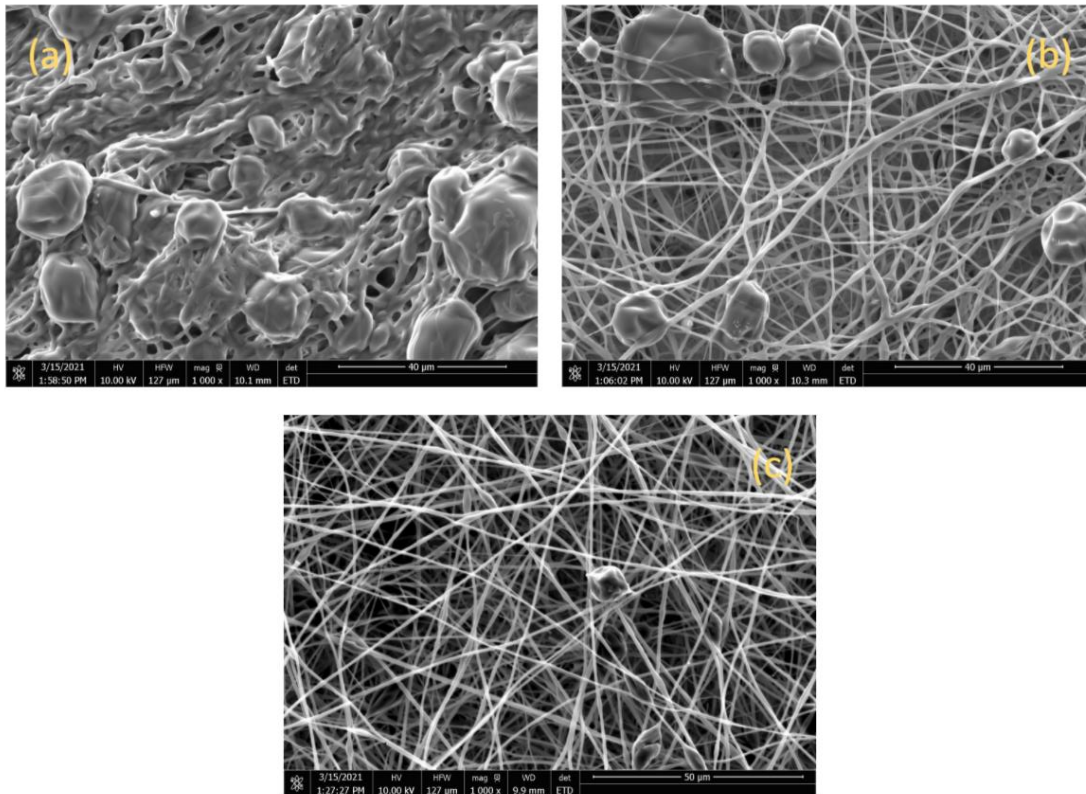


Figure 3.5 Thermal stabilization of 157BCP-40-99-1-with-Pd(acac)₂ at (a) 200 °C. (b) 175 °C. (c) 150 °C.

3.3.2 Energy Dispersive Spectroscopy of Thermostabilized Lignin

Figure 3.6 shows the energy dispersive spectroscopy (EDS) analysis of the 175 and 200 °C samples. Palladium can be detected by spot analysis (~ 0.02 wt% of Pd in fibers is just above EDS's detection limit of 0.01 wt% [137]). Spot analysis (Table 3.2) demonstrates that more Pd is detected at higher temperature (XPS also confirms this; see section 3.3.5) [161]. In the EDS spectrum, carbon content is higher for 175 compared to 200 °C. This is likely due to cleavage of bonds at higher temperature (see section 3.3.3 for FTIR analysis with similar conclusion) [87].

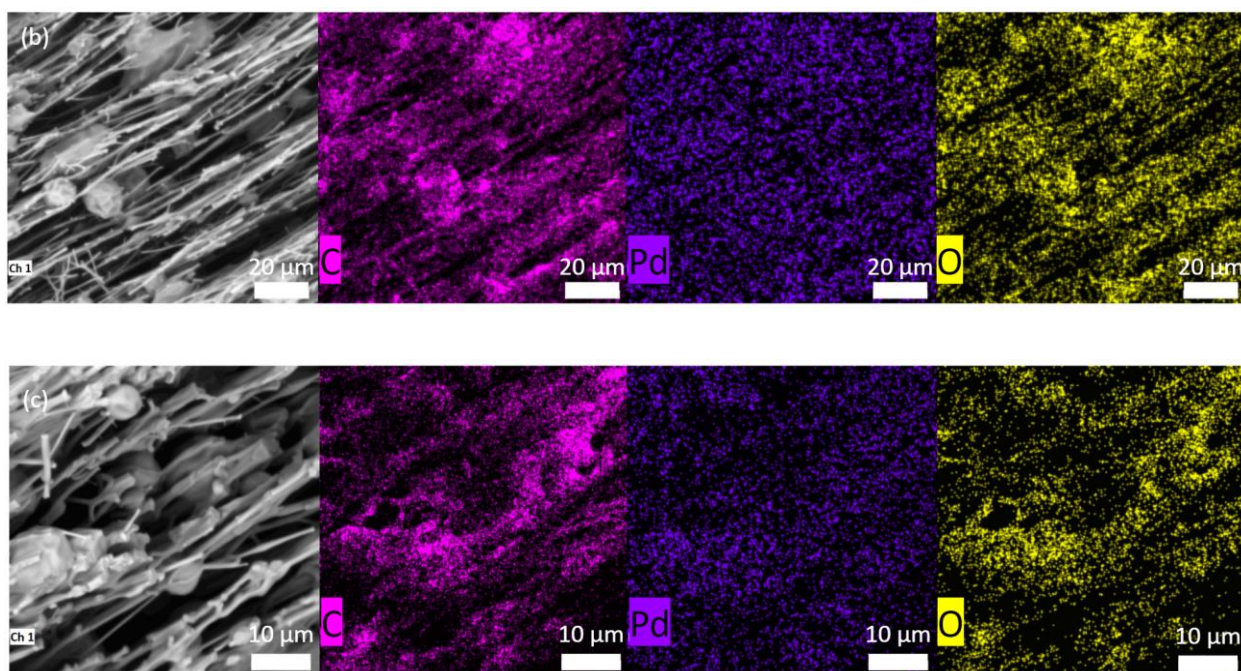
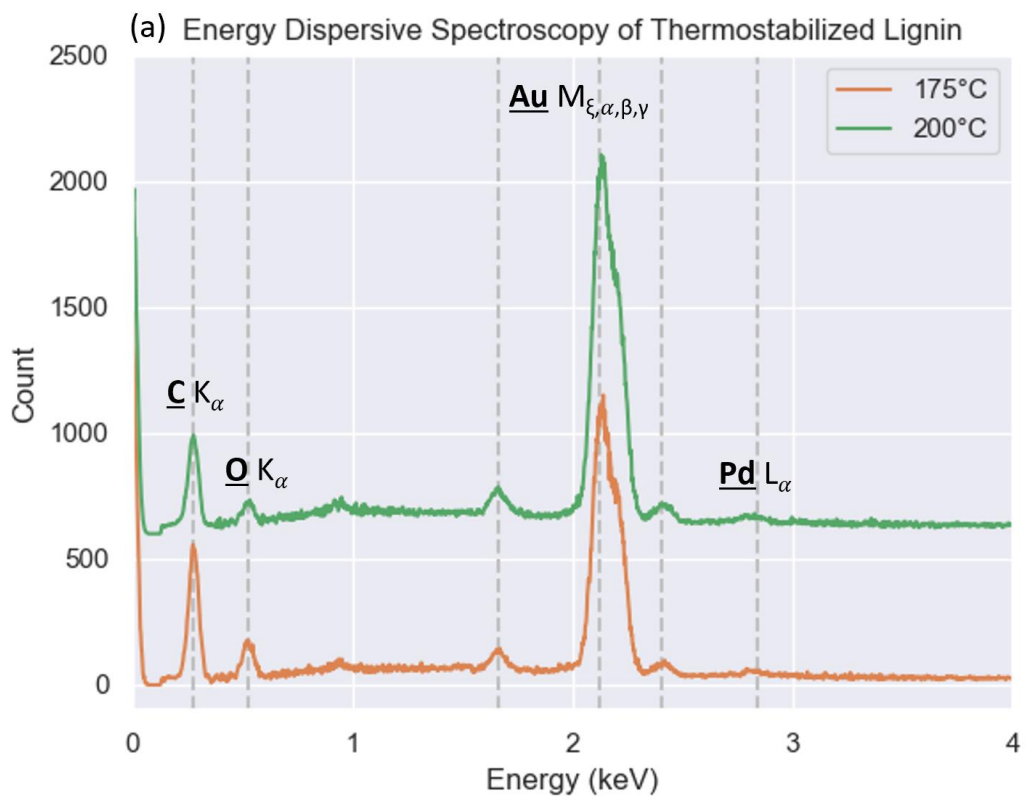


Figure 3.6 EDS of 175 and 200 °C thermostabilized lignin. (a) spectrum. (b) elemental mapping of 175 °C cross section. (c) elemental mapping of 200 °C cross section. C_K α and O_K α values are from ref. [167], [168].

Table 3.2 EDS elemental mass % of 175 and 200 °C thermostabilized lignin.

Element	175 °C Mass %	200 °C Mass %
Carbon	56.33	56.03
Oxygen	32.42	26.82
Palladium	11.25	17.16

3.3.3 Fourier Transform Infrared Spectroscopy of Thermostabilized Lignin

Fourier transform infrared spectroscopy (FTIR) uncovers the changes in chemical structure of lignin stabilized at different temperatures. The band assignments are numbered in Figure 3.7 and listed in Table 3.3. A reduction in absorbance for the 200 °C sample is seen between 1000 – 1600 cm^{-1} (see Appendix B for normalized values and overlaid plot of the 3 different temperatures). In this range, peaks at 1030, 1217, and 1265 cm^{-1} indicate C–O stretch and deformation of methoxyl group; hence, cleavage of methoxyl group at C3 position is probable for the 200 °C sample [87]. The reduction of carbonyl groups – 1593 cm^{-1} peak for 200 °C and 1659, 1700, and 1711 cm^{-1} peaks for both 175 and 200 °C samples – is also an indication of stabilization. The change in aromatic C–H stretch (854 cm^{-1} peak) is indicative of cross-linking at C5 position of G units [169]. Removal of phenolic or alcoholic groups is shown by reduction of absorbance at 3411 cm^{-1} for both 175 and 200 °C samples. Methyl groups (2920 and 2852 cm^{-1} peaks) are likely cleaved in the 175 °C sample [170]. In general, the peaks in region between 1000 – 1600 cm^{-1} are larger for 175 °C, compared to the 200 °C sample. Considering the 150 °C sample as the baseline, the change in carbon content at different temperatures implies that the bands are probably first stretched (larger peaks at 175 °C compared to 150 °C); followed by

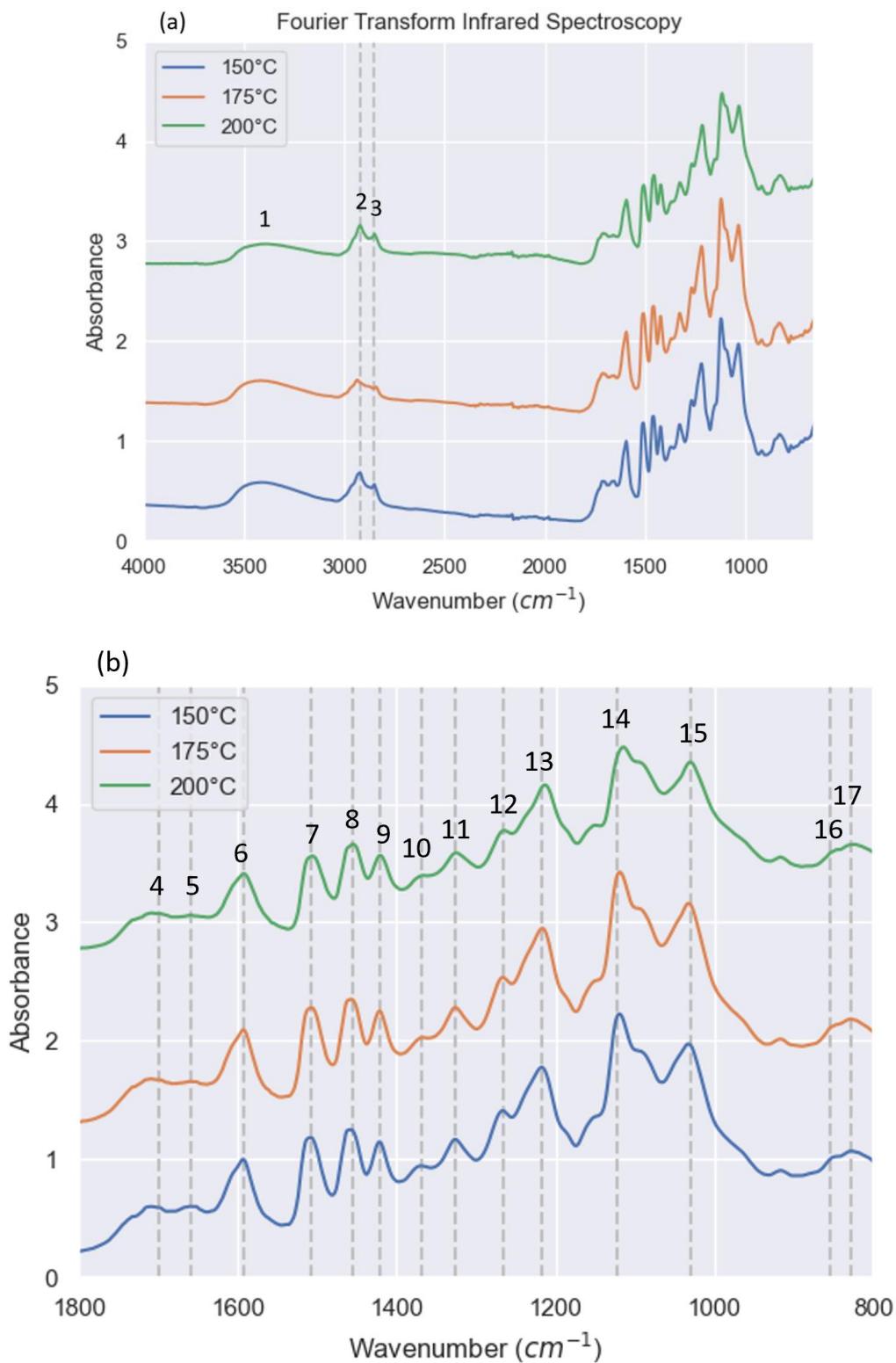


Figure 3.7 FTIR spectrum of thermostabilized lignin at different temperatures. (a) full spectrum. (b) 1800 – 800 cm^{-1} range, normalized based on peak 6 (the first aromatic vibration peak) – see Appendix B for exact normalized values.

Table 3.3 FTIR band assignments for organosolv lignin [100], [111], [171].

Band/signal assignment	Peak Wavenumber (cm ⁻¹)	Num on plot
O–H stretch	3411	1
C–H stretch in –CH ₃ and –CH ₂ –	2920	2
C–H vibration of methyl group of methoxyl	2852	3
C=O stretch in unconjugated ketones, carbonyls and in ester groups; conjugated aldehydes and carboxylic acids	1700, 1711	4
C=O stretch; in conjugated p-substituent aryl ketones; conjugated carbonyl and carboxyl; absorbed OH	1659	5
Aromatic skeletal vibrations (S > G); C=O stretch; G condensed > G etherified	1593	6
Aromatic skeletal vibrations (G > S)	1508	7
C–H deformation; asymmetric in –CH ₃ and –CH ₂ –	1456	8
Aromatic ring vibrations of phenyl-propane (C9) skeletal combined with C–H in-plane deformation	1421	9
Aliphatic C–H stretch in CH ₃ , not in OCH ₃ ; phenolic OH	1369	10
S ring plus condensed G ring	1327	11
C=O stretch; C–O stretch in G aromatic methoxyl groups	1265	12
C–C stretch; C–O stretch; C=O stretch; G condensed > G etherified	1217	13
Aromatic C–H in plane deformation (typical for S units); secondary alcohols; C=O stretch	1122	14
Aromatic C–H in plane deformation; C–O deformation in primary alcohols; C=O stretch (unconjugated)	1030	15
C–H out-of-plane deformation in G units	~ 854	16
C–H out-of-plane deformation in S and H units	~ 829	17

cleavage and rearrangement of structure (smaller peaks at 200 °C compared to 175 °C) [87], [170]. Note that the 150 °C sample does not show stretching or cleavage of bands, as seen for the

175 and 200 °C samples, respectively. This further confirms that the 150 °C sample is not stabilized.

3.3.4 X-ray Diffraction of Thermostabilized Lignin

X-ray diffraction (XRD) characterizes the micro and crystal structure of thermostabilized lignin (Figure 3.8 and Table 3.4). A broad peak at around 22° (related to the (002) crystallographic plane of disordered carbon [87]) is observed for all 3 temperatures. The lack of well-defined (sharp) peaks indicates an amorphous structure; however, the slight sharpening of the peak as well as reduction in interplanar spacing at higher temperatures show rearrangement of structure [87], [170], [172]. Additionally, a small peak is visible at around 40° for the 200 °C sample, which can be from Pd metal [161]. XPS characterization further confirms the existence of Pd metal (section 3.3.5).

Table 3.4 Interplanar parameters of XRD plots of thermostabilized lignin at different temperatures.

Temperature	2 θ (°)	d-spacing (nm)
150 °C	21.0265	0.4222
175 °C	21.2816	0.4172
200 °C	21.3665	0.4155

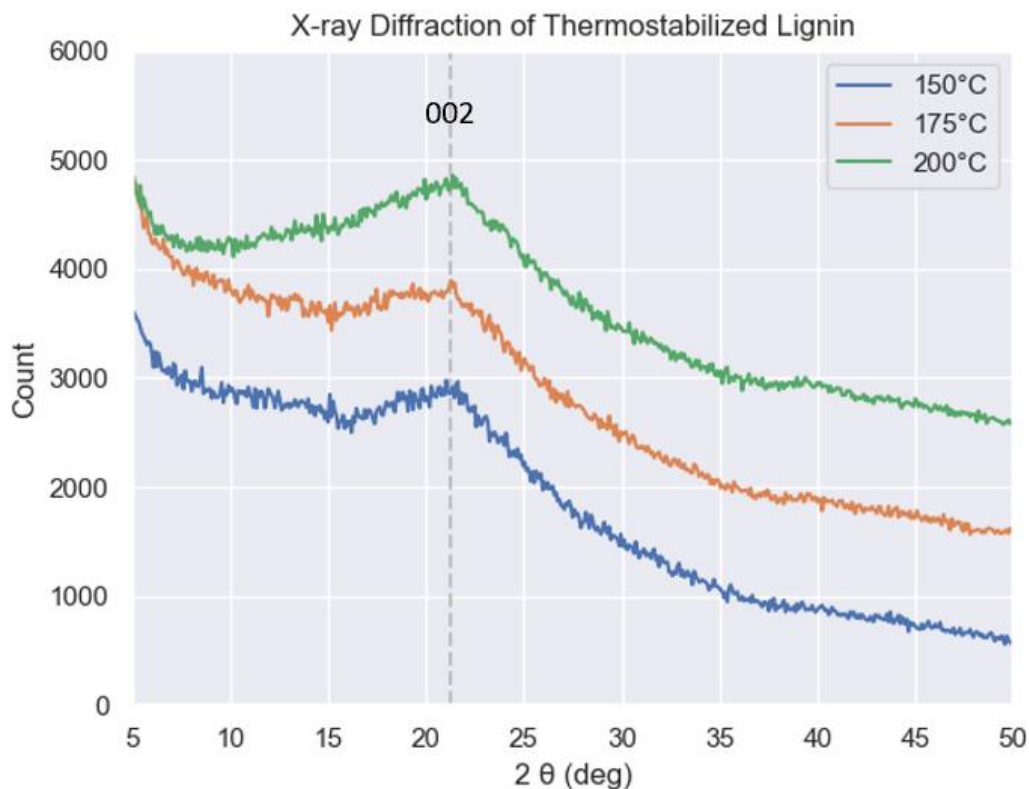


Figure 3.8 XRD of thermostabilized lignin at different temperatures.

3.3.5 X-ray Photoelectron Spectroscopy of Thermostabilized Lignin

X-ray photoelectron spectroscopy (XPS) can illustrate whether Pd metal has formed during the thermostabilization process. The dominant peak around 334.1 eV – assigned to Pd (0) [173]– [175] – shows that the reduction from Pd (II) to Pd (0) has occurred (Figure 3.9) [161].

Therefore, the catalyst for electroless plating is produced. Interestingly, XPS results agree with the FTIR observation of an increase in carbon content at 175 °C and a decrease at 200 °C [87]. Additionally, XPS confirms the EDS result of higher Pd at higher temperatures [161]. In general, Pd (0) has been created and the fibers are ready to be plated.

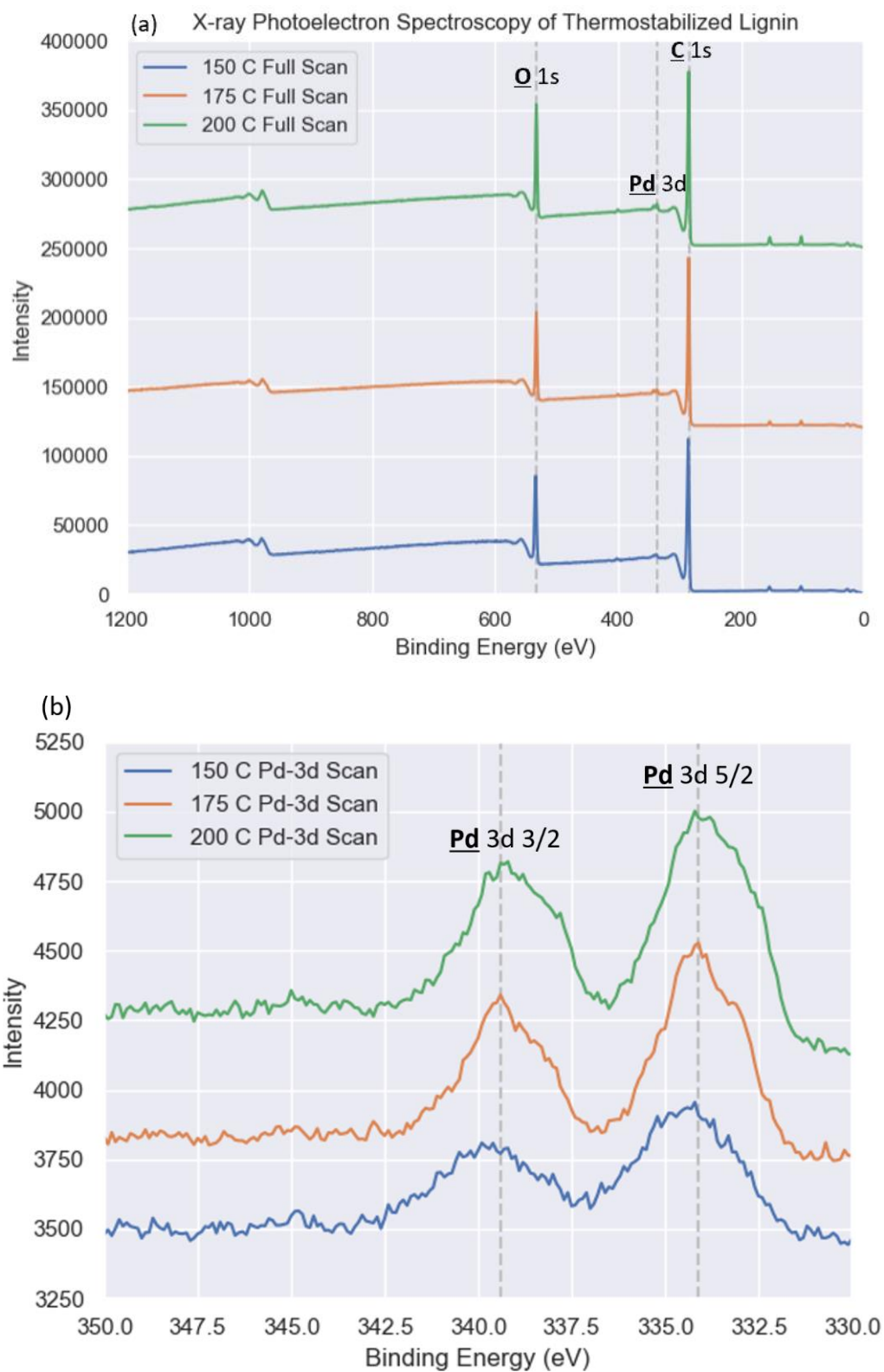


Figure 3.9 XPS of thermostabilized lignin at different temperatures. (a) survey scan. (b) Pd 3d narrow scan. O 1s, C 1s, Pd 3d values were provided by 4D LABS and confirmed through ref. [173]–[175].

3.4 Concluding Remarks

In this chapter, the preparation of lignin samples for electroless plating has been described.

Hardwood organosolv lignin is specifically chosen due to its preferred spinnability. Electrospun lignin fiber diameter is initially optimized by varying MW of plasticizer, lignin: plasticizer ratio, and solid content. Once an optimized recipe is identified, Pd(acac)₂ is added to the electrospinning solution as the catalyst precursor.

The samples are then thermostabilized to ensure (1) cross-linking, and (2) conversion of Pd (II) to Pd (0) have occurred. A series of characterization methods (e.g., EDS, FTIR, XRD, and XPS) are used to assess the thermostability of the lignin fibers. Through characterization similar conclusions can be drawn that (1) more Pd (0) is generated at higher temperatures, and (2) carbon content initially increases then reduces due to stretching and cleavage, as temperature is raised. The 175 °C sample is chosen as the substrate for electroless plating and MnO₂ deposition in the following chapters due to its high surface-to-volume ratio. From FTIR results and the behavior of samples in the plating solution, one can conclude that the 200 °C sample is the most stabilized, while the 150 °C sample is not stabilized. The 175 °C sample is somewhat more stabilized than the 150 °C sample; however, further investigation into its stability in the plating solution is required.

Chapter 4: Electroless Copper Plating Optimization Based on Electrical Conductivity Measurements

4.1 Introduction

In Chapter 4, stability of lignin electrospun fibers is first examined in the plating solution. As discussed in Chapter 3, the 175 °C lignin sample may not be chemically stable, thus the electroless copper plating solution is designed to accommodate any instabilities by varying the reducing agent (i.e., formaldehyde) amounts, sonication time, and plating time. The optimization ensures that the 175 °C lignin does not dissolve in solution and meets the target values of electrical conductivity (denoted as conductivity henceforth) and sheet resistance. The copper plated fibers are characterized using SEM, EDS, XRD, and XPS to provide insight into the existence of copper.

4.2 Examining Thermostability of Lignin Fibers in Electroless Plating Solution

The 150 and 175 °C samples are put in separate vials, plating solution with the recipe in section 2.4 is poured over each sample, and 0.075 mL of formaldehyde per 15 mL of solution (0.005 mL/mL solution) – as suggested by ref. [72] – is lastly added to each vial. Figure 4.1 shows that the 150 °C sample starts to dissolve in the plating solution within only 3 minutes, confirming its instability, as discussed in section 3.3.3. The 175 °C sample, on the other hand, does not dissolve or change the colour of the solution, unless left in solution for a while (e.g., 2.5 hrs). Therefore, the plating solution is modified to certify that 175 °C lignin does not dissolve and is plated.

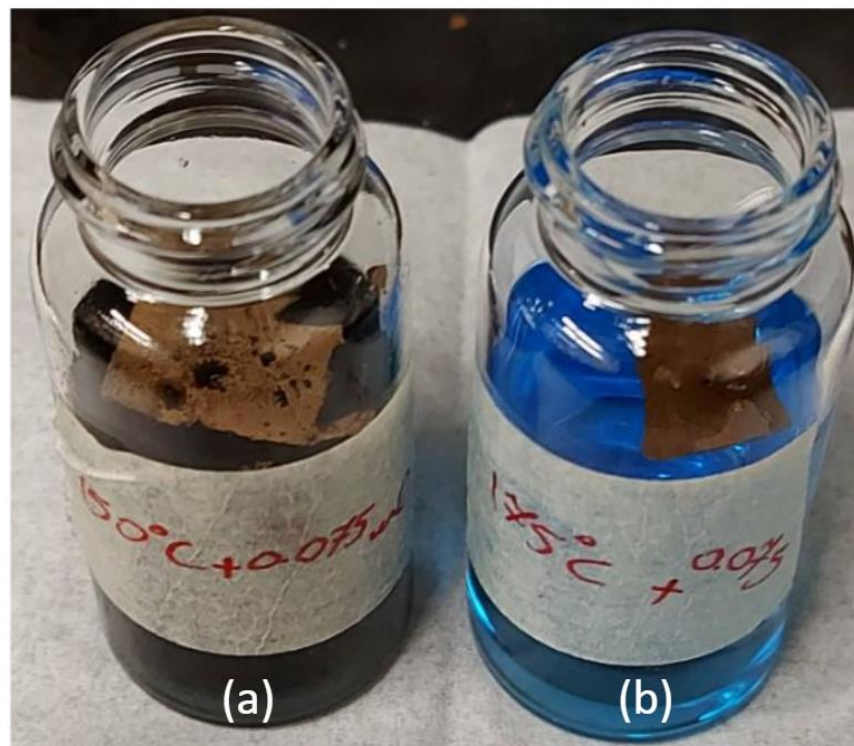


Figure 4.1 Stability of thermostabilized samples with 0.005 mL formaldehyde per mL of solution. (a) 150 °C. (b) 175 °C (after only 3 minutes in the solution).

4.3 Electroless Plating Solution Optimization of Conductivity

As discussed in section 1.1.2.2, for current collectors, high conductivity is a prerequisite. For this thesis, we will target conductivity of at least 575 S/cm and sheet resistance below $0.33 \Omega/\square$, as described in Table 1.1.

In general, longer plating time increases the thickness of the deposited metal and decreases the sheet resistance. Additionally, higher rate of deposition has been shown to decrease the sheet resistance [176]. In the following sections, the influence of deposition rate and plating time are further discussed.

4.3.1 Formaldehyde Amount and Ultrasonication

The recipe of the bath is described in section 2.4. The formaldehyde amount of 0.005 mL/mL of solution is suggested by ref. [72]. However, such bath solution results in undetectable (very high) sheet resistance and dissolves the 175 °C lignin after 2.5 hrs. Therefore, the experiments in Table 4.1 are designed to help achieve detectable and high conductivity, while avoiding the dissolution of samples. This optimization is achieved by varying the formaldehyde amounts and sonication time.

From Table 4.1, one can notice that higher amounts of formaldehyde greatly enhance the conductivity. Higher formaldehyde amounts have been shown to increase the speed of the reaction [177]. However, beyond a certain point (0.03 mL/mL of solution) – given an initial pH and $\text{CuSO}_4 \cdot 5\text{H}_2\text{O}$ amount – an increase in formaldehyde amount, decreases the rate due to lower spontaneity [178]. Recall, from section 1.4.2.1, that higher pH is desirable for more thermodynamically favorable (spontaneous) plating. Therefore, the lower pH and spontaneity lower the rate of reaction [117], [178], while providing a pH that does not dissolve the 175 °C sample. The pH of 0.05 mL formaldehyde per mL of solution and 5-min sonicated sample drops from 13.2 to 13.0 after the addition of formaldehyde (lignin completely dissolves in solutions with $\text{pH} > 13$ [156]) .

Ultrasonication is performed to increase the number of anchor sites and improve adhesion of copper [179], [180], resulting in lower resistivity [181]. This effect can be seen from Table 4.1, for 0.05 mL of formaldehyde per mL of solution, where higher sonication time results in higher

conductivity. However, at 10 minutes of sonication, the instability of 175 °C starts to cause issues (visible change in solution colour – from dark blue to brown).

Table 4.1 Electroless plating optimization based on formaldehyde amount and sonication time. Total plating time is 2.5 hours for all samples. The units are in Ω/\square (S/cm). The control samples, denoted by C, provide a systematic approach to conductivity optimization.

Formaldehyde	No sonication	5 – min sonication	10 – min sonication	Ref supporting formaldehyde amounts
0.005 mL/mL solution	-	-	14.41 ± 0.002 (3.30 ± 0.43)	[72]
0.025 mL/mL solution	-	11281.5 ± 0.02 (0.01 ± 0.17)	-	[182] 0.02 mL/mL of solution
0.05 mL/mL solution	$0.30 \pm 8.65E^{-5}$ (203.17 ± 0.19)	0.10 ± 0.05 (596.34 ± 0.69)	-	C
Ref supporting sonication time	[72]	[179]	[180]	

From Table 4.1, one can choose 0.05 mL of formaldehyde per mL of solution and 5-minute sonication as the optimal case. This combination meets both target values (above 575 S/cm and below $0.33 \Omega/\square$).

4.3.2 Plating Time

As mentioned earlier, longer plating time decreases resistivity (and increases the conductivity), due to the added thickness of deposited copper [176]. Table 4.2 and Figure 4.2 illustrate the pattern of higher conductivity for longer plating time. Electroless plating of copper with a similar recipe as this thesis (but with lower formaldehyde amounts) can take up to 2 hrs [182], [183]. However, due to the lower rate of reaction, we are not able to meet the target values after 2 hrs of plating; thus, the plating process is continued for another 30 minutes for a total of 2.5 hrs.

Table 4.2 Conductivity and sheet resistance of optimized sample (5-min sonication and 0.05 mL/mL solution of formaldehyde) for different plating times.

Plating Time	Conductivity ($\frac{S}{cm}$)	Sheet Resistance ($\frac{\Omega}{\square}$)
30 mins	-	-
1 hr	-	-
1.5 hrs	34.61 ± 0.29	2.21 ± 0.06
2 hrs	187.77 ± 0.12	0.39 ± 0.003
2.5 hrs	596.34 ± 0.69	0.10 ± 0.05

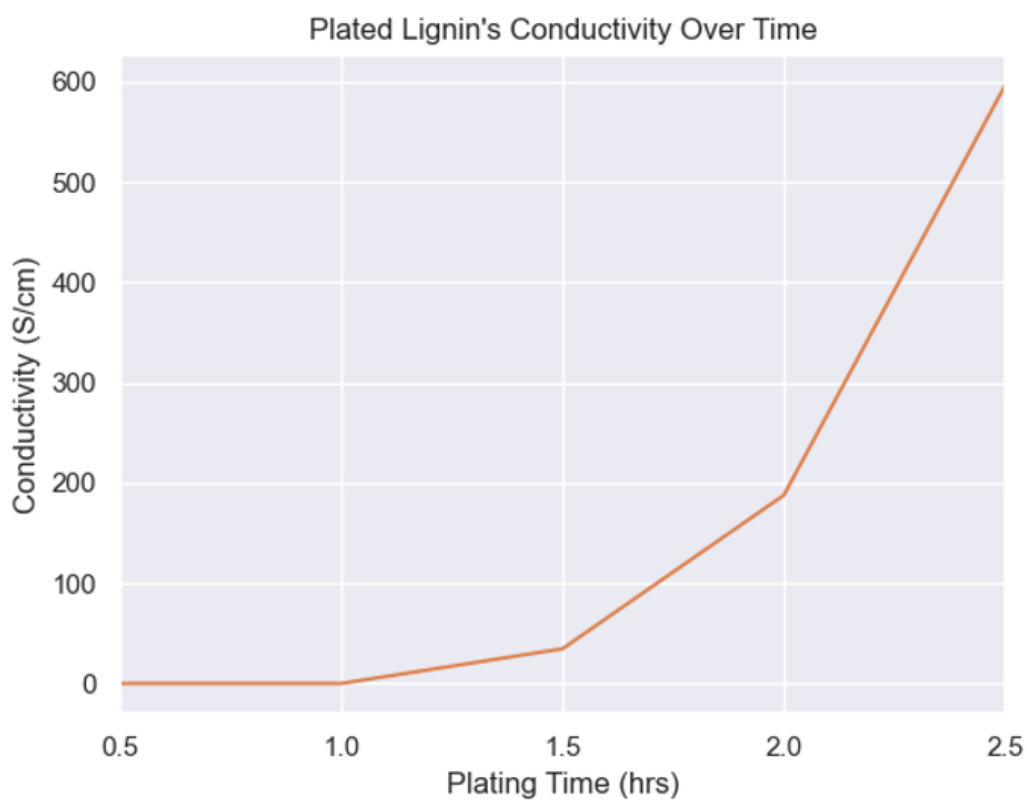


Figure 4.2 Conductivity of lignin samples over time in optimized plating solution (5-min sonication and 0.05 mL/mL solution of formaldehyde).

The SEM (BSE) images can help with understanding the sharp increase in conductivity with respect to plating time. As seen in Figure 4.3, after 2.5 hrs, the sample is fully covered with copper. However, at 30 mins, there is barely any copper detected; thus, zero conductivity. At 1.5 hrs, there are portions of the samples that are not fully covered, resulting in low conductivity. As one can expect, the discontinuity in samples results in electrons having to travel a longer distance through the portions that are covered by copper, hence the lower conductivity [184], [185] (see section 4.4.1 for confirmation of existence of copper).

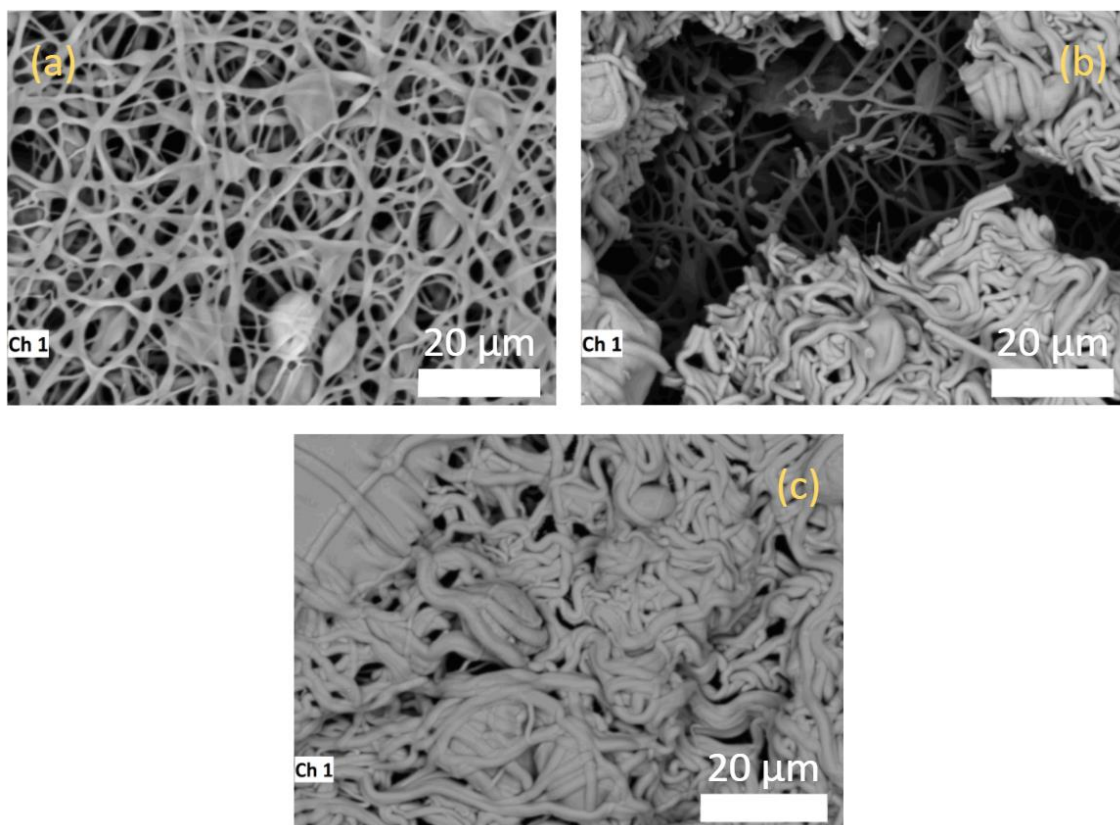


Figure 4.3 SEM (BSE) images of copper plated 175 °C lignin after different plating times (5-min sonication and 0.05 mL/mL solution of formaldehyde): (a) 30 mins. (b) 1.5 hrs. (c) 2.5 hrs.

4.4 Confirmation of Copper Deposition

The following sections provide insight into the existence of copper on plated samples. EDS, XRD, and XPS all confirm the existence of copper metal. XRD and XPS distinguish different oxidized copper types as well.

4.4.1 Energy Dispersive Spectroscopy of Plated 175 °C Lignin

Figure 4.4 indicates the EDS copper mapping on the plated 175 °C lignin fibers, confirming that not much copper is visible on the 30 mins sample, 1.5 hrs sample is not fully plated, and 2.5 hrs sample is fully covered with copper.

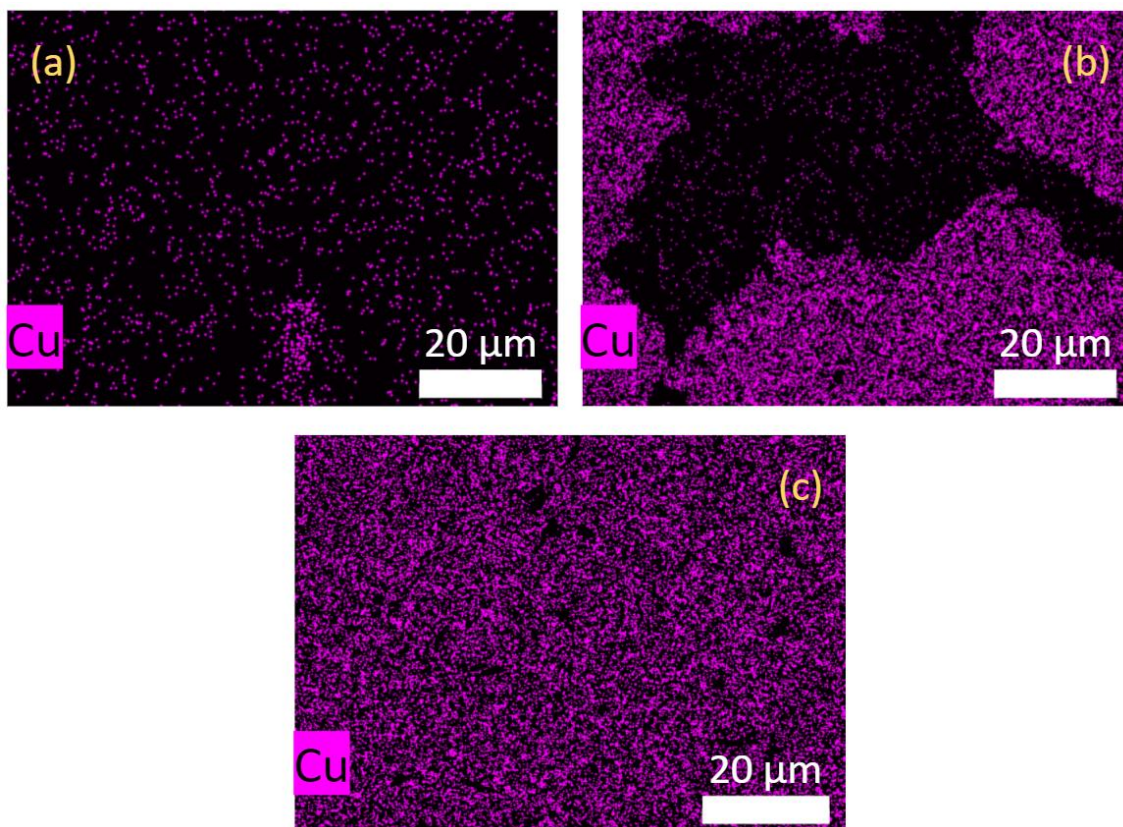


Figure 4.4 EDS mapping of copper plated on 175 °C lignin after different plating times (5-min sonication and 0.05 mL/mL solution of formaldehyde): (a) 30 mins. (b) 1.5 hrs. (c) 2.5 hrs.

As for cross-section of plated fibers, Figure 4.5 demonstrates that the surface of the sample is plated with copper; but copper is detected throughout the thickness of the plated lignin as well (about 34.11 mass % in the middle). Table 4.3 shows the mass percentage of each element, excluding the gold coating.

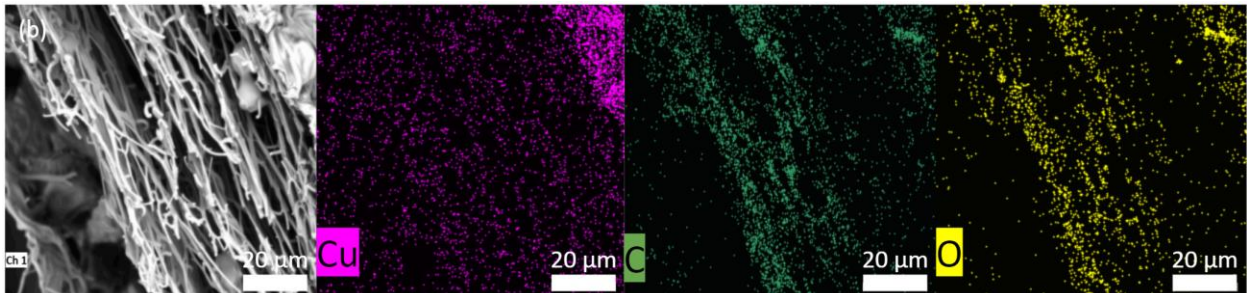
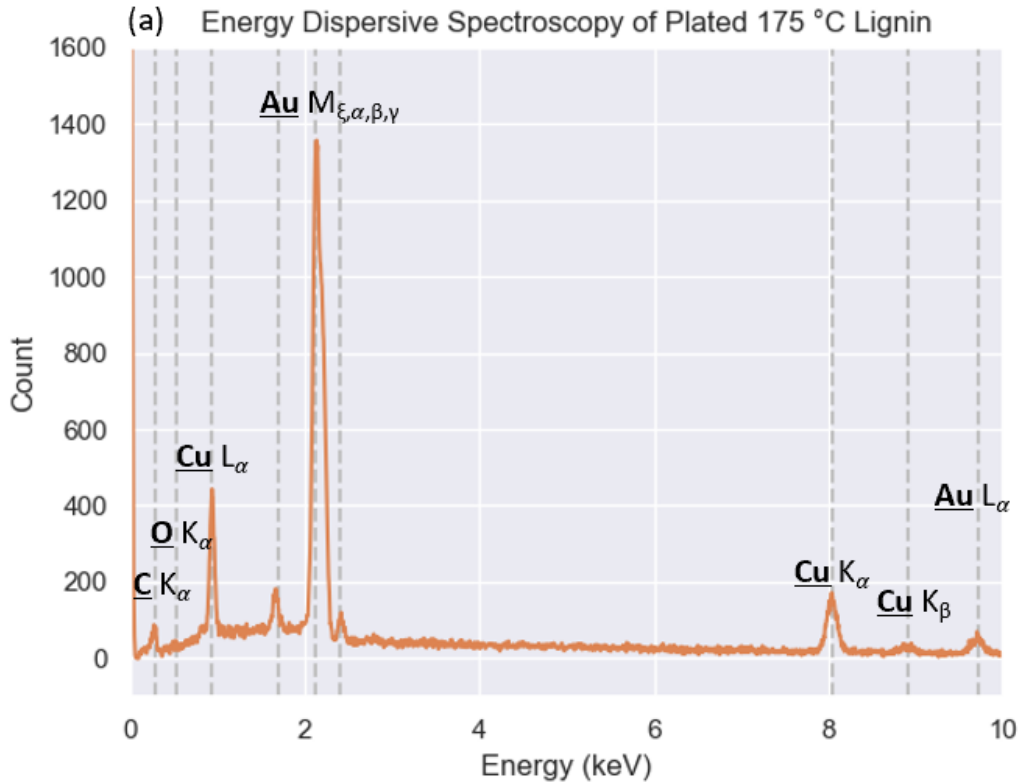


Figure 4.5 EDS of copper plated 175 °C lignin. (a) spectrum on the surface. (b) elemental mapping of the cross section. C_K α , O_K α , Cu_L α , Au_M, Cu_K α , Cu_K β , Au_L α values are from ref. [167], [168], [186].

Table 4.3 EDS elemental mass % on the surface of copper plated 175 °C lignin.

Element	Plated lignin (2.5 hrs, 5 min sonication, 0.05 mL/mL solution of formaldehyde) Mass %
Carbon	6.41
Oxygen	0.91
Copper	92.69

4.4.2 X-ray Diffraction of Plated 175 °C Lignin

Figure 4.6 validates the copper deposition by XRD peaks at 43.4, 50.5, and 74.2° [187]. The first peak at around 22° corresponds to (002) plane of disordered carbon and is the same peak as seen in section 3.3.4 for 175 °C lignin [87]. The other peaks are from copper (I) oxide at 36.6 and 61.8° [188].

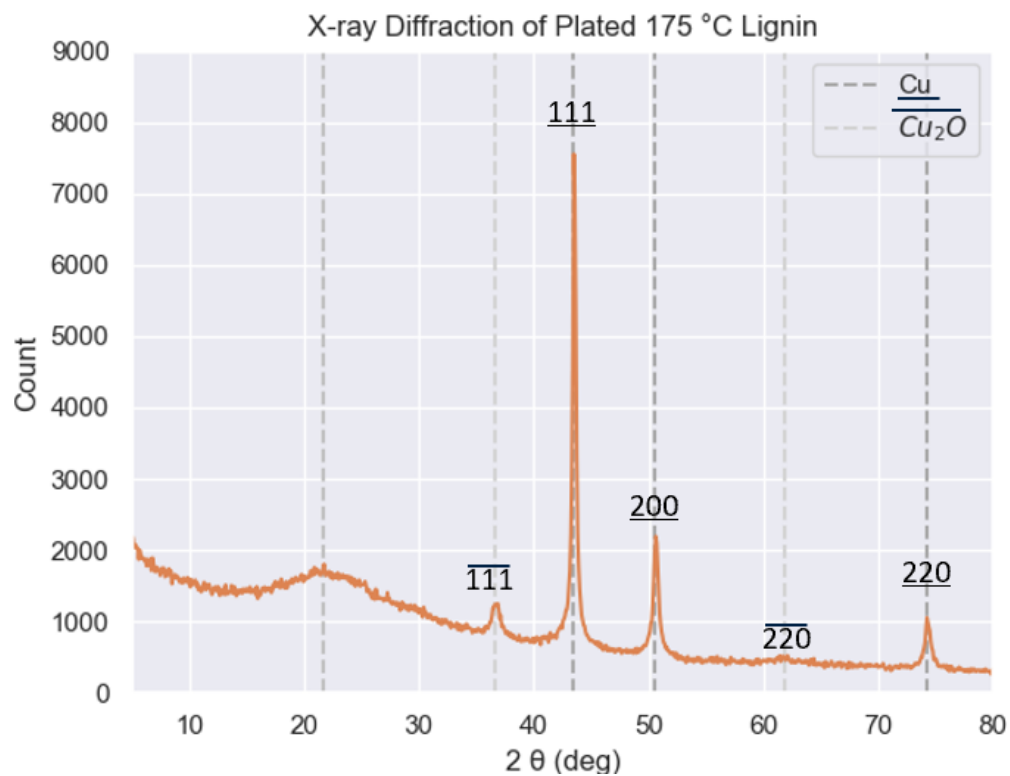
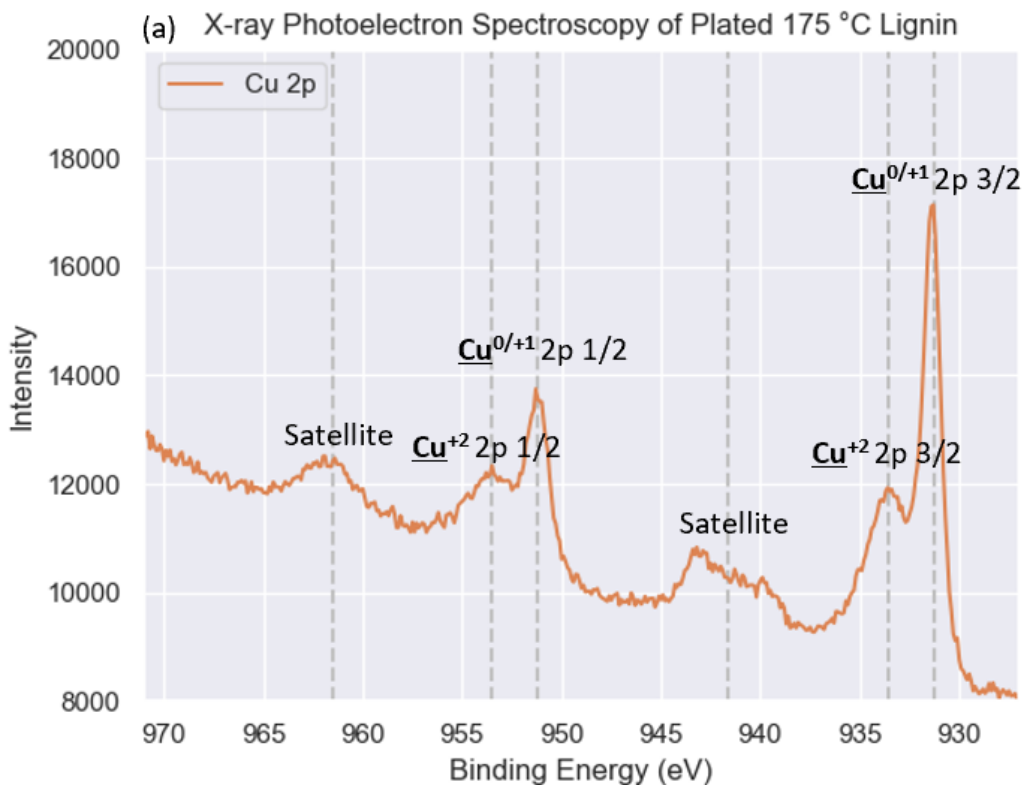


Figure 4.6 XRD of plated 175 °C lignin.

4.4.3 X-ray Photoelectron Spectroscopy of Plated 175 °C Lignin

XPS is a complementary characterization method to XRD [189]. Together, we can see how and if copper has oxidized. In XRD, CuO peaks are not detected, possibly due to their low concentration. In XPS, however, Cu, CuO, and Cu₂O peaks are visible (Figure 4.7).

The Cu-2p narrow scan illustrates that Cu (0) and Cu (I) lie on top of each other, with peaks at 931.3 and 951.2 eV [188], [190], [191]. The O-1s narrow scan helps confirm that Cu (I) is, in fact, present on the sample (peak at 530.3 eV [192]). The Cu-2p peaks of Cu (II) are located at 933.6 and 953.5 eV with weak satellite peaks around 941.6 (doublet) and 961.5 eV [188], [193], [194]. Finally, the O-1s peak of Cu (II) is at 529.6 eV [193].



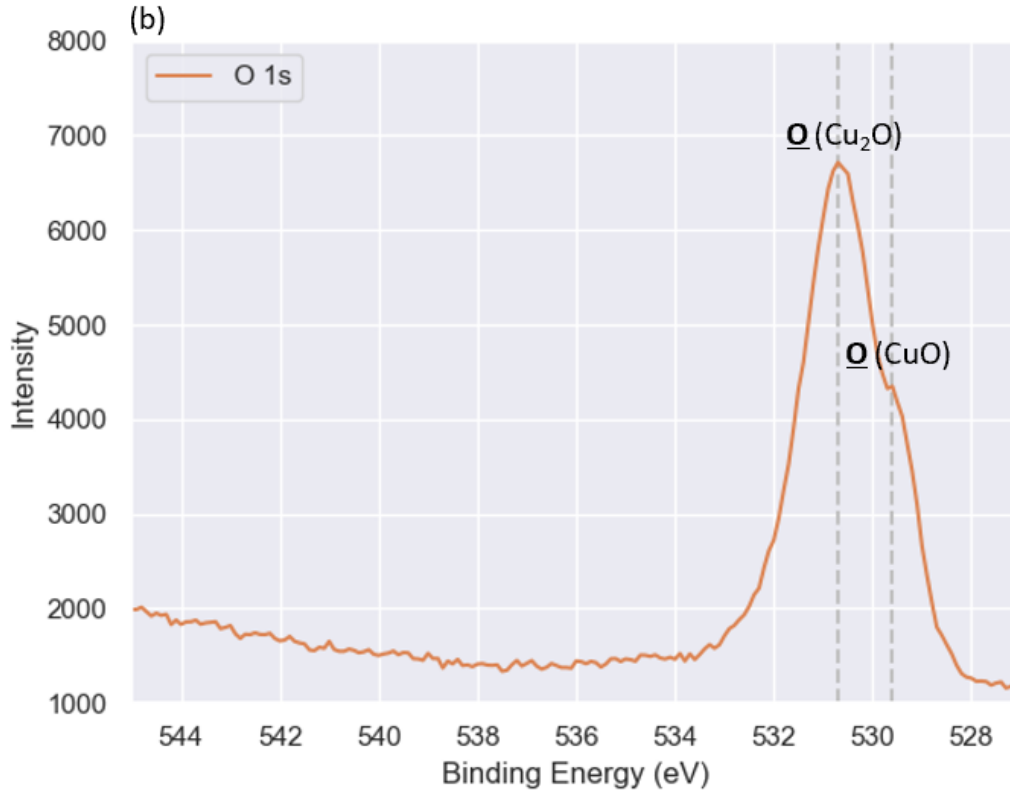


Figure 4.7 XPS of plated 175 °C lignin. (a) Cu 2p narrow scan. (b) O 1s narrow scan. Cu 2p, and O 1s values were provided by 4D LABS and confirmed through ref. [188], [190]–[194].

4.5 Concluding Remarks

In this chapter, an electroless plating solution optimization is presented to complement the unstable nature of the 175 °C lignin sample. The key to such solution is to lower pH to around 13 to avoid dissolution of lignin fibers. The deposition of copper is confirmed through conductivity measurements, EDS, XRD, and XPS. XRD can distinguish between Cu metal and Cu₂O, while XPS differentiates Cu₂O and CuO.

In the next chapter, the plated lignin will be brush-coated with an MnO₂ paste to create the working electrode. Table 4.4 shows how the lignin-based current collector compares to carbon paper and carbon cloth current collectors, which are commonly used in Zn-MnO₂ batteries [22],

[23], [52], [134], [135], [146], [195], [196]. Additionally, as a control sample for the plating process, the same process (5 min sonication, 0.05 mL/mL solution of formaldehyde, and 2.5 hrs) was repeated for PAN-co-MA [72]. Note that plating process as described by ref. [72] (no sonication, 0.005 mL/mL solution of formaldehyde, and 8 minutes of plating time) resulted in non-conductive PAN-co-MA samples.

Table 4.4 Comparison of conductivity/sheet resistance of current collectors.

Sample	Conductivity $\left(\frac{S}{cm}\right)$	Sheet resistance $\left(\frac{\Omega}{\square}\right)$
Carbon paper	193.85 ± 0.05	0.12 ± 0.05
Carbon cloth	25.50 ± 0.49	1.55 ± 0.24
Copper plated lignin	596.34 ± 0.69	0.10 ± 0.05
Copper plated PAN-co-MA	263.57 ± 0.39	0.23 ± 0.15

Chapter 5: Deposition of MnO₂ on Copper Plated Lignin and Electrochemical Performance of the Lignin-based Zn-MnO₂ Battery

5.1 Introduction

In this chapter, morphology, chemical composition, and crystal structure of the deposited MnO₂ on copper plated lignin is analyzed through SEM, EDS, XRD, and XPS. Then, the lignin-based MnO₂ electrode is assembled within a Zn-MnO₂ battery, and the electrochemical performance is analyzed and compared to carbon paper.

5.2 Deposited MnO₂ on Plated 175 °C Lignin

Before the MnO₂ electrode can be electrochemically analyzed, one needs to ensure that MnO₂ is successfully deposited on the plated lignin. Furthermore, the crystal structure of MnO₂ influences its electrochemical performance; for example, β -MnO₂'s specific capacity is lowest compared to α , γ , and δ -MnO₂ [197]. The smaller capacity is due to β -MnO₂'s inability to incorporate zinc ions well, because of its narrow tunnels [24]. In this work, however, the objective is to analyze the current collector. Thus, the electrochemical performance of lignin-based current collector is to be compared to the currently used carbon paper (lower sheet resistance compared to carbon cloth, see Table 4.4) [22], [135], [196], given the same MnO₂ paste (recipe in section 2.5).

Figure 5.1 shows the morphology of the deposited MnO₂ under SEM. The cross section shows that the lignin fibers have collapsed onto each other (see Figure 5.2 for elemental EDS mapping), confirming again that the 175 °C sample is not structurally stable.

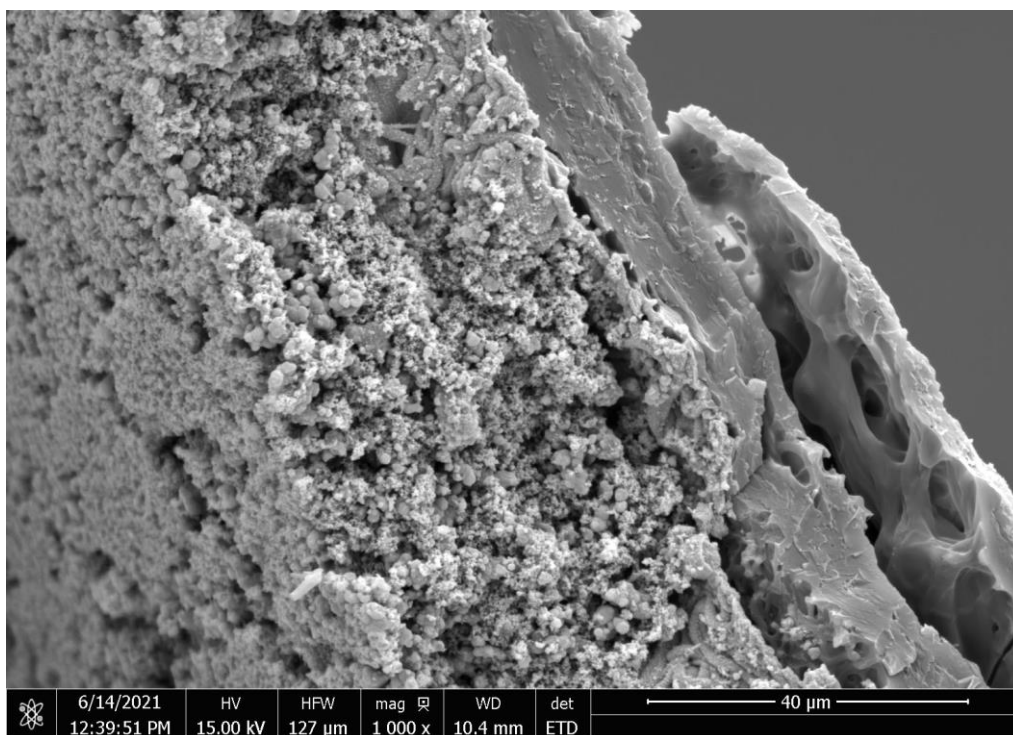
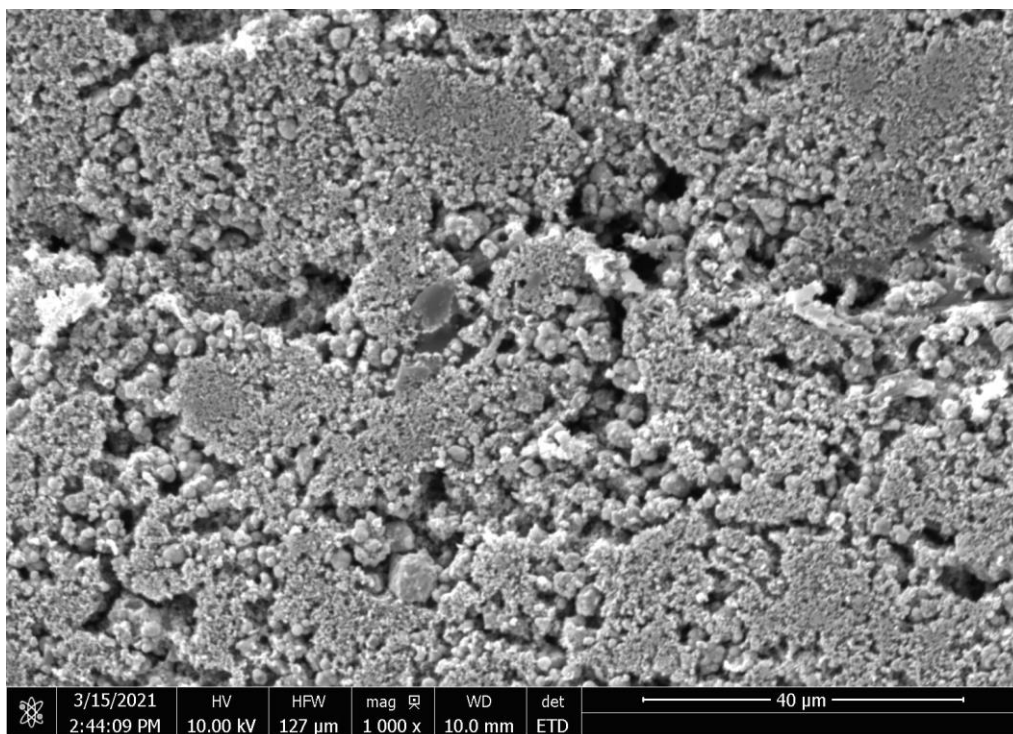


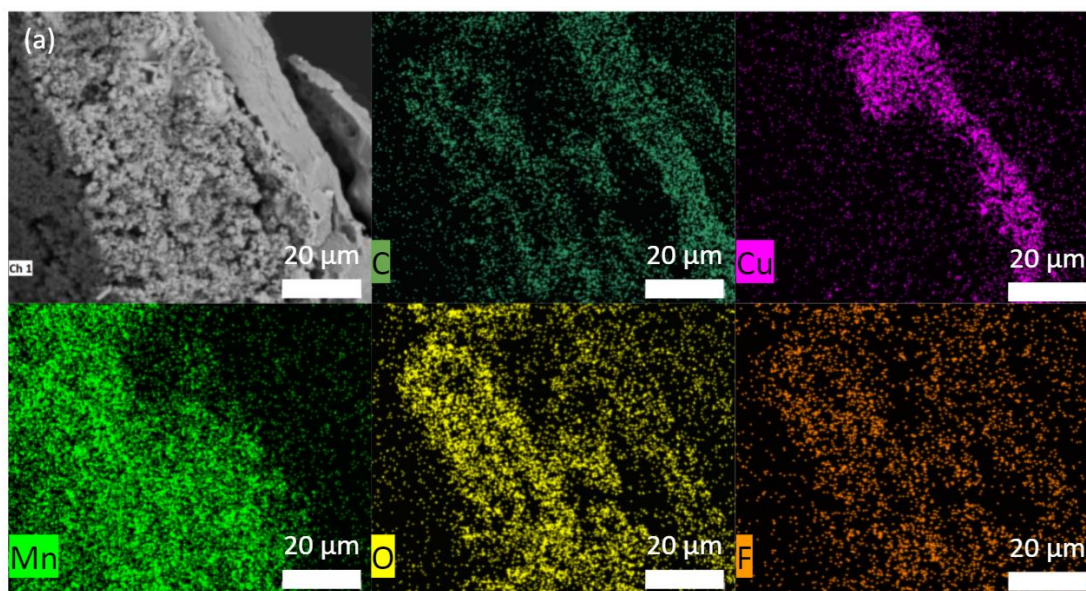
Figure 5.1 SEM of deposited MnO₂ on plated 175 °C lignin. (a) surface. (b) cross section.

5.2.1 Energy Dispersive Spectroscopy of the Deposited MnO₂ on Plated 175 °C Lignin

Figure 5.2 reveals the different layers of the MnO₂ electrode, consisting of lignin, the copper plating, and the active material (MnO₂). Given the carbon black content in the MnO₂ paste, one can expect to have carbon mapping throughout the sample. Table 5.1 demonstrates the mass percentage of each element, excluding the gold coating. Small amounts of fluorine is from PVDF, which acts as a binder in MnO₂ paste [134], [135].

Table 5.1 EDS elemental mass % on the surface of deposited MnO₂ on copper plated 175 °C lignin.

Element	Deposited MnO ₂ Mass %
Carbon	14.76
Oxygen	10.64
Manganese	68.99
Fluorine	5.60



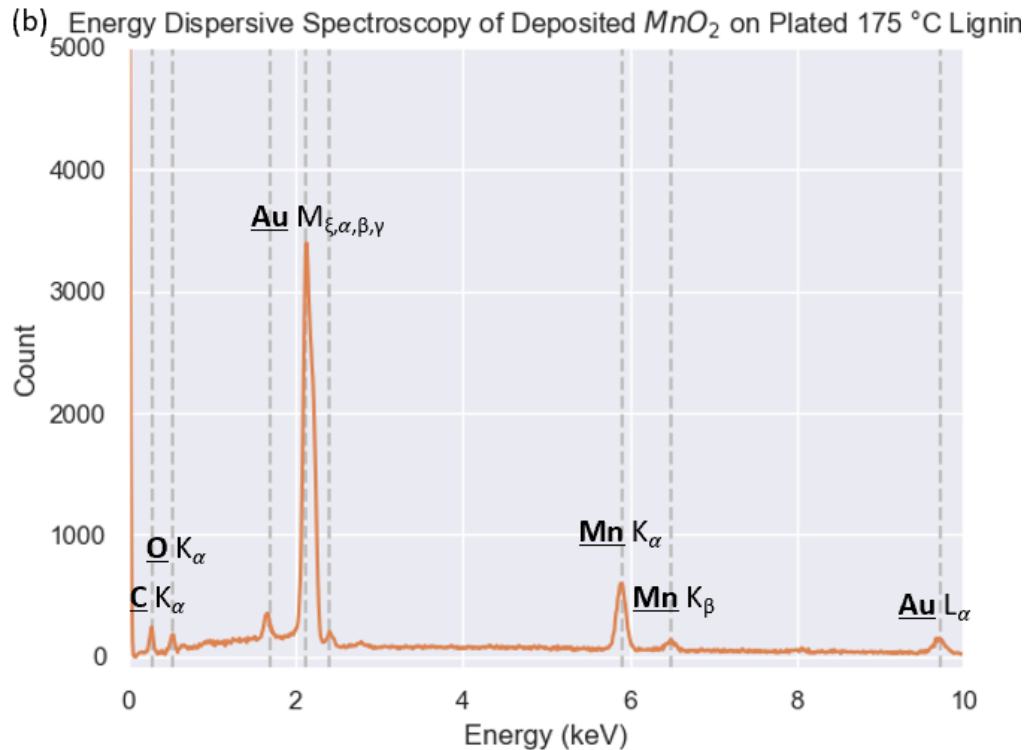


Figure 5.2 EDS of deposited MnO_2 on copper plated 175 °C lignin. (a) elemental mapping of the cross section. (b) spectrum on the MnO_2 surface. C K_{α} , O K_{α} , Au $M_{\xi,\alpha,\beta,\gamma}$, Mn K_{α} , Mn K_{β} , Au L_{α} values are from ref. [167], [168], [186].

5.2.2 X-ray Diffraction of the Deposited MnO_2 on Plated 175 °C Lignin

Figure 5.3 confirms the crystal structure of the deposited MnO_2 . With peaks at around 28.9, 37.5, 56.8, and 72.4°, one can conclude that the crystal structure is β - MnO_2 [197], [198]. The other peaks belong to carbon black at around 24.2 and 42.6°, corresponding to (002) and (100) graphitic planes, respectively [199], [200].

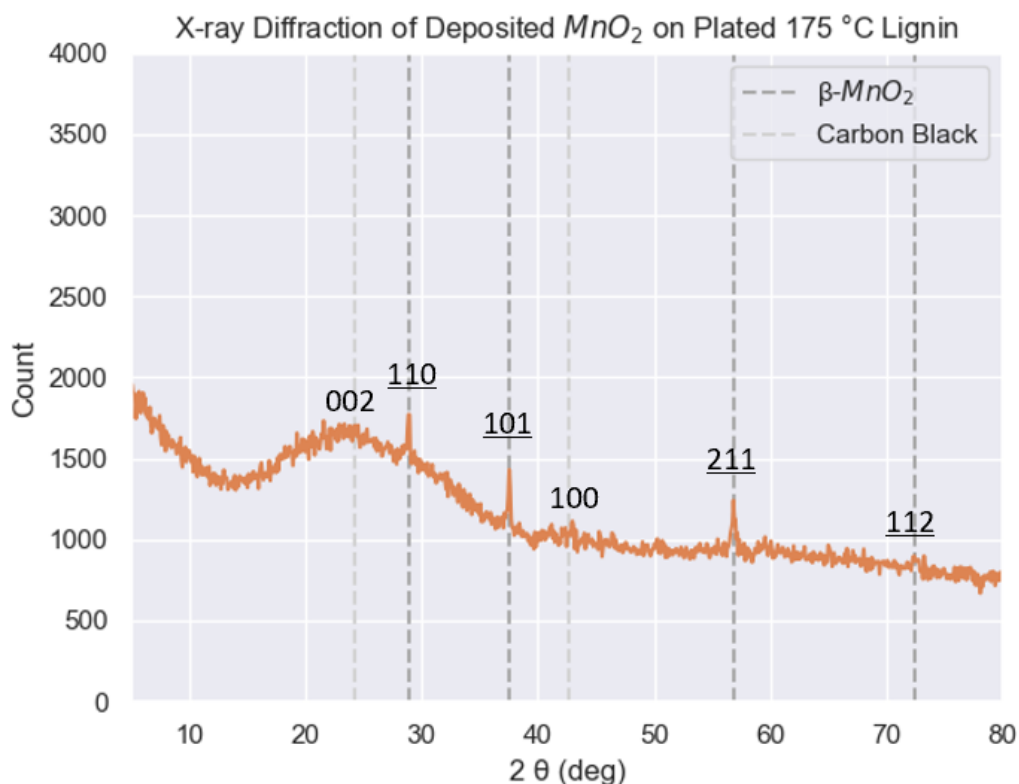


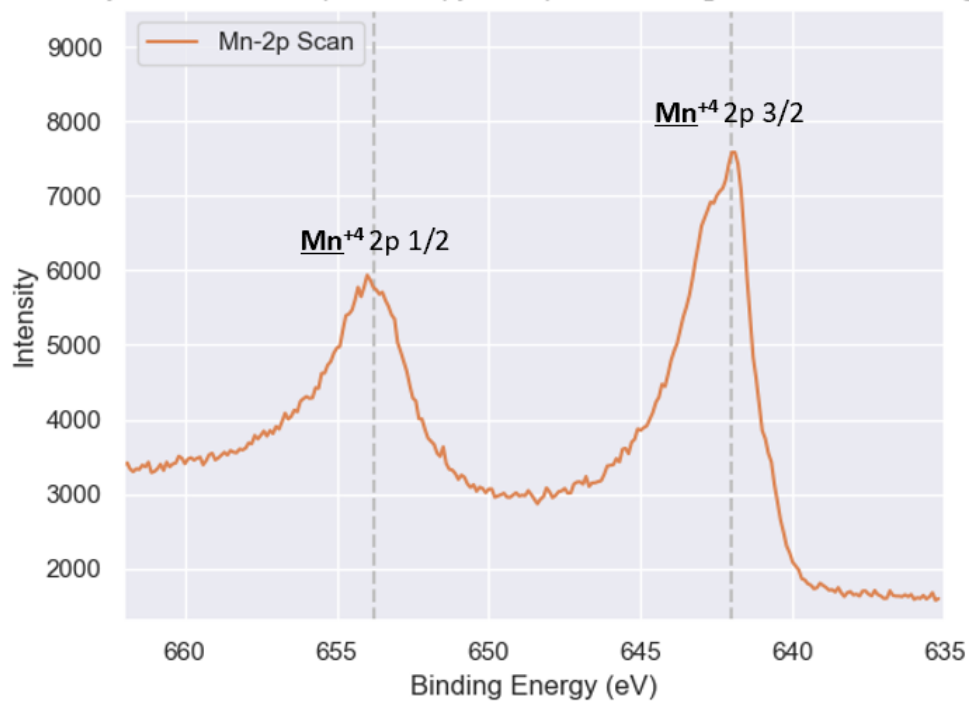
Figure 5.3 XRD of deposited MnO_2 on plated 175 °C lignin.

5.2.3 X-ray Photoelectron Spectroscopy of the Deposited MnO_2 on Plated 175 °C Lignin

Manganese has six stable oxidation states (0, II, III, IV, VI, and VIII); three of which have multiplet splitting (II, III, and IV) and overlapping binding energies. As one can imagine, these properties of Mn make it difficult to perform XPS analysis [201]. Here, we start by comparing the XPS result to $\beta\text{-MnO}_2$, as suggested by XRD. The peaks at 642 and 653.8 eV are ascribed to Mn^{+4} [202]–[204] and the unsmooth curvature is due to the multiplet splitting (642.7 eV) [201].

The O-1s peaks are from O^{2-} (529.5 eV), OH^- (531.2 eV), and H_2O (532.8 eV) bonds, corresponding to lattice, adsorbed, and hydrated/carbonated oxygen species, respectively [148], [205]–[208] (Figure 5.4). Hence, MnO_2 is present on the sample.

(a) X-ray Photoelectron Spectroscopy of Deposited MnO_2 on Plated 175 °C Lignin



(b)

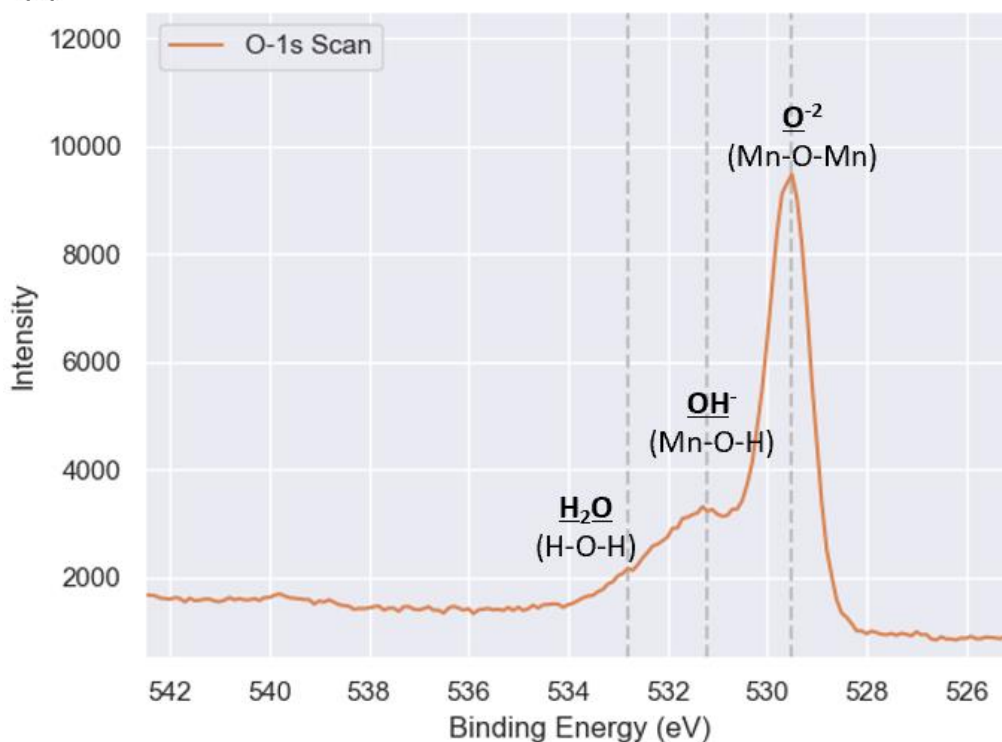


Figure 5.4 XPS of deposited MnO_2 on copper plated 175 °C lignin. (a) Mn 2p narrow scan. (b) O 1s narrow scan. Mn 2p, and O 1s values were provided by 4D LABS and confirmed through ref. [148], [202]–[206].

5.3 Electrochemical Performance of the Lignin-based Zn-MnO₂ Battery

In this section, the electrochemical performance of the battery is tested. Zinc foil is used as the counter electrode. Lignin current collector or carbon paper (control sample) brush-coated with β -MnO₂ are used as the working electrode. The electrolyte is made from 2 M ZnSO₄ and 0.2 M MnSO₄ [144]. The cell is assembled in a beaker to perform the following preliminary tests. This 2-electrode setup will allow for the study of capacity, Coulombic efficiency, cycling performance, and rate capability [209].

Lignin-based and carbon paper-based electrodes have a mass loading of about 2.39 ± 0.06 and 2.21 ± 0.19 mg/cm², respectively (MnO₂ mass per surface area of the current collector). Thickness and density of the MnO₂ layer on the lignin-based current collector are about 36.53 ± 8.78 μ m and 0.31 ± 0.06 g/cm³, respectively. The thickness and density of the MnO₂ layer on the carbon paper are 28.72 ± 2.54 μ m and 0.05 ± 0.19 g/cm³, respectively. The density is calculated based on the mass of active material, the surface area and thickness of the entire current collector. Compared to literature, the mass loading is slightly higher [22], [24], [149], [150], [210] and density is lower [8], [211]. For the following sections, battery with lignin-based current collector is simply denoted as lignin battery and the battery with carbon paper current collector is denoted as carbon paper battery.

5.3.1 Cyclic Voltammetry (CV)

Figure 5.5 presents the cyclic voltammograms (CV) of the assembled batteries at 0.1 mV/s scan rate within 1 – 1.8 V range [24], [146], [147], [212]. Two pairs of redox peaks are visible around 1.58/1.38 V and 1.56/1.20 V for the lignin battery, and 1.60/1.36 V and 1.56/1.25 V for the

carbon paper one. The two-step reduction peaks (1.38 and 1.2 V) correspond to insertion of H^+ and Zn^{+2} into the MnO_2 host, respectively, causing the reduction of Mn^{+4} to Mn^{+3} . The oxidation peaks (1.58 and 1.56 V) correspond to extraction of the H^+ and Zn^{+2} species [144], [147], [213]. The polarization – ΔV or loss or peak separation – of the two current collector indicates better kinetics/reversibility for H^+ insertion/extraction in lignin and better reversibility for Zn^{+2} insertion/extraction in the carbon paper current collector [22], [146], [214].

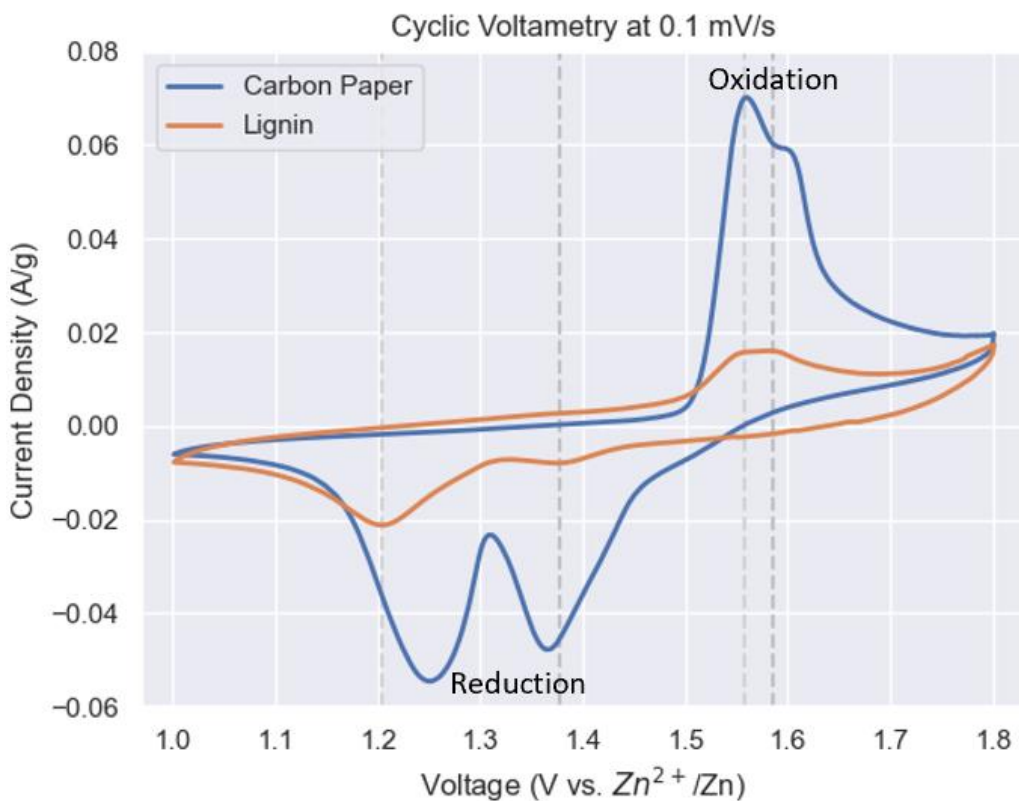


Figure 5.5 CV curves of lignin and carbon paper batteries at scan rate of 0.1 mV/s.

The difference between peak currents can be ascribed to the slower transfer of electrons in the lignin battery [215]. This slower electron transfer can be linked to electrode surface kinetics (i.e., charge transfer) (See section 5.3.6 for further information on polarization).

5.3.2 Galvanostatic Charge – Discharge (GCD)

Figure 5.6 presents the relationship between voltage and specific capacity at current density of 0.1 A/g (per mass of active MnO₂) [54], [146], [216]. There are two tilting discharge plateaus at around ~ 1.2 and 1.38 V; consistent with the CV results [22], [24], [149].

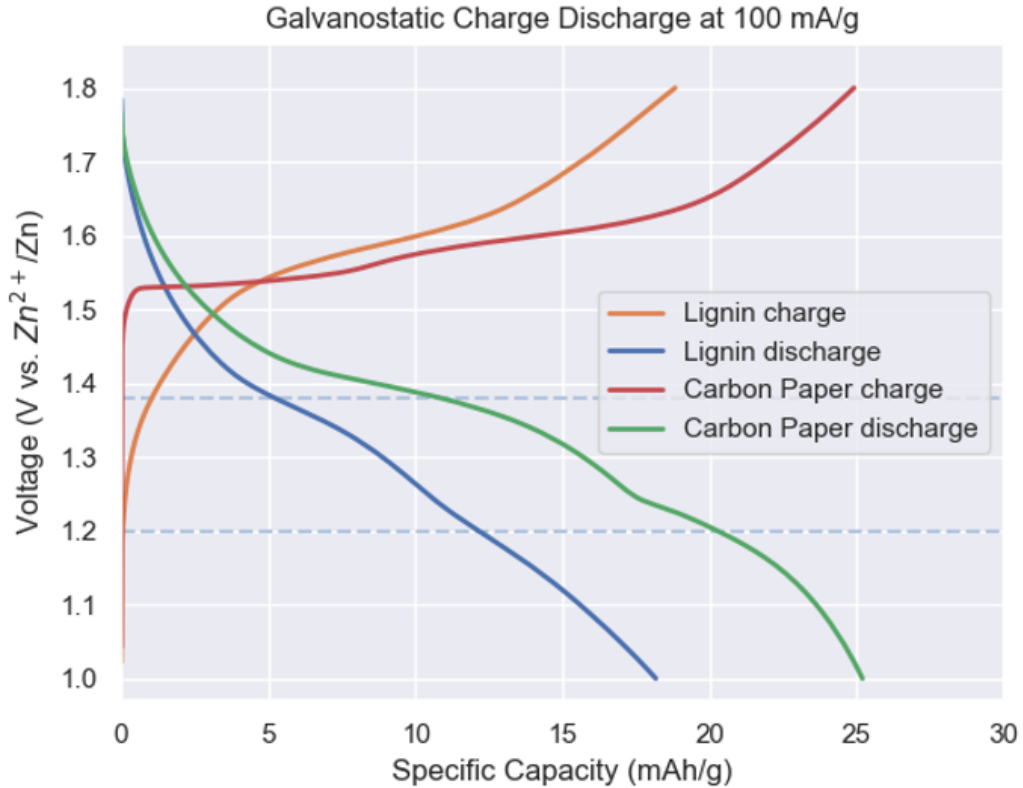


Figure 5.6 GCD curves of lignin and carbon paper batteries at current density of 0.1 A/g (per active MnO₂).

The smaller specific capacity of the lignin battery can be related to its higher polarization [217], [218], consistent with the CV results (see section 5.3.6 for more information). Despite the higher polarization, the lignin current collector still has a capacity (18.17 mAh/g - per mass of active MnO₂) very close to the carbon paper (25.19 mAh/g - per mass of active MnO₂).

5.3.3 Rate Capability

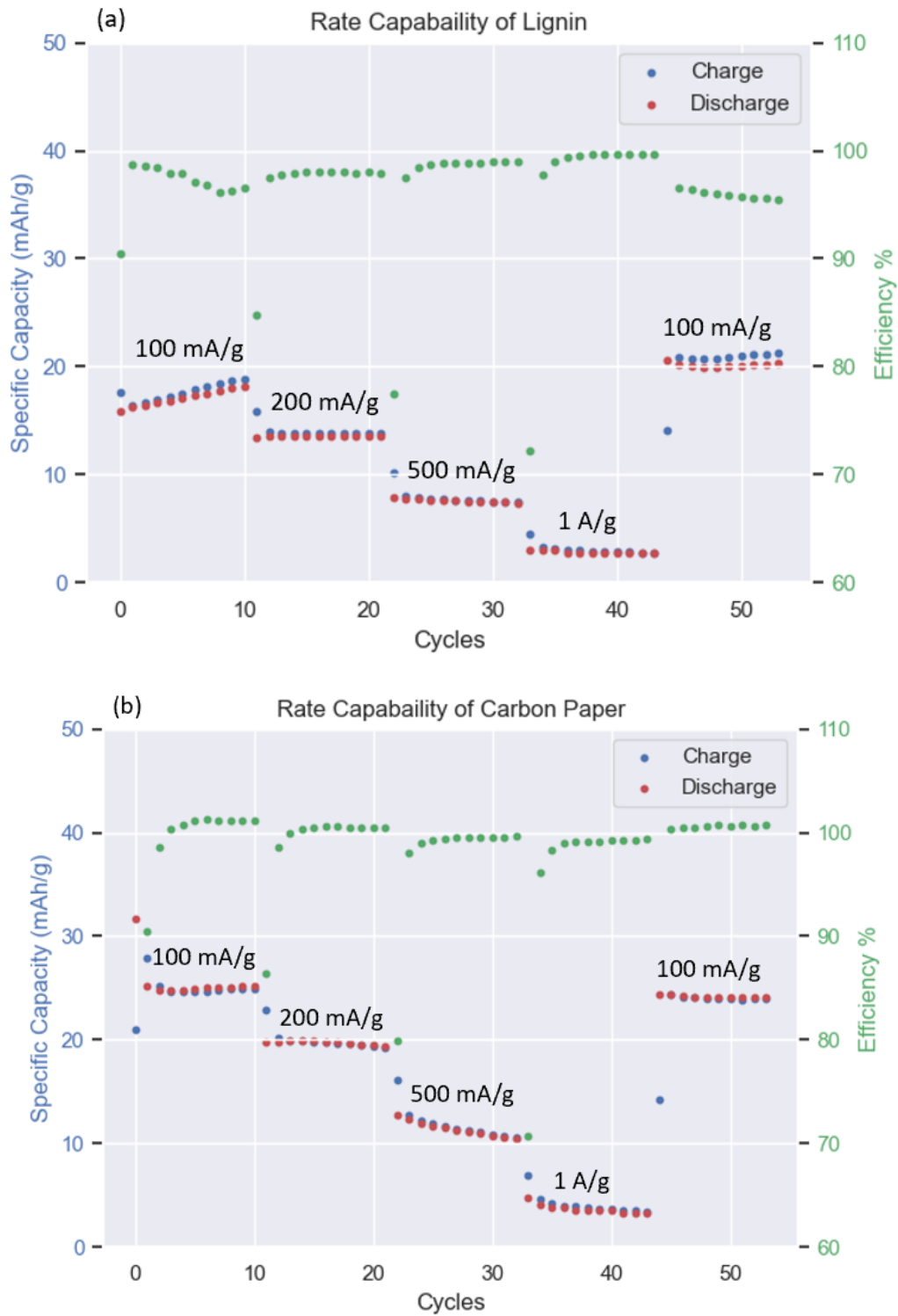


Figure 5.7 Rate capabilities of (a) lignin battery. (b) carbon paper battery. Current densities are chosen based on ref. [149], [212] and are based on mass of active MnO_2 .

Rate capability is an indication of battery polarization at high current. Higher loss and polarization corresponds to lower capacity [217], [218]. In literature, rate capability is presented in terms of capacity [22], [24], [135], [144], [204], [212], [219].

Figure 5.7 illustrates the rate capabilities of lignin and carbon paper batteries. Due to the higher polarization (smaller capacity) of the lignin current collector, its rate capability is lower than the carbon paper [218] (taking specific capacities at 1 A/g as the baseline).

5.3.4 Cycle Life

Cycle life (cycling performance/stability) is the number of charge/discharge cycles before the battery's capacity drops to about 80% of its initial value [220]–[222]. In literature, cycling performance is reported as the specific capacity vs. cycles [24], [144], [149], [150].

Cycling performance for the two current collectors is depicted in Figure 5.8 at 200 mA/g (per mass of active MnO₂) [144], [149], [150]. As described before in section 5.3.2, the initial capacity of the lignin current collector is lower due to its higher polarization; however, it manages to retain 94.4% of its initial capacity (14.27 mAh/g - per mass of active MnO₂) over 1400 cycles.

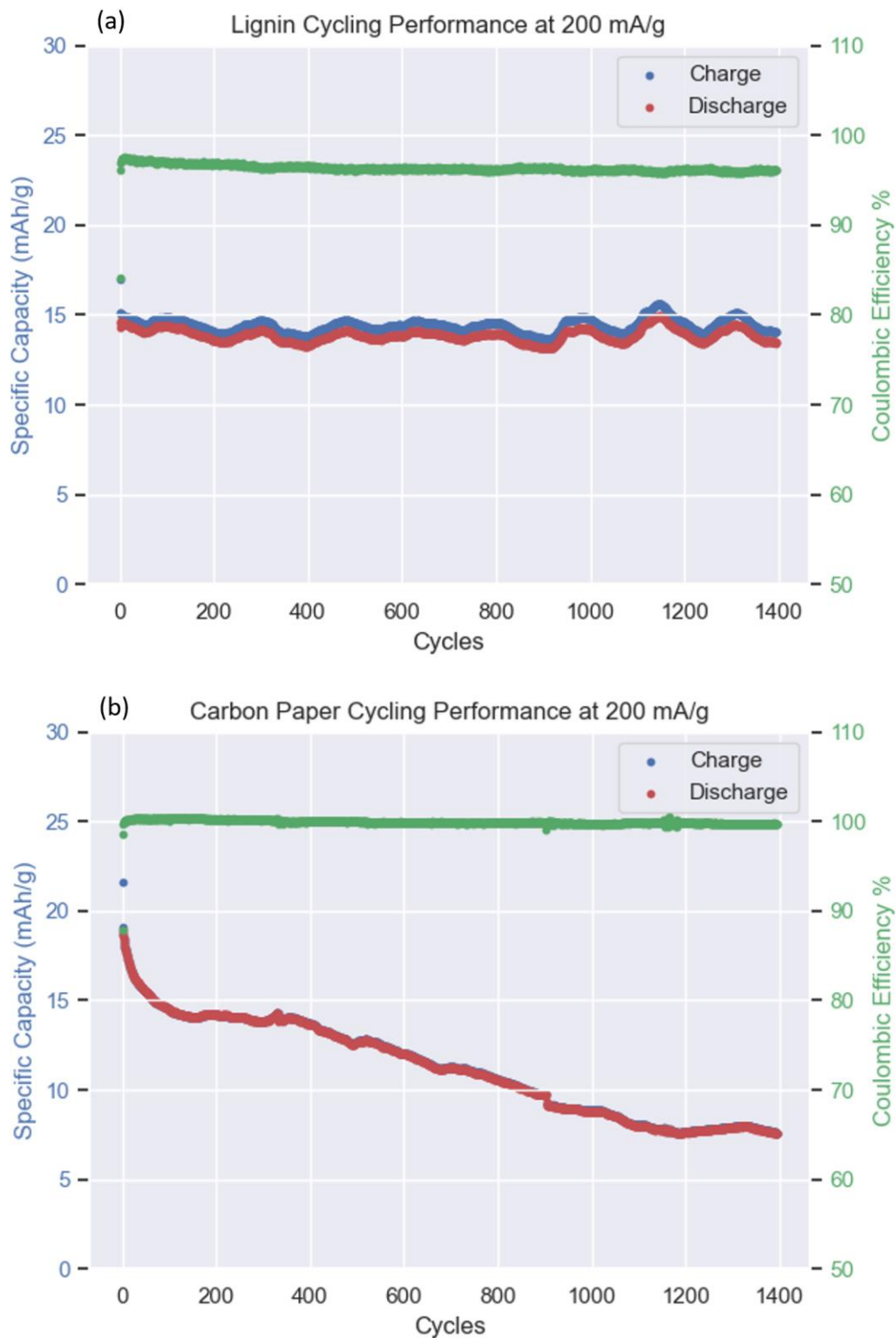


Figure 5.8 Cycling performance of (a) lignin battery. (b) carbon paper battery. at 200 mA/g (per active MnO₂).

Interestingly, the carbon paper battery loses its capacity rapidly, with about 39.9% capacity retention over 1400 cycles. Carbon paper battery reaches 80% retention in only 60 cycles. The cycling stability of carbon paper is, therefore, far lower than the lignin battery.

5.3.5 Electrochemical Impedance Spectroscopy (EIS)

Figure 5.9 depicts the EIS results of the two batteries. Figure 5.10 shows the equivalent circuit chosen to fit the data in Figure 5.9 [151], [152], [197]. R_b is the bulk resistance – resistance from current collector, electrolyte solution, electrode active materials, and the binder. The two parallel RQ components are illustrated by the two semi-circles. R_1 and R_2 are related to electrode/electrolyte interface and charge transfer; however, their exact origin is under investigation [151]. Q_1 and Q_2 , named constant phase element, are associated with non-ideal double-layer capacitors (i.e., surface roughness, leaky capacitors, and non-uniform current distribution [223]). W , slope of the diagonal line, is known as the Warburg impedance; indicating mass transfer and ion diffusion rate [144], [149], [151], [152].

From fitting the equivalent circuit in Figure 5.10 to Figure 5.9's data, one can obtain the equivalent circuit parameters, as indicated in Table 5.2. The results in Table 5.2 confirm the larger polarization of the lignin battery (see section 5.3.6 for more information). The EIS difference between the two current collectors is mostly due to the interfacial, charge transfer, and Warburg impedances [152].

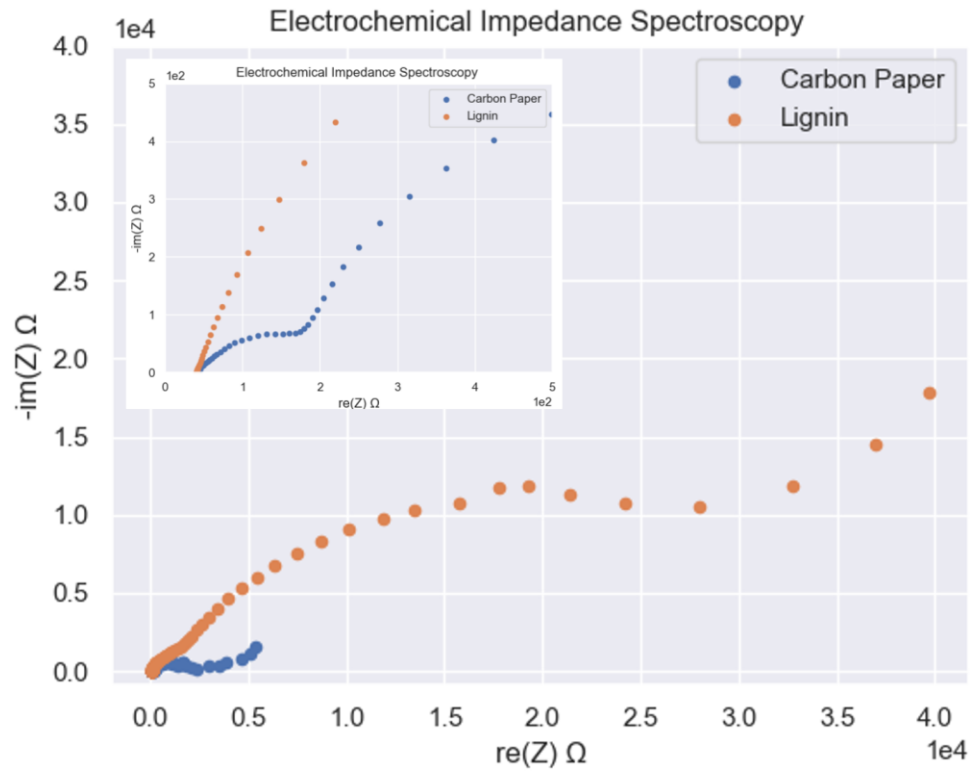


Figure 5.9 EIS of lignin and carbon paper batteries. Inset is zoomed in to about 500 Ω on the real axis.

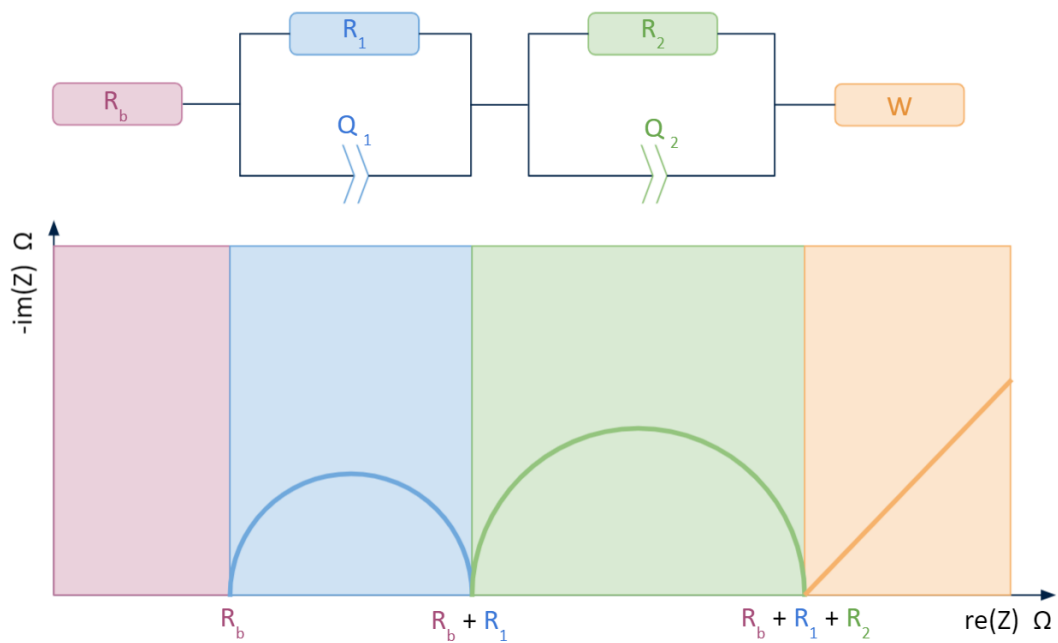


Figure 5.10 Equivalent circuit for fitting to EIS data.

Table 5.2 Equivalent circuit parameters.

Equivalent Circuit Parameter	Lignin	Carbon Paper
R_b [Ω]	39.65	44.28
R_1 [Ω]	1000	114.4
Q_1 [$S \cdot s^n$]	$0.99 E - 6$	$2.07 E - 6$
R_2 [Ω]	$3.66 E + 4$	$1.36 E + 3$
Q_2 [$S \cdot s^n$]	$5.63 E - 6$	$27.31 E - 6$
W [$\Omega \cdot s^{0.5}$]	$4.2 E + 4$	$2.4 E + 3$

5.3.6 Source of Loss

To understand the source of the losses within the battery, one can consider the voltage measured across a battery, which can be expressed by:

$$E = E_{OC} - [\eta_{d,anode} + \eta_{d,cathode}] - iR_b - [\eta_{ct,anode} + \eta_{ct,cathode}] \quad \text{Equation 5.1}$$

In Equation 5.1, E_{OC} is the open circuit potential, η_d is the concentration (mass transfer/diffusion) polarization, i is the operating current, R_b is the bulk/internal resistance of the battery, and η_{ct} is the charge-transfer polarization. Thus, the three sources of loss become concentration, ohmic (iR), and charge-transfer polarizations [26].

Concentration polarization is related to the mass transfer and diffusion of ions [26]. From the dissimilar values of Warburg impedance (section 5.3.5, Table 5.2), one can conclude that the concentration polarization is higher for the lignin battery. Additionally, R_b values are very

similar between the two batteries from the EIS results, thus a similar ohmic drop can be realized between the batteries. The other difference between the lignin and carbon paper battery comes from the charge-transfer polarization. Charge-transfer polarization is associated with the reaction rate [26]. At first glance, one may think that charge-transfer polarizations should be the same between the two batteries, due to the similar active material participating in similar reactions. However, this first glance approach ignores the side reactions between the current collector and the electrolyte.

A closer look at the system reveals that the lignin current collector holds copper on its back side (side that is not brush-coated with MnO_2 - Figure 5.11 and Table 5.3).

Table 5.3 EDS elemental mass % on the back of deposited MnO_2 on copper plated 175 °C lignin.

Elements	Mass % on the back of plated 175 °C lignin brush-coated with MnO_2
Carbon	15.82
Copper	52.10
Manganese	19.72
Oxygen	8.18
Palladium	4.18

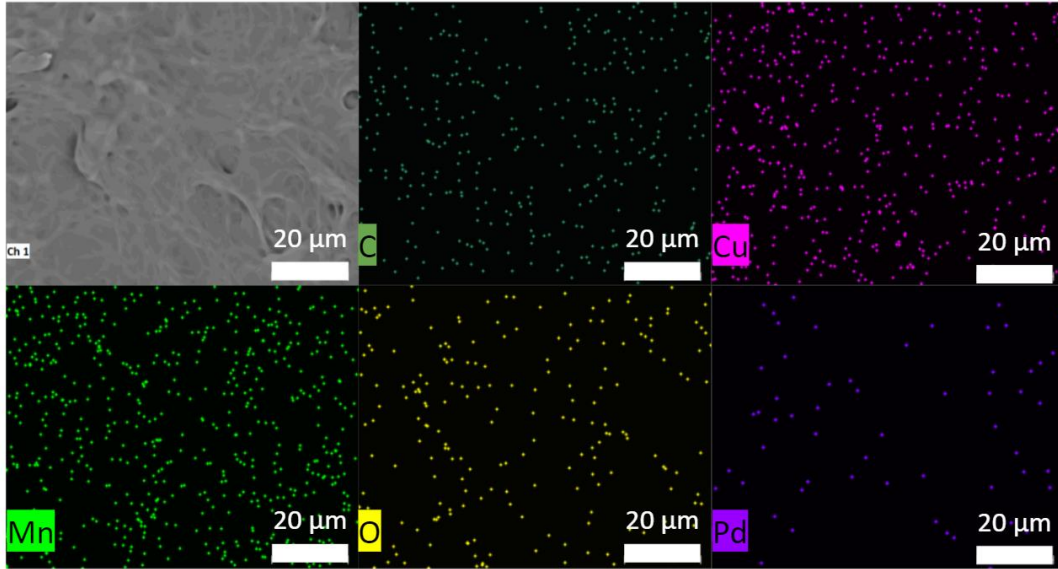


Figure 5.11 EDS elemental mapping of the back side of deposited MnO₂ on copper plated 175 °C lignin.

Copper can participate in side reactions with the mild aqueous electrolyte and produce H₂ [224]. These corrosion and side reactions are the causes for increased polarization, lower reversibility (of Zn²⁺), and smaller capacity of the lignin battery [225], [226]. In addition, Figure 5.1 and Figure 5.2 illustrate the deposition of MnO₂ only on one side of the lignin current collector; however, MnO₂ paste can penetrate between the fibers of the carbon paper (see Fig C.2); therefore, increasing the contact surface area and reducing the bulk resistance [227]. Contrary to the smaller expected bulk resistance for carbon paper, lignin possesses smaller bulk resistance. This can be due to the corroded copper in the electrolyte. It should be noted that copper does not participate in the battery reactions (no peak in CV around 1.1 V Zn²⁺/Zn); however, its diffusion and charge-transfer polarizations, as well as H₂ production can explain the lower reversibility and capacity of the lignin battery.

5.4 Concluding Remarks

This chapter covers the morphology, crystal structure, and electrochemical performance of the MnO_2 deposited on copper plated lignin. XRD and XPS confirm that the crystal structure is β - MnO_2 .

The electrochemical tests show a larger polarization for the lignin battery as compared to the carbon paper battery. Despite the large polarization, the lignin battery has a capacity close to carbon paper and an excellent cycling performance. This is in agreement with the literature that polarization does not significantly influence the cycling performance [228]. As mentioned in section 1.1, cycle life is one of the most important factors for wearable batteries. Therefore, the lignin current collector is a promising candidate for such wearable batteries. It should be noticed that the performance of both batteries is far below literature (e.g., specific capacity is at least 75 mAh/g at 0.2 A/g (based on cathode) [149], [210]). Additionally, the energy density and power density of the lignin battery are about 25.77 Wh/kg and 372.27 W/kg, respectively (per active MnO_2). For carbon paper, energy and power density are 31.08 Wh/kg and 366.19 W/kg, respectively (per active MnO_2). Thus, further improvement of batteries (e.g., bringing the two electrodes closer [145] or changing the morphology of the current collector to allow for faster electron transfer of the active MnO_2 [134]) is crucial. However, such improvements are beyond the scope of this thesis. Finally, the lignin current collector which was thermostabilized at 200 °C has lower capacity and cycle life compared to both carbon paper and 175 °C lignin batteries. This is likely due to higher copper content on the back of the 200 °C lignin current collector (Appendix D).

Chapter 6: Conclusion and Future Work

6.1 Conclusion

This research investigates the feasibility of developing a conductive current collector from lignin for use in Zn-MnO₂ wearable batteries. In particular, hardwood organosolv lignin is used as a precursor for fabricating fibers that are later thermostabilized. Thermostabilization helps lignin to crosslink and converts palladium (II) acetylacetonate (Pd(acac)₂) to Pd metal. Pd metal is used as a catalyst for electroless copper plating on the thermostabilized lignin fibers. The copper plated lignin fibers are brush-coated with MnO₂ paste to create the working electrode for the Zn-MnO₂ battery. Finally, the electrochemical performance of the assembled battery is analyzed. The findings of this work are summarized as follows:

The first step in this investigation is to electrospin lignin into fibers. Two different batches (69 and 157 BCP) of lignin are used. The initial optimization of 69 BCP based on molecular weight of plasticizer, lignin: plasticizer ratio, and solid content show that 30-99-1-900k, 30-95-5-900k, and 40-99-1-900k produce fibers with the smallest diameter ($1.29 \pm 0.69 \mu\text{m}$, $1.24 \pm 0.46 \mu\text{m}$, and $2.77 \pm 1.81 \mu\text{m}$, respectively). The switch to 157 BCP lignin refines the optimization choice to only 40-99-1-900k, as the other two produce droplets. With the optimized recipe in hand, Pd(acac)₂ can be added to the electrospinning solution. The fibers containing Pd(acac)₂ have smaller diameters due to the added conductivity of Pd.

The second step of the investigation is thermal stabilization (thermostabilization). The results indicate that the sample thermostabilized at 175 °C is not chemically stabilized in the electroless

plating solution or when coated with MnO₂. However, due to the higher surface-to-volume ratio (smaller diameter and higher reactivity) of the 175 °C sample (compared to the most stabilized sample, which is thermostabilized at 200 °C), it is chosen for electroless copper plating and MnO₂ deposition. The X-ray photoelectron spectroscopy results illustrate that Pd metal is present on the 175 °C sample to serve as the catalyst for plating.

The third step is electroless copper plating. First, a plating solution is developed that accommodates the unstable nature of the 175 °C sample, then, the existence of copper is confirmed. The results demonstrate that a solution with 0.05 mL of formaldehyde per mL of solution with 5-minute sonication time over plating time of 2.5 hrs produces fibers with the highest conductivity (and lowest sheet resistance), which meet target value of 575 S/cm (and 0.33 Ω/□ [39]) [8]. Furthermore, copper, copper (I) oxide, and copper (II) oxide are confirmed to be present on the plated sample.

The fourth step is the deposition of MnO₂ on the samples, confirmation of the existence of MnO₂, and its crystal structure. The results reveal that samples have β-MnO₂ crystal structure.

The fifth and final step of this investigation is the analysis of the electrochemical performance of the assembled Zn-MnO₂ battery. The results illustrate the superiority of the lignin current collector compared to the control sample, carbon paper, because of the lignin current collector's longer cycle life. It should be noted that the lignin current collector possesses higher polarization due to the diffusion and side reactions of copper in the electrolyte. Despite the higher

polarization (and the resulting smaller capacity), the lignin current collector shows promise for wearable applications, where longer cycle life is needed.

6.2 Future Work

This thesis is a study on conductive current collectors made from lignin for wearable batteries. However, as with every research, there is room for improvement, which are discussed below:

6.2.1 N.N-dimethylformamide (DMF) Alternatives

N.N-dimethylformamide (DMF), the solvent used in electrospinning solution, is a strong liver toxin, which can be absorbed through skin, inhalation, or ingestion [229]. Therefore, alternatives are highly recommended to be considered. Ethanol has previously been shown to work as solvent for organosolv lignin [98].

6.2.2 Further Weight Reduction of the Zn-MnO₂ Battery

To reduce the weight of the battery, (1) instead of zinc foil, copper plated lignin coated with zinc paste can be used, and/or (2) the back of the lignin current collector can be etched away after deposition of MnO₂. Caution is advised for the etchant in the latter, as the etchant should not etch away the lignin fibers that are plated. Plasma treatment, for example, can be used for surface etching of lignin [230]. After removal of lignin, MnO₂ can be deposited on the back to reduce the side reactions of copper.

6.2.3 Solid-State Electrolyte

Use of solution-based electrolytes can cause leakage in the wearable system. Solid-state electrolytes can prevent leakage as well as dendrite formation on the zinc anode [23], [147]. Thus, their employment within the battery is encouraged. Polyvinyl alcohol (PVA)/LiCl-ZnCl₂-MnSO₄ gel, PVA-ZnCl₂, and PVA-ZnSO₄-based gel have been used as solid-state electrolytes [23], [146], [147].

6.2.4 Higher Viscosity of Electrospinning Solution

As mentioned in section 3.2.2, higher concentration and viscosity are shown to work better for 157 BCP samples. To produce even and bead-less fibers, higher molecular weight (MW) of electrospinning solution can be considered. This higher MW can be from the lignin and/or the plasticizer. A MW of poly (ethylene oxide) (PEO) between 900 k and 4 M may work well.

6.2.5 Flexibility

Lignin fibers are brittle and hard to handle. Polyacrylonitrile-co-methyl-acrylate (PAN-co-MA) fibers are much more flexible (Fig E.1). We recommend combining lignin and PAN-co-MA to fabricate composite fibers with higher flexibility.

Bibliography

- [1] B. Parke and A. Bianchi, “Micro Data: Wearable Devices Contribute to Improved Chronic Disease Management,” *Healthc. Q.*, vol. 18, no. 4, pp. 62–65, 2016, doi: 10.12927/hcq.2016.24548.
- [2] J. R. Loos and E. J. Davidson, “Wearable health monitors and physician-patient communication: The physician’s perspective,” in *Hawaii International Conference on System Sciences*, 2016, pp. 3389–3398, doi: 10.1109/HICSS.2016.422.
- [3] Public Health Agency of Canada, “How Healthy are Canadians?,” 2017.
- [4] World Health Organization, “Ten threats to global health in 2019,” 2019. [Online]. Available: <https://www.who.int/news-room/feature-stories/ten-threats-to-global-health-in-2019>. [Accessed: 13-May-2020].
- [5] World Health Organization (WHO), “Noncommunicable diseases.” [Online]. Available: https://www.who.int/health-topics/noncommunicable-diseases#tab=tab_1. [Accessed: 01-Mar-2021].
- [6] S. C. Mukhopadhyay, *Wearable Electronics Sensors For Safe and Healthy Living*. Springer International Publishing, 2015.
- [7] L. Manjakkal, C. G. Núñez, W. Dang, and R. Dahiya, “Flexible self-charging supercapacitor based on graphene-Ag-3D graphene foam electrodes,” *Nano Energy*, vol. 51, pp. 604–612, Sep. 2018, doi: 10.1016/j.nanoen.2018.06.072.
- [8] W. Luo *et al.*, “Highly Conductive, Light Weight, Robust, Corrosion-Resistant, Scalable, All-Fiber Based Current Collectors for Aqueous Acidic Batteries,” *Adv. Energy Mater.*, vol. 8, p. 1702615, 2018, doi: 10.1002/aenm.201702615.
- [9] Y. Chen *et al.*, “Reduced Graphene Oxide Films with Ultrahigh Conductivity as Li-Ion

- Battery Current Collectors,” *Nano Lett*, vol. 16, pp. 3616–3623, 2016, doi: 10.1021/acs.nanolett.6b00743.
- [10] D. Kilani, B. Mohammad, M. Alhawari, H. Saleh, and M. Ismail, “Introduction to Power Management,” in *Power Management for Wearable Electronic Devices*, Cham: Springer International Publishing, 2020, pp. 1–13.
- [11] C. H. Wang, N. Kurra, M. Alhabeab, J. K. Chang, H. N. Alshareef, and Y. Gogotsi, “Titanium Carbide (MXene) as a Current Collector for Lithium-Ion Batteries,” *ACS Omega*, vol. 3, pp. 12489–12494, Oct. 2018, doi: 10.1021/acsomega.8b02032.
- [12] Y. W. Chong, W. Ismail, K. Ko, and C. Y. Lee, “Energy Harvesting for Wearable Devices: A Review,” *IEEE Sens. J.*, vol. 19, no. 20, pp. 9047–9062, Oct. 2019, doi: 10.1109/JSEN.2019.2925638.
- [13] C. Xu, Y. Song, M. Han, and H. Zhang, “Portable and wearable self-powered systems based on emerging energy harvesting technology,” *Microsystems Nanoeng.*, vol. 7, no. 25, pp. 1–14, Dec. 2021, doi: 10.1038/s41378-021-00248-z.
- [14] A. Khaligh and O. C. Onar, *Solar Energy Harvesting*. CRC Press, 2017.
- [15] V. Vega-Garita, L. Ramirez-Elizondo, N. Narayan, and P. Bauer, “Integrating a photovoltaic storage system in one device: A critical review,” *Progress in Photovoltaics: Research and Applications*, vol. 27. John Wiley and Sons Ltd, pp. 346–370, 01-Apr-2019, doi: 10.1002/pip.3093.
- [16] H. Yuan *et al.*, “Cable-Shaped Lithium–Sulfur Batteries Based on Nitrogen-Doped Carbon/Carbon Nanotube Composite Yarns,” *Macromol. Mater. Eng.*, vol. 304, p. 1900201, Aug. 2019, doi: 10.1002/mame.201900201.
- [17] H. Abdi, B. Mohammadi-ivatloo, S. Javadi, A. Reza Khodaei, and E. Dehnavi, “Energy

- Storage Systems,” in *Distributed Generation Systems*, 2017, pp. 333–368.
- [18] P. Simon, Y. Gogotsi, and B. Dunn, “Where do batteries end and supercapacitors begin?,” *Science*, vol. 343. American Association for the Advancement of Science, pp. 1210–1211, 14-Mar-2014, doi: 10.1126/science.1249625.
- [19] Battery University, “Supercapacitor Information,” 2020. [Online]. Available: https://batteryuniversity.com/learn/article/whats_the_role_of_the_supercapacitor. [Accessed: 08-May-2021].
- [20] “Vancouver, British Columbia, Canada — Sunrise, Sunset, and Daylength, December 2020,” *Time and Date*. [Online]. Available: <https://www.timeanddate.com/sun/canada/vancouver?month=12&year=2020>. [Accessed: 08-May-2021].
- [21] T. Pandolfo, V. Ruiz, S. Sivakkumar, and J. Nerkar, “General Properties of Electrochemical Capacitors,” in *Supercapacitors: Materials, Systems, and Applications*, 1st ed., Weinheim, Germany: Wiley-VCH Verlag GmbH & Co. KGaA, 2013, pp. 69–109.
- [22] C. Wang *et al.*, “ γ -MnO₂ nanorods/graphene composite as efficient cathode for advanced rechargeable aqueous zinc-ion battery,” *J. Energy Chem.*, vol. 43, pp. 182–187, Apr. 2020, doi: 10.1016/j.jechem.2019.08.011.
- [23] Y. Jiang, D. Ba, Y. Li, and J. Liu, “Noninterference Revealing of ‘Layered to Layered’ Zinc Storage Mechanism of δ -MnO₂ toward Neutral Zn–Mn Batteries with Superior Performance,” *Adv. Sci.*, vol. 7, p. 1902795, Mar. 2020, doi: 10.1002/advs.201902795.
- [24] N. Zhang *et al.*, “Rechargeable aqueous zinc-manganese dioxide batteries with high energy and power densities,” *Nat. Commun.*, vol. 8, no. 405, pp. 1–9, Dec. 2017, doi: 10.1038/s41467-017-00467-x.

- [25] R. Borah, F. R. Hughson, J. Johnston, and T. Nann, “On battery materials and methods,” *Mater. Today Adv. J.*, vol. 6, p. 100046, 2020, doi: 10.1016/j.mtadv.2019.100046.
- [26] D. Linden and T. B. Reddy, *Handbook of Batteries*. 2002.
- [27] M. Yamada, T. Watanabe, T. Gunji, J. Wu, and F. Matsumoto, “Review of the Design of Current Collectors for Improving the Battery Performance in Lithium-Ion and Post-Lithium-Ion Batteries,” *Electrochem*, vol. 1, pp. 124–159, 2020, doi: 10.3390/electrochem1020011.
- [28] S. W. Kim and K. Y. Cho, “Current Collectors for Flexible Lithium Ion Batteries: A Review of Materials,” *J. Electrochem. Sci. Technol.*, vol. 6, no. 1, pp. 1–6, 2015, doi: 10.5229/JECST.2015.6.1.1.
- [29] Y. Yue and H. Liang, “3D Current Collectors for Lithium-Ion Batteries: A Topical Review,” *Small Methods*, vol. 2, p. 1800056, Aug. 2018, doi: 10.1002/smt.201800056.
- [30] “A new approach boosts lithium-ion battery efficiency and puts out fires, too,” *SLAC National Accelerator Laboratory*, 2020. [Online]. Available: <https://www6.slac.stanford.edu/news/2020-10-15-new-approach-boosts-lithium-ion-battery-efficiency-and-puts-out-fires-too.aspx>. [Accessed: 06-May-2021].
- [31] “New current collector makes batteries lighter, safer and more efficient,” *Materials Today*, 2020. [Online]. Available: <https://www.materialstoday.com/energy/news/new-current-collector-batteries/>. [Accessed: 06-May-2021].
- [32] L. Hu *et al.*, “Highly conductive paper for energy-storage devices,” *Proc. Natl. Acad. Sci.*, vol. 106, no. 51, pp. 21490–21494, 2009, doi: 10.1073/pnas.0908858106.
- [33] M. Wu, Y. Li, B. Yao, J. Chen, C. Li, and G. Shi, “A high-performance current collector-free flexible in-plane micro-supercapacitor based on a highly conductive reduced

- graphene oxide film,” *J. Mater. Chem. A*, vol. 4, p. 16213, Oct. 2016, doi: 10.1039/c6ta06846d.
- [34] A. Sumboja, X. Wang, J. Yan, and P. S. Lee, “Nanoarchitected current collector for high rate capability of polyaniline based supercapacitor electrode,” *Electrochim. Acta*, vol. 65, pp. 190–195, 2012, doi: 10.1016/j.electacta.2012.01.046.
- [35] M. Notarianni, J. Liu, F. Mirri, M. Pasquali, and N. Motta, “Graphene-based supercapacitor with carbon nanotube film as highly efficient current collector,” *Nanotechnology*, vol. 25, p. 435405, Oct. 2014, doi: 10.1088/0957-4484/25/43/435405.
- [36] X. Chen, H. Huang, L. Pan, T. Liu, and M. Niederberger, “Fully Integrated Design of a Stretchable Solid-State Lithium-Ion Full Battery,” *Adv. Mater.*, vol. 31, p. 1904648, Oct. 2019, doi: 10.1002/adma.201904648.
- [37] L. Hu, H. Wu, F. La Mantia, Y. Yang, and Y. Cui, “Lightweight - Thin, Flexible Secondary Li-Ion Paper Batteries,” *ACS Nano*, vol. 4, no. 10, pp. 5843–5848, 2010, doi: 10.1021/nn1018158.
- [38] K. Wang *et al.*, “Super-Aligned Carbon Nanotube Films as Current Collectors for Lightweight and Flexible Lithium Ion Batteries,” *Adv. Funct. Mater.*, vol. 23, pp. 846–853, Feb. 2013, doi: 10.1002/adfm.201202412.
- [39] K. Wang *et al.*, “Super-aligned carbon nanotube films with a thin metal coating as highly conductive and ultralight current collectors for lithium-ion batteries,” *J. Power Sources*, vol. 351, pp. 160–168, 2017, doi: 10.1016/j.jpowsour.2017.03.081.
- [40] C. Chen *et al.*, “Highly Conductive, Lightweight, Low-Tortuosity Carbon Frameworks as Ultrathick 3D Current Collectors,” *Adv. Energy Mater.*, vol. 7, p. 1700595, Sep. 2017, doi: 10.1002/aenm.201700595.

- [41] American Heart Association, “Electrocardiogram (ECG or EKG).” [Online]. Available: <https://www.heart.org/en/health-topics/heart-attack/diagnosing-a-heart-attack/electrocardiogram-ecg-or-ekg>. [Accessed: 08-May-2021].
- [42] Heart and Stroke Foundation, “Electrocardiogram.” [Online]. Available: <https://www.heartandstroke.ca/heart-disease/tests/electrocardiogram>. [Accessed: 08-May-2021].
- [43] Apple, “Apple Watch Battery and Performance ,” 2020. [Online]. Available: <https://support.apple.com/en-ca/HT210551>. [Accessed: 08-May-2021].
- [44] Analog Devices, “AD8232 Datasheet and Product Info .” [Online]. Available: <https://www.analog.com/en/products/ad8232.html?doc=AD8232.pdf#product-overview>. [Accessed: 08-May-2021].
- [45] M. Shao, Z. Zhou, G. Bin, Y. Bai, and S. Wu, “A Wearable Electrocardiogram Telemonitoring System for Atrial Fibrillation Detection,” *Sensors*, vol. 20, p. 606, Feb. 2020, doi: 10.3390/s20030606.
- [46] Clean Energy Institute, “Lithium-Ion Battery ,” *University of Washington*. [Online]. Available: <https://www.cei.washington.edu/education/science-of-solar/battery-technology/>. [Accessed: 08-May-2021].
- [47] Tektronix, “Lithium-Ion Battery Maintenance Guidelines,” *Tektronix*. [Online]. Available: www.tektronix.com. [Accessed: 21-Jul-2021].
- [48] R. Moshtev and B. Johnson, “State of the art of commercial Li ion batteries,” *J. Power Sources*, vol. 91, pp. 86–91, Dec. 2000, doi: 10.1016/S0378-7753(00)00458-4.
- [49] J. Murray, “Is the Nobel Prize-winning lithium-ion battery really having a positive impact on the environment?,” *NS Energy*, 2019. [Online]. Available:

<https://www.nsenergybusiness.com/features/lithium-ion-battery-environmental-impact/>.
[Accessed: 09-May-2021].

- [50] University of Birmingham, “New high-capacity sodium-ion could replace lithium in rechargeable batteries,” *Phys.Org*, 2018. [Online]. Available: <https://phys.org/news/2018-09-high-capacity-sodium-ion-lithium-rechargeable-batteries.html>. [Accessed: 19-Aug-2020].
- [51] C. Early, “The new ‘gold rush’ for green lithium,” *BBC Future*, 2020. [Online]. Available: <https://www.bbc.com/future/article/20201124-how-geothermal-lithium-could-revolutionise-green-energy>. [Accessed: 09-May-2021].
- [52] D. Chao *et al.*, “An Electrolytic Zn–MnO₂ Battery for High-Voltage and Scalable Energy Storage,” *Angew. Chemie Int. Ed.*, vol. 58, pp. 7823–7828, Jun. 2019, doi: 10.1002/anie.201904174.
- [53] C. C. Yang and S. J. Lin, “Improvement of high-rate capability of alkaline Zn-MnO₂ battery,” *J. Power Sources*, vol. 112, pp. 174–183, 2002.
- [54] X. Guo, J. Zhou, C. Bai, X. Li, G. Fang, and S. Liang, “Zn/MnO₂ battery chemistry with dissolution-deposition mechanism,” *Mater. Today Energy J.*, vol. 16, p. 100396, 2020, doi: 10.1016/j.mtener.2020.100396.
- [55] K. Schulte, “Abundance of Elements in Earth’s Crust,” *Geosciences LibreTexts*, 2020. [Online]. Available: [https://geo.libretexts.org/Bookshelves/Geology/Book%3A_Fundamentals_of_Geology_\(Schulte\)/02%3A_Rock_Forming_Minerals/2.08%3A_Abundance_of_Elements_in_Earth%27s_Crust](https://geo.libretexts.org/Bookshelves/Geology/Book%3A_Fundamentals_of_Geology_(Schulte)/02%3A_Rock_Forming_Minerals/2.08%3A_Abundance_of_Elements_in_Earth%27s_Crust). [Accessed: 09-May-2021].
- [56] T. Helmenstine, “Abundance of Elements in Earth’s Crust - Periodic Table and List,”

- Science Notes* , 2020. [Online]. Available: <https://sciencenotes.org/abundance-of-elements-in-earths-crust-periodic-table-and-list/>. [Accessed: 09-May-2021].
- [57] L. Learning, “Reading: Abundance of Elements in Earth’s Crust.” [Online]. Available: <https://courses.lumenlearning.com/geology/chapter/reading-abundance-of-elements-in-earths-crust/>. [Accessed: 20-Jun-2020].
- [58] “Lithium Price ,” *Metalary*, 2018. [Online]. Available: <https://www.metalary.com/lithium-price/>. [Accessed: 09-May-2021].
- [59] “Zinc Price,” *Metalary*, 2018. [Online]. Available: <https://www.metalary.com/zinc-price/>. [Accessed: 09-May-2021].
- [60] “Manganese Price ,” *Metalary*, 2018. [Online]. Available: <https://www.metalary.com/manganese-price/>. [Accessed: 09-May-2021].
- [61] F. Ko, Y. Wan, and Cambridge University Press, “Fundamentals of Polymers,” in *Introduction to Nanofiber Materials*, Cambridge United Kingdom: Cambridge University Press, 2014, pp. 13–43.
- [62] K. Wei *et al.*, “Development of electrospun metallic hybrid nanofibers via metallization,” *Polym. Adv. Technol.*, vol. 21, pp. 746–751, Oct. 2010, doi: 10.1002/pat.1490.
- [63] S. Vahid Ebadi, H. Fashandi, D. Semnani, B. Rezaei, and A. Fakhrali, “Overcoming the potential drop in conducting polymer artificial muscles through metallization of electrospun nanofibers by electroplating process,” *Smart Mater. Struct.*, vol. 29, p. 085036, 2020, doi: 10.1088/1361-665X/ab98ed.
- [64] H. R. Kim, T. Ito, B. S. Kim, Y. Watanabe, and I. S. Kim, “Mechanical Properties, Morphologies, and Microstructures of Novel Electrospun Metallized Nanofibers,” *Adv. Eng. Mater.*, vol. 13, no. 5, pp. 376–382, May 2011, doi: 10.1002/adem.201000320.

- [65] F. Ko, Y. Wan, and Cambridge University Press, “Introduction,” in *Introduction to Nanofiber Materials*, Cambridge United Kingdom: DE GRUYTER SAUR, 2014, pp. 1–12.
- [66] National Nanotechnology Initiative (NNI), “What’s So Special about the Nanoscale?” [Online]. Available: <https://www.nano.gov/nanotech-101/special>. [Accessed: 29-Mar-2020].
- [67] “Fact Sheet: Nanoscale Materials | Reviewing New Chemicals under the Toxic Substances Control Act (TSCA),” *United States Environmental Protection Agency*, 2017. [Online]. Available: <https://www.epa.gov/reviewing-new-chemicals-under-toxic-substances-control-act-tsca/fact-sheet-nanoscale-materials>. [Accessed: 10-May-2021].
- [68] “Control of Nanoscale Materials under the Toxic Substances Control Act | Reviewing New Chemicals under the Toxic Substances Control Act (TSCA),” *United States Environmental Protection Agency*, 2021. [Online]. Available: <https://www.epa.gov/reviewing-new-chemicals-under-toxic-substances-control-act-tsca/control-nanoscale-materials-under>. [Accessed: 10-May-2021].
- [69] “Lighter, Cheaper, Safer, Stronger: Nanotechnology-Enabled Materials,” *National Nanotechnology Initiative*. [Online]. Available: <https://www.nano.gov/node/1545>. [Accessed: 10-May-2021].
- [70] K. Wei, H.-R. Kim, B.-S. Kim, and I.-S. Kim, “Electrospun Metallic Nanofibers Fabricated by Electrospinning and Metallization,” in *Nanofibers - Production, Properties and Functional Applications*, InTech, 2011, pp. 117–134.
- [71] H. Ji, R. Zhao, N. Zhang, C. Jin, X. Lu, and C. Wang, “Lightweight and flexible electrospun polymer nanofiber/metal nanoparticle hybrid membrane for high-performance

- electromagnetic interference shielding,” *NPG Asia Mater.*, vol. 10, pp. 749–760, Aug. 2018, doi: 10.1038/s41427-018-0070-1.
- [72] G. Yip, “COPPER (II) HYDROXIDE NANORODS GROWN ON COPPER AND NICKEL PLATED NANOFIBRES FOR PSEUDOCAPACITOR ELECTRODES IN REGENERATIVE BRAKING,” University of British Columbia, 2017.
- [73] D.-N. Phan *et al.*, “The synthesis of silver-nanoparticle-anchored electrospun polyacrylonitrile nanofibers and a comparison with as-spun silver/polyacrylonitrile nanocomposite membranes upon antibacterial activity,” *Polym. Bull.*, vol. 77, pp. 4197–4212, Aug. 2020, doi: 10.1007/s00289-019-02969-8.
- [74] M.-W. Kim *et al.*, “Packing of metalized polymer nanofibers for aneurysm embolization,” *Nanoscale*, vol. 10, pp. 6589–6601, 2018, doi: 10.1039/C7NR09645C.
- [75] S. An *et al.*, “Self-Junctioned Copper Nanofiber Transparent Flexible Conducting Film via Electrospinning and Electroplating,” *Adv. Mater.*, vol. 28, pp. 7149–7154, Sep. 2016, doi: 10.1002/adma.201506364.
- [76] J. Choi, S. Chan, G. Yip, H. Joo, H. Yang, and F. K. Ko, “Palladium-Zeolite nanofiber as an effective recyclable catalyst membrane for water treatment,” *Water Reseach*, vol. 101, pp. 46–54, 2016, doi: 10.1016/j.watres.2016.05.051.
- [77] D. Gao *et al.*, “Preparation and Characterization of porous Carbon/Nickel Nanofibers for Supercapacitor,” *J. Eng. Fiber. Fabr.*, vol. 8, no. 4, pp. 108–113, 2013, doi: hPreparation and Characterization of porous Carbon/Nickel Nanofibers for Supercapacitor.
- [78] J. Li, E. Liu, W. Li, X. Meng, and S. Tan, “Nickel/carbon nanofibers composite electrodes as supercapacitors prepared by electrospinning,” *J. Alloys Compd.*, vol. 478, no. 1–2, pp. 371–374, Jun. 2009, doi: 10.1016/j.jallcom.2008.11.024.

- [79] Noble Biomaterials, “Electrostatic Discharge (ESD) Solutions.” [Online]. Available: <https://noblebiomaterials.com/x-static/>. [Accessed: 16-Apr-2021].
- [80] Innovation in Textiles, “Flexsil brand for permanent silver based anti-bacterial protection.” [Online]. Available: <https://www.innovationintextiles.com/flexsil-brand-for-permanent-silver-based-antibacterial-protection/>. [Accessed: 17-Apr-2021].
- [81] N. Biomaterials, “Ionic+™.” [Online]. Available: <https://noblebiomaterials.com/ionic-plus/>. [Accessed: 16-Apr-2021].
- [82] Carlisle Interconnect Technologies, “Braided EMI Shields.” [Online]. Available: <https://www.carlisleit.com/products/aracon-fiber/braided-emi-shields/>. [Accessed: 16-Apr-2021].
- [83] F. Ko, Y. Wan, and Cambridge University Press, “Nanofiber Technology,” in *Introduction to Nanofiber Materials*, Cambridge United Kingdom: Cambridge University Press, 2014, pp. 44–63.
- [84] L. Wei, R. Sun, C. Liu, J. Xiong, and X. Qin, “Mass production of nanofibers from needleless electrospinning by a novel annular spinneret,” *Mater. Des.*, vol. 179, p. 107885, Oct. 2019, doi: 10.1016/j.matdes.2019.107885.
- [85] Y. Xu *et al.*, “Large-Scale Preparation of Polymer Nanofibers for Air Filtration by a New Multineedle Electrospinning Device,” *J. Nanomater.*, vol. 2020, pp. 1–7, Apr. 2020, doi: 10.1155/2020/4965438.
- [86] N. Bhardwaj and S. C. Kundu, “Electrospinning: A fascinating fiber fabrication technique,” *Biotechnol. Adv.*, vol. 28, pp. 325–347, May 2010, doi: 10.1016/j.biotechadv.2010.01.004.
- [87] L.-T. Lin, “STRUCTURE AND PROPERTIES OF LIGNIN-BASED COMPOSITE

- CARBON NANOFIBRES,” The University of British Columbia, 2017.
- [88] S. Ramakrishna, K. Fujihara, W.-E. Teo, T. Yong, Z. Ma, and R. Ramaseshan, “Electrospun nanofibers: solving global issues,” *Mater. Today*, vol. 9, no. 3, pp. 40–50, Mar. 2006, doi: 10.1016/S1369-7021(06)71389-X.
- [89] G. C. Rutledge and S. V. Fridrikh, “Formation of fibers by electrospinning,” *Adv. Drug Deliv. Rev.*, vol. 59, pp. 1384–1391, Dec. 2007, doi: 10.1016/j.addr.2007.04.020.
- [90] D. H. Reneker and A. L. Yarin, “Electrospinning jets and polymer nanofibers,” *Polymer (Guildf.)*, vol. 49, pp. 2387–2425, May 2008, doi: 10.1016/j.polymer.2008.02.002.
- [91] F. K. Ko and L. Y. Wan, “Nanofiber Technology Bridging the Gap between Nano and Macro World,” in *Nanomaterials Handbook*, 2nd ed., Y. Gogotsi, Ed. Boca Raton, FL: CRC Press, 2017, pp. 603–629.
- [92] M. Bayat, H. Yang, F. K. Ko, D. Michelson, and A. Mei, “Electromagnetic interference shielding effectiveness of hybrid multifunctional Fe₃O₄/carbon nanofiber composite,” *Polymer (Guildf.)*, vol. 55, pp. 936–943, Feb. 2014, doi: 10.1016/j.polymer.2013.12.042.
- [93] E. J. Ra, K. H. An, K. K. Kim, S. Y. Jeong, and Y. H. Lee, “Anisotropic electrical conductivity of MWCNT/PAN nanofiber paper,” *Chem. Phys. Lett.*, vol. 413, pp. 188–193, Sep. 2005, doi: 10.1016/j.cplett.2005.07.061.
- [94] S. Kedem, J. Schmidt, Y. Paz, and Y. Cohen, “Composite Polymer Nanofibers with Carbon Nanotubes and Titanium Dioxide Particles,” *Langmuir*, vol. 21, pp. 5600–5604, Jun. 2005, doi: 10.1021/la0502443.
- [95] C. Prahsarn, W. Klinsukhon, and N. Roungpaisan, “Electrospinning of PAN/DMF/H₂O containing TiO₂ and photocatalytic activity of their webs,” *Mater. Lett.*, vol. 65, pp. 2498–2501, Aug. 2011, doi: 10.1016/j.matlet.2011.05.018.

- [96] M. S. Enayati *et al.*, “Development of electrospun poly (vinyl alcohol)-based bionanocomposite scaffolds for bone tissue engineering,” *J. Biomed. Mater. Res. Part A*, vol. 106, pp. 1111–1120, Apr. 2018, doi: 10.1002/jbm.a.36309.
- [97] S.-X. Wang, L. Yang, L. P. Stubbs, X. Li, and C. He, “Lignin-Derived Fused Electrospun Carbon Fibrous Mats as High Performance Anode Materials for Lithium Ion Batteries,” *ACS Appl. Mater. Interfaces*, vol. 5, pp. 12275–12282, Dec. 2013, doi: 10.1021/am4043867.
- [98] E. Svinterikos, I. Zuburtikudis, and M. Al-Marzouqi, “Electrospun Lignin-Derived Carbon Micro- and Nanofibers: A Review on Precursors, Properties, and Applications,” *ACS Sustain. Chem. Eng.*, vol. 8, pp. 13868–13893, Sep. 2020, doi: 10.1021/acssuschemeng.0c03246.
- [99] E. Frank, L. M. Steudle, D. Ingildeev, J. M. Spörl, and M. R. Buchmeiser, “Carbon Fibers: Precursor Systems, Processing, Structure, and Properties,” *Angew. Chemie Int. Ed.*, vol. 53, pp. 5262–5298, May 2014, doi: 10.1002/anie.201306129.
- [100] M. Fodil Cherif, D. Trache, N. Brosse, F. Benaliouche, and A. F. Tarchoun, “Comparison of the Physicochemical Properties and Thermal Stability of Organosolv and Kraft Lignins from Hardwood and Softwood Biomass for Their Potential Valorization,” *Waste and Biomass Valorization*, vol. 11, pp. 6541–6553, Dec. 2020, doi: 10.1007/s12649-020-00955-0.
- [101] Y. Li, “STRUCTURES, PROPERTIES AND APPLICATIONS OF MULTIFUNCTIONAL LIGNIN NANOFIBRES,” The University of British Columbia, 2015.
- [102] T. Q. Hu, *Chemical Modification, Properties, and Usage of Lignin*. Boston, MA: Springer

- US, 2002.
- [103] C. Nitsos *et al.*, “Isolation and Characterization of Organosolv and Alkaline Lignins from Hardwood and Softwood Biomass,” *ACS Sustain. Chem. Eng.*, vol. 4, pp. 5181–5193, Oct. 2016, doi: 10.1021/acssuschemeng.6b01205.
- [104] D. Kai, M. J. Tan, P. L. Chee, Y. K. Chua, Y. L. Yap, and X. J. Loh, “Towards lignin-based functional materials in a sustainable world,” *Green Chem.*, vol. 18, no. 5, pp. 1175–1200, Feb. 2016, doi: 10.1039/C5GC02616D.
- [105] S. Ma *et al.*, “Variations and determinants of carbon content in plants: a global synthesis,” *Biogeosciences*, vol. 15, pp. 693–702, Feb. 2018, doi: 10.5194/bg-15-693-2018.
- [106] A. Prakash, R. Singh, B. Balagurumurthy, T. Bhaskar, A. K. Arora, and S. K. Puri, “Thermochemical Valorization of Lignin,” in *Recent Advances in Thermo-Chemical Conversion of Biomass*, Elsevier, 2015, pp. 455–478.
- [107] A. Duval and M. Lawoko, “A review on lignin-based polymeric, micro- and nano-structured materials,” *React. Funct. Polym.*, vol. 85, pp. 78–96, Dec. 2014, doi: 10.1016/j.reactfunctpolym.2014.09.017.
- [108] A. Awal and M. Sain, “Characterization of Soda Hardwood Lignin and the Formation of Lignin Fibers by Melt Spinning,” *J. Appl. Polym. Sci.*, vol. 129, pp. 2765–2771, Sep. 2013, doi: 10.1002/app.38911.
- [109] J. . Kadla, S. Kubo, R. . Venditti, R. . Gilbert, A. . Compere, and W. Griffith, “Lignin-based carbon fibers for composite fiber applications,” *Carbon N. Y.*, vol. 40, pp. 2913–2920, 2002, doi: 10.1016/S0008-6223(02)00248-8.
- [110] J. Köhnke *et al.*, “Comparison of Four Technical Lignins as a Resource for Electrically Conductive Carbon Particles,” *BioResources*, vol. 14, no. 1, pp. 1091–1109, Dec. 2018,

doi: 10.15376/biores.14.1.1091-1109.

- [111] T. D. M. Florian *et al.*, “Chemical composition analysis and structural features of banana rachis lignin extracted by two organosolv methods,” *Ind. Crops Prod.*, vol. 132, pp. 269–274, Jun. 2019, doi: 10.1016/j.indcrop.2019.02.022.
- [112] P. Bajpai, *Pulping Chemistry and Technology*. Walter de Gruyter, 2010.
- [113] D. A. Baker, N. C. Gallego, and F. S. Baker, “On the Characterization and Spinning of an Organic- Purified Lignin Toward the Manufacture of Low-Cost Carbon Fiber,” *J. Appl. Polym. Sci.*, vol. 124, pp. 227–234, Apr. 2012, doi: 10.1002/app.33596.
- [114] A. Attwenger, “VALUE-ADDED LIGNIN BASED CARBON FIBER FROM VALUE-ADDED LIGNIN BASED CARBON FIBER FROM ORGANOSOLV FRACTIONATION OF POPLAR AND SWITCHGRASS ORGANOSOLV FRACTIONATION OF POPLAR AND SWITCHGRASS,” University of Tennessee, 2014.
- [115] I. Dallmeyer, F. Ko, and J. F. Kadla, “Correlation of Elongational Fluid Properties to Fiber Diameter in Electrospinning of Softwood Kraft Lignin Solutions,” *Ind. Eng. Chem. Res.*, vol. 53, pp. 2697–2705, Feb. 2014, doi: 10.1021/ie403724y.
- [116] C. Deckert and I. Shipley Company, “Electroless Copper Plating,” in *ASM Handbook, Volume 05 - Surface Engineering*, vol. 5, ASM International, 1994, pp. 311–322.
- [117] M. Schlesinger and M. Paunovic, *Modern Electroplating*, 5th ed. Hoboken, NJ, USA: John Wiley & Sons, Inc., 2010.
- [118] G. A. Krulik, “Electroless plating of plastics,” *J. Chem. Educ.*, vol. 55, no. 6, p. 361, Jun. 1978, doi: 10.1021/ed055p361.
- [119] A. Yli-Pentti, “Electroplating and Electroless Plating,” in *Comprehensive Materials*

- Processing*, Elsevier, 2014, pp. 277–306.
- [120] J. E. A. M. Van Den Meerakker, “On the mechanism of electroless plating. II. One mechanism for different reductants,” *J. Appl. Electrochem.*, vol. 11, pp. 395–400, May 1981, doi: 10.1007/BF00613960.
- [121] A. M. Helmenstine, “Conductivity and Conductive Elements,” 2019. [Online]. Available: <https://www.thoughtco.com/the-most-conductive-element-606683>. [Accessed: 20-Jan-2021].
- [122] A. Helmenstine, “What Is the Most Conductive Element?,” 2020. [Online]. Available: <https://sciencenotes.org/what-is-the-most-conductive-element/>. [Accessed: 20-Jan-2021].
- [123] “Metal Commodities.” [Online]. Available: <https://www.cnbc.com/metal-commodities/>. [Accessed: 20-Jan-2021].
- [124] E. Steinhäuser, “Potential low-cost palladium-alternatives for activating electroless copper deposition,” *Circuit World*, vol. 36, no. 3, pp. 4–8, Aug. 2010, doi: 10.1108/03056121011066279.
- [125] P. Bindra and J. R. White, “Fundamental Aspects of Electroless Copper Plating,” in *Electroless Plating*, 2008, pp. 289–329.
- [126] B. D. Barker, “Electroless Deposition of Metals,” *Surf. Technol.*, vol. 12, pp. 77–88, 1981.
- [127] D. A. Luke and L. Ronal, “New Non-Precious Metal Catalyst for Through-Hole Plating,” *Circuit World*, vol. 7, no. 4, pp. 36–40, 1981.
- [128] J. J. Kuzmik, “Plating on Plastics,” in *Electroless Plating - Fundamentals and Applications*, 1990, pp. 377–399.
- [129] I. Dallmeyer, F. Ko, and J. F. Kadla, “Electrospinning of Technical Lignins for the Production of Fibrous Networks,” *J. Wood Chem. Technol.*, vol. 30, pp. 315–329, Nov.

- 2010, doi: 10.1080/02773813.2010.527782.
- [130] J. I. Dallmeyer, “PREPARATION AND CHARACTERIZATION OF LIGNIN NANOFIBRE-BASED MATERIALS OBTAINED BY ELECTROSTATIC SPINNING,” University of British Columbia, 2013.
- [131] X. Shi, X. Wang, B. Tang, Z. Dai, K. Chen, and J. Zhou, “Impact of lignin extraction methods on microstructure and mechanical properties of lignin-based carbon fibers,” *J. Appl. Polym. Sci.*, vol. 135, p. 45580, Mar. 2018, doi: 10.1002/app.45580.
- [132] S. Aslanzadeh, B. Ahvazi, Y. Boluk, and C. Ayranci, “Carbon Fiber Production from Electrospun Sulfur Free Softwood Lignin Precursors,” *J. Eng. Fiber. Fabr.*, vol. 12, no. 4, p. 155892501701200, Dec. 2017, doi: 10.1177/155892501701200405.
- [133] T. Watson, “Engineering High Performance Electrodes for Energy Storage Devices from Low-cost, Sustainable and Naturally Abundant Biomaterials,” University of British Columbia, 2016.
- [134] S. Vargheese, D. Muthu, D. Pattappan, K. V. Kavya, R. T. R. Kumar, and Y. Haldorai, “Hierarchical flower-like MnO₂@nitrogen-doped porous carbon composite for symmetric supercapacitor: Constructing a 9.0 V symmetric supercapacitor cell,” *Electrochim. Acta*, vol. 364, p. 137291, Dec. 2020, doi: 10.1016/j.electacta.2020.137291.
- [135] M. Chamoun, W. R. Brant, C.-W. Tai, G. Karlsson, and D. Noréus, “Rechargeability of aqueous sulfate Zn/MnO₂ batteries enhanced by accessible Mn²⁺ ions,” *Energy Storage Mater.*, vol. 15, pp. 351–360, Nov. 2018, doi: 10.1016/j.ensm.2018.06.019.
- [136] F. K. Ko, Y. Wan, and Cambridge University Press, “Characterization of nanofibers,” in *Introduction to Nanofiber Materials*, Cambridge United Kingdom: Cambridge University Press, 2014, pp. 101–145.

- [137] S. Nasrazadani and S. Hassani, "Modern analytical techniques in failure analysis of aerospace, chemical, and oil and gas industries," in *Handbook of Materials Failure Analysis with Case Studies from the Oil and Gas Industry*, Elsevier, 2016, pp. 39–54.
- [138] P. M. V. Raja and A. R. Barron, "An Introduction to Energy Dispersive X-ray Spectroscopy," *Chemistry LibreTexts*. [Online]. Available: [https://chem.libretexts.org/Bookshelves/Analytical_Chemistry/Book%3A_Physical_Methods_in_Chemistry_and_Nano_Science_\(Barron\)/01%3A_Elemental_Analysis/1.12%3A_An_Introduction_to_Energy_Dispersive_X-ray_Spectroscopy](https://chem.libretexts.org/Bookshelves/Analytical_Chemistry/Book%3A_Physical_Methods_in_Chemistry_and_Nano_Science_(Barron)/01%3A_Elemental_Analysis/1.12%3A_An_Introduction_to_Energy_Dispersive_X-ray_Spectroscopy). [Accessed: 25-Jun-2021].
- [139] K. A. CONNORS, "THE PHENOMENOLOGICAL THEORY OF SOLVENT EFFECTS IN MIXED SOLVENT SYSTEMS," in *Handbook of Solvents*, Elsevier, 2014, pp. 467–490.
- [140] P. M. V. Raja and A. R. Barron, "X-ray Photoelectron Spectroscopy," *Chemistry LibreTexts*. [Online]. Available: [https://chem.libretexts.org/Bookshelves/Analytical_Chemistry/Book%3A_Physical_Methods_in_Chemistry_and_Nano_Science_\(Barron\)/01%3A_Elemental_Analysis/1.13%3A_X-ray_Photoelectron_Spectroscopy](https://chem.libretexts.org/Bookshelves/Analytical_Chemistry/Book%3A_Physical_Methods_in_Chemistry_and_Nano_Science_(Barron)/01%3A_Elemental_Analysis/1.13%3A_X-ray_Photoelectron_Spectroscopy). [Accessed: 26-Jun-2021].
- [141] F. M. SMITS, "Measurement of Sheet Resistivities with the Four-Point Probe," in *The Bell System Technical Journal*, WORLD SCIENTIFIC, 1958, pp. 711–718.
- [142] Y. Wang, F. Gan, and K. Chen, "Graphene composite plastic film as current collector for aluminum-graphite batteries," *Mater. Lett.*, vol. 254, pp. 436–439, Nov. 2019, doi: 10.1016/j.matlet.2019.06.082.
- [143] S.-H. Deng, Y. Wang, and X. Yang, "The study of electrochemical synthesis, properties and composite mechanism of PANI/PVA and PANI/PVA/Ag composite films," *Pigment*

- Resin Technol.*, vol. 47, no. 2, pp. 133–141, Mar. 2018, doi: 10.1108/PRT-11-2016-0101.
- [144] W. Zhou *et al.*, “Hybridizing δ -Type MnO₂ With Lignin-Derived Porous Carbon as a Stable Cathode Material for Aqueous Zn–MnO₂ Batteries,” *Front. Energy Res.*, vol. 8, no. 182, pp. 1–9, Jul. 2020, doi: 10.3389/fenrg.2020.00182.
- [145] N. Elgrishi, K. J. Rountree, B. D. McCarthy, E. S. Rountree, T. T. Eisenhart, and J. L. Dempsey, “A Practical Beginner’s Guide to Cyclic Voltammetry,” *J. Chem. Educ.*, vol. 95, pp. 197–206, Feb. 2018, doi: 10.1021/acs.jchemed.7b00361.
- [146] Y. Chen, J. Li, S. Zhang, J. Cui, and M. Shao, “Highly Reversible Zinc Anode Enhanced by Ultrathin MnO₂ Cathode Material Film for High-Performance Zinc-Ion Batteries,” *Adv. Mater. Interfaces*, vol. 7, p. 2000510, Aug. 2020, doi: 10.1002/admi.202000510.
- [147] D. Y. Putro *et al.*, “Quasi-solid-state zinc-ion battery based on α -MnO₂ cathode with husk-like morphology,” *Electrochim. Acta*, vol. 345, p. 136189, Jun. 2020, doi: 10.1016/j.electacta.2020.136189.
- [148] M. Han *et al.*, “Oxygen Defects in β -MnO₂ Enabling High-Performance Rechargeable Aqueous Zinc/Manganese Dioxide Battery,” *iScience*, vol. 23, p. 100797, Jan. 2020, doi: 10.1016/j.isci.2019.100797.
- [149] W. Liu *et al.*, “ β -MnO₂ with proton conversion mechanism in rechargeable zinc ion battery,” *J. Energy Chem.*, vol. 56, pp. 365–373, May 2021, doi: 10.1016/j.jechem.2020.07.027.
- [150] L. Li, T. K. A. Hoang, J. Zhi, M. Han, S. Li, and P. Chen, “Functioning Mechanism of the Secondary Aqueous Zn- β -MnO₂ Battery,” *ACS Appl. Mater. Interfaces*, vol. 12, pp. 12834–12846, Mar. 2020, doi: 10.1021/acsami.9b22758.
- [151] L. A. Middlemiss, A. J. R. Rennie, R. Sayers, and A. R. West, “Characterisation of

- batteries by electrochemical impedance spectroscopy,” *Energy Reports*, vol. 6, pp. 232–241, May 2020, doi: 10.1016/j.egy.2020.03.029.
- [152] P. Tan Thong, T. Sadhasivam, N.-I. Kim, Y. A. Kim, S.-H. Roh, and H.-Y. Jung, “Highly conductive current collector for enhancing conductivity and power supply of flexible thin-film Zn–MnO₂ battery,” *Energy*, vol. 221, p. 119856, Apr. 2021, doi: 10.1016/j.energy.2021.119856.
- [153] A. L. Yarin, B. Pourdeyhimi, and S. Ramakrishna, “General quasi-one-dimensional equations of dynamics of free liquid jets, capillary and bending instability,” in *Fundamentals and Applications of Micro and Nanofibers*, Cambridge: Cambridge University Press, 2014, pp. 63–88.
- [154] S. Aslanzadeh, B. Ahvazi, Y. Boluk, and C. Ayranci, “Morphologies of electrospun fibers of lignin in poly(ethylene oxide)/N,N-dimethylformamide,” *J. Appl. Polym. Sci.*, vol. 133, p. 44172, Nov. 2016, doi: 10.1002/app.44172.
- [155] H. Fong, I. Chun, and D. . Reneker, “Beaded nanofibers formed during electrospinning,” *Polymer (Guildf)*., vol. 40, pp. 4585–4592, Jul. 1999, doi: 10.1016/S0032-3861(99)00068-3.
- [156] V. Poursorkhabi, A. K. Mohanty, and M. Misra, “Electrospinning of Aqueous Lignin/Poly(ethylene oxide) Complexes,” *J. Appl. Polym. Sci.*, vol. 132, p. 41260, Jan. 2015, doi: 10.1002/app.41260.
- [157] M. G. McKee, G. L. Wilkes, R. H. Colby, and T. E. Long, “Correlations of Solution Rheology with Electrospun Fiber Formation of Linear and Branched Polyesters,” *Macromolecules*, vol. 37, no. 5, pp. 1760–1767, Mar. 2004, doi: 10.1021/ma035689h.
- [158] M. Cho, F. K. Ko, and S. Rennecker, “Impact of Thermal Oxidative Stabilization on the

- Performance of Lignin-Based Carbon Nanofiber Mats,” *ACS Omega*, vol. 4, no. 3, pp. 5345–5355, Mar. 2019, doi: 10.1021/acsomega.9b00278.
- [159] L. E. Nielsen, “Cross-Linking-Effect on Physical Properties of Polymers,” *J. Macromol. Sci. Part C*, vol. 3, no. 1, pp. 69–103, 1969, doi: 10.1080/15583726908545897.
- [160] S. Jaswal, T. Thakur, B. Gaur, and A. S. Singha, “High-performance gum rosin-modified hyperbranched vinyl ester resin derived from multifunctional pentaerythritol,” *Polym. Bull.*, pp. 1–25, Jan. 2021, doi: 10.1007/s00289-020-03511-x.
- [161] Y.-H. Xie *et al.*, “Mechanistic aspects of formation of sintering-resistant palladium nanoparticles over SiO₂ prepared using Pd(acac)₂ as precursor,” *Appl. Catal. A Gen.*, vol. 504, pp. 179–186, Sep. 2015, doi: 10.1016/j.apcata.2014.12.008.
- [162] F. W. Zeng, D. Zhang, and J. B. Spicer, “Palladium nanoparticle formation processes in fluoropolymers by thermal decomposition of organometallic precursors,” *Phys. Chem. Chem. Phys.*, vol. 20, pp. 24389–24398, Sep. 2018, doi: 10.1039/C8CP04997A.
- [163] Sigma Aldrich, “MSDS - Pd(acac)₂.” [Online]. Available: <https://www.sigmaaldrich.com/MSDS/MSDS/DisplayMSDSPage.do?country=CA&language=en&productNumber=209015&brand=ALDRICH&PageToGoToURL=https%3A%2F%2Fwww.sigmaaldrich.com%2Fcatalog%2Fproduct%2Faldrich%2F209015%3Flang%3Den>. [Accessed: 24-May-2021].
- [164] M. C. Bavya, L. George, R. Srivastava, and V. Rohan K, “Natural and Synthetic Materials in Regenerative Medicine: Progress Over the Past Five Years,” in *Reference Module in Materials Science and Materials Engineering*, Elsevier, 2019.
- [165] PerkinElmer, “Thermogravimetric Analysis (TGA) A Beginner’s Guide.”
- [166] PerkinElmer and Inc, “Characterization of Polymers using TGA.”

- [167] “Energy table for EDS analysis,” *JEOL*. .
- [168] Lawrence Berkeley National Laboratory, “X-Ray Data Booklet.”
- [169] I. Norberg, Y. Nordström, R. Drougge, G. Gellerstedt, and E. Sjöholm, “A New Method for Stabilizing Softwood Kraft Lignin Fibers for Carbon Fiber Production,” *J. Appl. Polym. Sci.*, vol. 128, pp. 3824–3830, Jun. 2013, doi: 10.1002/app.38588.
- [170] J. Köhnke *et al.*, “Carbon Microparticles from Organosolv Lignin as Filler for Conducting Poly(Lactic Acid),” *Polymers (Basel)*, vol. 8, p. 205, May 2016, doi: 10.3390/polym8060205.
- [171] J. Dörrstein *et al.*, “Dataset on the structural characterization of organosolv lignin obtained from ensiled Poaceae grass and load-dependent molecular weight changes during thermoplastic processing,” *Data Br.*, vol. 17, pp. 647–652, Apr. 2018, doi: 10.1016/j.dib.2018.01.060.
- [172] K. F. El-Nemr, H. R. Mohamed, M. A. Ali, R. M. Fathy, and A. S. Dhmees, “Polyvinyl alcohol/gelatin irradiated blends filled by lignin as green filler for antimicrobial packaging materials,” *Int. J. Environ. Anal. Chem.*, vol. 100, pp. 1578–1602, Nov. 2020, doi: 10.1080/03067319.2019.1657108.
- [173] G. Li *et al.*, “Pd catalyst supported on ZrO₂-Al₂O₃ by double-solvent method for methane oxidation under lean conditions,” *Can. J. Chem. Eng.*, vol. 95, pp. 1117–1123, Jun. 2017, doi: 10.1002/cjce.22750.
- [174] R. Niu, P. Liu, W. Li, S. Wang, and J. Li, “High performance for oxidation of low-concentration methane using ultra-low Pd in silicalite-1 zeolite,” *Microporous Mesoporous Mater.*, vol. 284, pp. 235–240, Aug. 2019, doi: 10.1016/j.micromeso.2019.04.044.

- [175] E. Ochoa *et al.*, “Synthesis and characterization of a supported Pd complex on carbon nanofibers for the selective decarbonylation of stearic acid to 1-heptadecene: the importance of subnanometric Pd dispersion,” *Catal. Sci. Technol.*, vol. 10, pp. 2970–2985, May 2020, doi: 10.1039/D0CY00322K.
- [176] W. Sha, X. Wu, and K. G. Keong, “Electrical resistivity of electroless copper deposit,” in *Electroless Copper and Nickel–Phosphorus Plating*, Elsevier, 2011, pp. 117–134.
- [177] J. Dumesic, J. A. Koutsky, and T. W. Chapman, “The Rate of Electroless Copper Deposition by Formaldehyde Reduction,” *J. Electrochem. Soc.*, vol. 121, no. 11, p. 1405, 1974, doi: 10.1149/1.2401698.
- [178] H. Wang, J. Jia, H. Song, X. Hu, H. Sun, and D. Yang, “The preparation of Cu-coated Al₂O₃ composite powders by electroless plating,” *Ceram. Int.*, vol. 37, pp. 2181–2184, Sep. 2011, doi: 10.1016/j.ceramint.2011.03.013.
- [179] J. M. Córdoba and M. Odén, “Growth and characterization of electroless deposited Cu films on carbon nanofibers,” *Surf. Coatings Technol.*, vol. 203, pp. 3459–3464, Aug. 2009, doi: 10.1016/j.surfcoat.2009.05.007.
- [180] X. Zhang, J. Wang, J. Tang, and Z. Tian, “Unraveling the multilayer structure formation mechanism of copper coating for the metallization of poly para-phenylene terephthalamide fibers,” *Colloids Surfaces A Physicochem. Eng. Asp.*, vol. 618, p. 126450, Jun. 2021, doi: 10.1016/j.colsurfa.2021.126450.
- [181] J. Huang *et al.*, “Fabrication of selective electroless copper plating on PET sheet: Effect of PET surface structure on resolution and adhesion of copper coating,” *Appl. Surf. Sci.*, vol. 458, pp. 734–742, Nov. 2018, doi: 10.1016/j.apsusc.2018.07.119.
- [182] G. H. Kim, J. H. Shin, T. An, and G. Lim, “Junction-free Flat Copper Nanofiber Network-

- based Transparent Heater with High Transparency, High Conductivity, and High Temperature,” *Sci. Rep.*, vol. 8, p. 13581, Dec. 2018, doi: 10.1038/s41598-018-32045-6.
- [183] H. Ji *et al.*, “Robust and durable superhydrophobic electrospun nanofibrous mats via a simple Cu nanocluster immobilization for oil-water contamination,” *Colloids Surfaces A*, vol. 538, pp. 173–183, Feb. 2018, doi: 10.1016/j.colsurfa.2017.10.064.
- [184] The Editors of Encyclopaedia Britannica, “Resistivity,” *Britannica*. [Online]. Available: <https://www.britannica.com/science/resistivity>. [Accessed: 06-Jun-2021].
- [185] N. Seidle, “How to Use a Multimeter,” *SparkFun Electronics*. [Online]. Available: <https://learn.sparkfun.com/tutorials/how-to-use-a-multimeter/continuity>. [Accessed: 06-Jun-2021].
- [186] MyScope, “DEPRECATED - Qualitative EDS X-ray microanalysis: What elements are present in the sample?,” 2013. [Online]. Available: <https://myscope.training/legacy/analysis/background/qualitative/>. [Accessed: 30-Apr-2021].
- [187] M. Raja, J. Subha, F. B. Ali, and S. H. Ryu, “Synthesis of Copper Nanoparticles by Electroreduction Process,” *Mater. Manuf. Process.*, vol. 23, pp. 782–785, Oct. 2008, doi: 10.1080/10426910802382080.
- [188] A. K. Kar and R. Srivastava, “Selective synthesis of Cu–Cu₂O/C and CuO–Cu₂O/C catalysts for Pd-free C–C, C–N coupling and oxidation reactions,” *Inorg. Chem. Front.*, vol. 6, pp. 576–589, 2019, doi: 10.1039/C8QI01198B.
- [189] S. J. Kerber, T. L. Barr, G. P. Mann, W. A. Brantley, E. Papazoglou, and J. C. Mitchell, “The Complementary Nature of X-Ray Photoelectron Spectroscopy and Angle-Resolved X-Ray Diffraction Part I: Background and Theory,” *J. Mater. Eng. Perform.*, vol. 7, no. 3,

- pp. 329–333, Jun. 1998, doi: 10.1361/105994998770347765.
- [190] C. Zhou *et al.*, “Matchstick-Like Cu₂S@Cu_xO Nanowire Film: Transition of Superhydrophilicity to Superhydrophobicity,” *J. Phys. Chem. C*, vol. 121, pp. 19716–19726, Sep. 2017, doi: 10.1021/acs.jpcc.7b03645.
- [191] K. N. Porchelvi, S. Meenakshi, and K. Pandian, “*In Situ* Synthesis of Copper Phthalocyanine Modified Multiwalled Carbon Tube and its Electrocatalytic Application towards the Oxidation of Nitrite,” *Adv. Mater. Res.*, vol. 938, pp. 40–45, Jun. 2014, doi: 10.4028/www.scientific.net/AMR.938.40.
- [192] Y. Wang, Y. Lü, W. Zhan, Z. Xie, Q. Kuang, and L. Zheng, “Synthesis of porous Cu₂O/CuO cages using Cu-based metal–organic frameworks as templates and their gas-sensing properties,” *J. Mater. Chem. A*, vol. 3, pp. 12796–12803, 2015, doi: 10.1039/C5TA01108F.
- [193] J. F. Moulder, W. F. Stickle, P. E. Sobol, K. D. Bomben, and J. Chastain, “Handbook of X-ray Photoelectron Spectroscopy A Reference Book of Standard Spectra for Identification and Interpretation of XPS Data.”
- [194] B. T. Sone, A. Diallo, X. G. Fuku, A. Gurib-Fakim, and M. Maaza, “Biosynthesized CuO nano-platelets: Physical properties & enhanced thermal conductivity nanofluidics,” *Arab. J. Chem.*, vol. 13, pp. 160–170, Jan. 2020, doi: 10.1016/j.arabjc.2017.03.004.
- [195] Q. Chen *et al.*, “Zn²⁺ Pre-Intercalation Stabilizes the Tunnel Structure of MnO₂ Nanowires and Enables Zinc-Ion Hybrid Supercapacitor of Battery-Level Energy Density,” *Small*, vol. 16, p. 2000091, Apr. 2020, doi: 10.1002/sml.202000091.
- [196] D. Yuan *et al.*, “Lignin@Nafion Membranes Forming Zn Solid–Electrolyte Interfaces Enhance the Cycle Life for Rechargeable Zinc-Ion Batteries,” *ChemSusChem*, vol. 12, pp.

- 4889–4900, Nov. 2019, doi: 10.1002/cssc.201901409.
- [197] Z. H. Raheem and A. M. A. Al Sammarraie, “Synthesis of different manganese dioxide nanostructures and studying the enhancement of their electrochemical behavior in zinc – MnO₂ rechargeable batteries by doping with copper,” in *AIP Conference Proceedings*, 2020, vol. 2213, p. 020187, doi: 10.1063/5.0000246.
- [198] X. Huang, D. Lv, H. Yue, A. Attia, and Y. Yang, “Controllable synthesis of α - and β - MnO₂ : cationic effect on hydrothermal crystallization,” *Nanotechnology*, vol. 19, no. 22, p. 225606, Jun. 2008, doi: 10.1088/0957-4484/19/22/225606.
- [199] K.-S. Yun, B.-R. Kim, W.-S. Kang, S.-C. Jung, S.-T. Myung, and S.-J. Kim, “Preparation of Carbon Blacks by Liquid Phase Plasma (LPP) Process,” *J. Nanosci. Nanotechnol.*, vol. 13, no. 11, pp. 7381–7385, Nov. 2013, doi: 10.1166/jnn.2013.7861.
- [200] N. R. Ostyn *et al.*, “Low-temperature activation of carbon black by selective photocatalytic oxidation,” *Nanoscale Adv.*, vol. 1, pp. 2873–2880, Aug. 2019, doi: 10.1039/C9NA00188C.
- [201] M. C. Biesinger, B. P. Payne, A. P. Grosvenor, L. W. M. Lau, A. R. Gerson, and R. S. C. Smart, “Resolving surface chemical states in XPS analysis of first row transition metals, oxides and hydroxides: Cr, Mn, Fe, Co and Ni,” *Appl. Surf. Sci.*, vol. 257, pp. 2717–2730, Jan. 2011, doi: 10.1016/j.apsusc.2010.10.051.
- [202] Z. Yang *et al.*, “Vertically-aligned Mn(OH)₂ nanosheet films for flexible all-solid-state electrochemical supercapacitors,” *J. Mater. Sci. Mater. Electron.*, vol. 28, pp. 17533–17540, Dec. 2017, doi: 10.1007/s10854-017-7689-5.
- [203] V. Subramanian, H. Zhu, R. Vajtai, P. M. Ajayan, and B. Wei, “Hydrothermal Synthesis and Pseudocapacitance Properties of MnO₂ Nanostructures,” *J. Phys. Chem. B*, vol. 109,

- no. 43, pp. 20207–20214, Nov. 2005, doi: 10.1021/jp0543330.
- [204] Z. Wang *et al.*, “A flexible rechargeable zinc-ion wire-shaped battery with shape memory function,” *J. Mater. Chem. A*, vol. 6, pp. 8549–8557, 2018, doi: 10.1039/C8TA01172A.
- [205] N. Zhang *et al.*, “Activity enhancement of Pt/MnO_x catalyst by novel β-MnO₂ for low-temperature CO oxidation: study of the CO–O₂ competitive adsorption and active oxygen species,” *Catal. Sci. Technol.*, vol. 9, pp. 347–354, 2019, doi: 10.1039/C8CY01879K.
- [206] D. Jampaiah *et al.*, “Nanowire Morphology of Mono- and Bidoped α-MnO₂ Catalysts for Remarkable Enhancement in Soot Oxidation,” *ACS Appl. Mater. Interfaces*, vol. 9, pp. 32652–32666, Sep. 2017, doi: 10.1021/acsami.7b07656.
- [207] W. Sun, A. Hsu, and R. Chen, “Carbon-supported tetragonal MnOOH catalysts for oxygen reduction reaction in alkaline media,” *J. Power Sources*, vol. 196, pp. 627–635, Jan. 2011, doi: 10.1016/j.jpowsour.2010.07.082.
- [208] H. Fang *et al.*, “Facile fabrication of multiwalled carbon nanotube/α-MnOOH coaxial nanocable films by electrophoretic deposition for supercapacitors,” *J. Power Sources*, vol. 235, pp. 95–104, Aug. 2013, doi: 10.1016/j.jpowsour.2013.01.195.
- [209] R. Nölle, K. Beltrop, F. Holtstiege, J. Kasnatscheew, T. Placke, and M. Winter, “A reality check and tutorial on electrochemical characterization of battery cell materials: How to choose the appropriate cell setup,” *Mater. Today*, vol. 32, pp. 131–146, Jan. 2020, doi: 10.1016/j.mattod.2019.07.002.
- [210] D. Su, H.-J. Ahn, and G. Wang, “β-MnO₂ nanorods with exposed tunnel structures as high-performance cathode materials for sodium-ion batteries,” *NPG Asia Mater.*, vol. 5, no. e70, Nov. 2013, doi: 10.1038/am.2013.56.
- [211] M. Fritsch *et al.*, “Lightweight Polymer-Carbon Composite Current Collector for Lithium-

- Ion Batteries,” *Batteries*, vol. 6, p. 60, Dec. 2020, doi: 10.3390/batteries6040060.
- [212] K. Wang *et al.*, “High-Performance Cable-Type Flexible Rechargeable Zn Battery Based on MnO₂ @CNT Fiber Microelectrode,” *ACS Appl. Mater. Interfaces*, vol. 10, pp. 24573–24582, Jul. 2018, doi: 10.1021/acsami.8b07756.
- [213] J. Huang *et al.*, “Polyaniline-intercalated manganese dioxide nanolayers as a high-performance cathode material for an aqueous zinc-ion battery,” *Nat. Commun.*, vol. 9, p. 2906, Dec. 2018, doi: 10.1038/s41467-018-04949-4.
- [214] M. H. Aboonassr Shiraz, “Electrode and Interface Design for Lithium/Sodium – Selenium Batteries,” The University of British Columbia, 2021.
- [215] N. A. Handayani, E. A. Krisanti, S. Kartohardjono, and K. Mulia, “Cyclic Voltammetry and Oxidation Rate Studies of Ferrous Gluconate Complex Solutions for Preparation of Chitosan-Tripolyphosphate Microparticles,” *J. Chem.*, vol. 2020, pp. 1–8, Feb. 2020, doi: 10.1155/2020/3417204.
- [216] J. Liu *et al.*, “A zinc ion yarn battery with high capacity and fire retardancy based on a SiO₂ nanoparticle doped ionogel electrolyte,” *Soft Matter*, vol. 16, pp. 7432–7437, 2020, doi: 10.1039/D0SM00996B.
- [217] M. Dubarry, V. Svoboda, R. Hwu, and B. Yann Liaw, “Incremental Capacity Analysis and Close-to-Equilibrium OCV Measurements to Quantify Capacity Fade in Commercial Rechargeable Lithium Batteries,” *Electrochem. Solid-State Lett.*, vol. 9, no. 10, p. A454, 2006, doi: 10.1149/1.2221767.
- [218] COMSOL, “Lithium-Ion Battery Rate Capability.” [Online]. Available: https://www.comsol.com/model/download/797301/models.battery.li_battery_rate_capability.pdf. [Accessed: 21-Jun-2021].

- [219] H. Pan *et al.*, “Reversible aqueous zinc/manganese oxide energy storage from conversion reactions,” *Nat. Energy*, vol. 1, p. 16039, May 2016, doi: 10.1038/nenergy.2016.39.
- [220] J. L. Garcia, “Electric power systems,” in *Cubesat Handbook*, Elsevier, 2021, pp. 185–197.
- [221] D. Mohanty *et al.*, “Modification of Ni-Rich FCG NMC and NCA Cathodes by Atomic Layer Deposition: Preventing Surface Phase Transitions for High-Voltage Lithium-Ion Batteries,” *Sci. Rep.*, vol. 6, p. 26532, May 2016, doi: 10.1038/srep26532.
- [222] Woodbank Communications Ltd., “Battery Performance Characteristics.” [Online]. Available: <https://www.mpoweruk.com/performance.htm>. [Accessed: 21-Jun-2021].
- [223] N. Wagner, “Electrochemical Impedance Spectroscopy,” *PEM Fuel Cell Diagnostic Tools*. CRC Press, pp. 37–70, 25-Aug-2011, doi: 10.1201/b111100-5.
- [224] Y. Feng, K.-S. Siow, W.-K. Teo, K.-L. Tan, and A.-K. Hsieh, “Corrosion Mechanisms and Products of Copper in Aqueous Solutions at Various pH Values,” *CORROSION*, vol. 53, no. 5, pp. 389–398, May 1997, doi: 10.5006/1.3280482.
- [225] J. Wang *et al.*, “Strategies towards the challenges of zinc metal anode in rechargeable aqueous zinc ion batteries,” *Energy Storage Mater.*, vol. 35, pp. 19–46, Mar. 2021, doi: 10.1016/j.ensm.2020.10.027.
- [226] R. Hausbrand *et al.*, “Fundamental degradation mechanisms of layered oxide Li-ion battery cathode materials: Methodology, insights and novel approaches,” *Mater. Sci. Eng. B*, vol. 192, pp. 3–25, Feb. 2015, doi: 10.1016/j.mseb.2014.11.014.
- [227] HyperPhysics, “Resistance and Resistivity.” [Online]. Available: <http://hyperphysics.phy-astr.gsu.edu/hbase/electric/resis.html>. [Accessed: 22-Jun-2021].
- [228] F. Wang *et al.*, “Does Polarization Increase Lead to Capacity Fade?,” *J. Electrochem.*

Soc., vol. 167, p. 090549, Jun. 2020, doi: 10.1149/1945-7111/ab956b.

- [229] National Institute for Occupational Safety and Health, “Preventing Adverse Health Effects from Exposure to: Dimethylformamide (DMF) ,” *DHHS (NIOSH)*, 01-Sep-2014.
[Online]. Available: <https://www.cdc.gov/niosh/docs/90-105/>. [Accessed: 27-Jun-2021].
- [230] J. G. G. de Farias, R. C. Cavalcante, B. R. Canabarro, H. M. Viana, S. Scholz, and R. A. Simão, “Surface lignin removal on coir fibers by plasma treatment for improved adhesion in thermoplastic starch composites,” *Carbohydr. Polym.*, vol. 165, pp. 429–436, Jun. 2017, doi: 10.1016/j.carbpol.2017.02.042.
- [231] S.-P. Rwei, T.-F. Way, W.-Y. Chiang, and S.-Y. Pan, “Effect of tacticity on the cyclization of polyacrylonitrile copolymers,” *Colloid Polym. Sci.*, vol. 295, pp. 803–815, May 2017, doi: 10.1007/s00396-017-4062-4.

Appendices

Appendix A Calculation of Surface-to-Volume Ratio

These calculations demonstrate the increase of surface area when a cube with 1 cm sides is broken down to 10^{21} cubes with 1 nm sides (same volume as cube with 1 cm sides) – see section 1.4 for the application of such property in our work.

$$\text{same volume: } 1 \text{ cm}^3 = 1 \text{ cm}^3 \times \frac{1 \text{ m}^3}{(100)^3 \text{ cm}^3} \times \frac{1 \text{ nm}^3}{(10^{-9})^3 \text{ m}^3} = 10^{21} \text{ nm}^3$$

$$\text{surface area of one nm cube: } 6 \times 1 \text{ nm}^2 = 6 \text{ nm}^2$$

$$= 6 \text{ nm}^2 \times \frac{(10^{-9})^2 \text{ m}^2}{1 \text{ nm}^2} \times \frac{(100)^2 \text{ cm}^2}{1 \text{ m}^2} = 10^{-14} \text{ cm}^2$$

$$\text{for } 10^{21} \text{ cubes, we have: } 10^{21} \times 10^{-14} = 10^7 \text{ cm}^2$$

Appendix B Normalized FTIR Peak Values

To observe the peak variation more clearly, FTIR plots of different temperatures are overlaid in Fig B.1. Furthermore, the normalized values in Tab B.1 support the observation in Fig B.1.

These normalized values are calculated based on the ratio of each peak with respect to peak 6 in Figure 3.7.

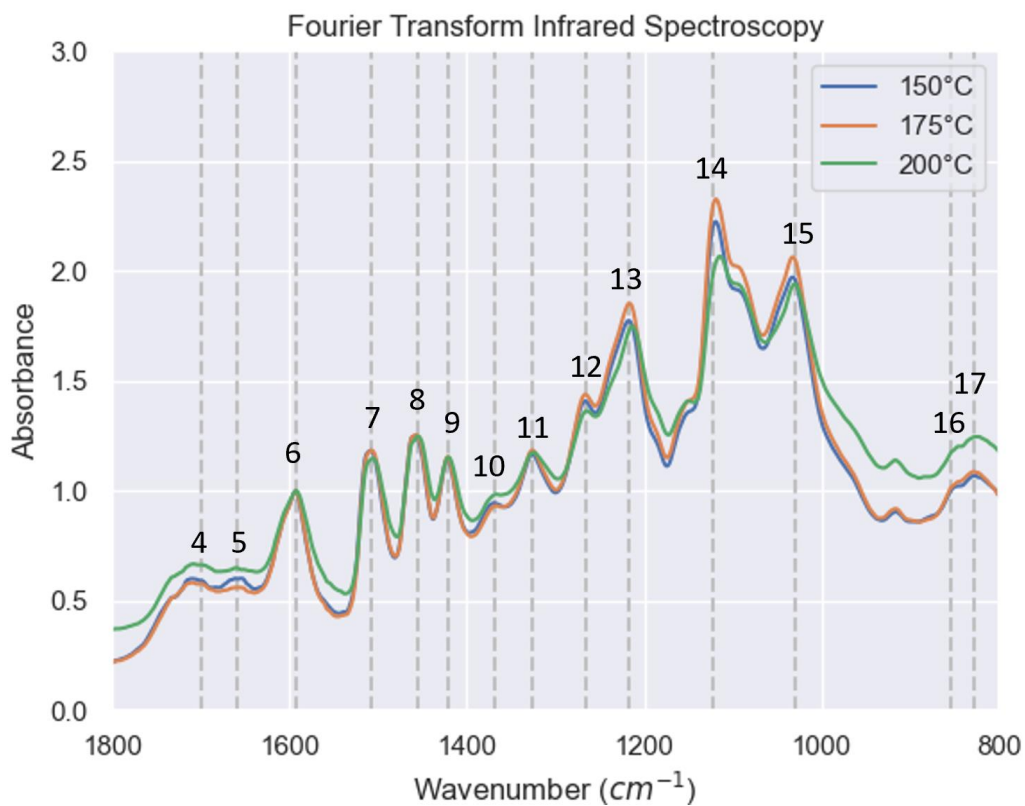


Fig B.1 Overlaid FTIR plots of 150, 175, and 200 °C samples.

Tab B.1 Normalized FTIR peak values

Num in Figure 3.7	Peak Wavenumber (cm ⁻¹)	150 °C	175 °C	200 °C
1	3411	0.6	0.52	0.56
2	2920	0.71	0.56	0.76
3	2852	0.58	0.48	0.68
4	1700, 1711	0.56	0.58	0.67
5	1659	0.61	0.56	0.66
6	1593	1	1	1
7	1508	1.19	1.19	1.16
8	1456	1.25	1.26	1.25
9	1421	1.15	1.16	1.15
10	1369	0.95	0.93	0.98
11	1327	1.17	1.19	1.17
12	1265	1.41	1.45	1.37
13	1217	1.78	1.86	1.76
14	1122	2.23	2.33	2.08
15	1030	1.98	2.07	1.94
16	~ 854	1.01	1.02	1.19
17	~ 829	1.08	1.09	1.25

Appendix C Cross Section of Carbon Paper Coated with MnO₂

Fig C.1, as discussed in section 5.3.6, demonstrates that the MnO₂ penetrates through the carbon paper, since the carbon fibers are surrounded by the active MnO₂.

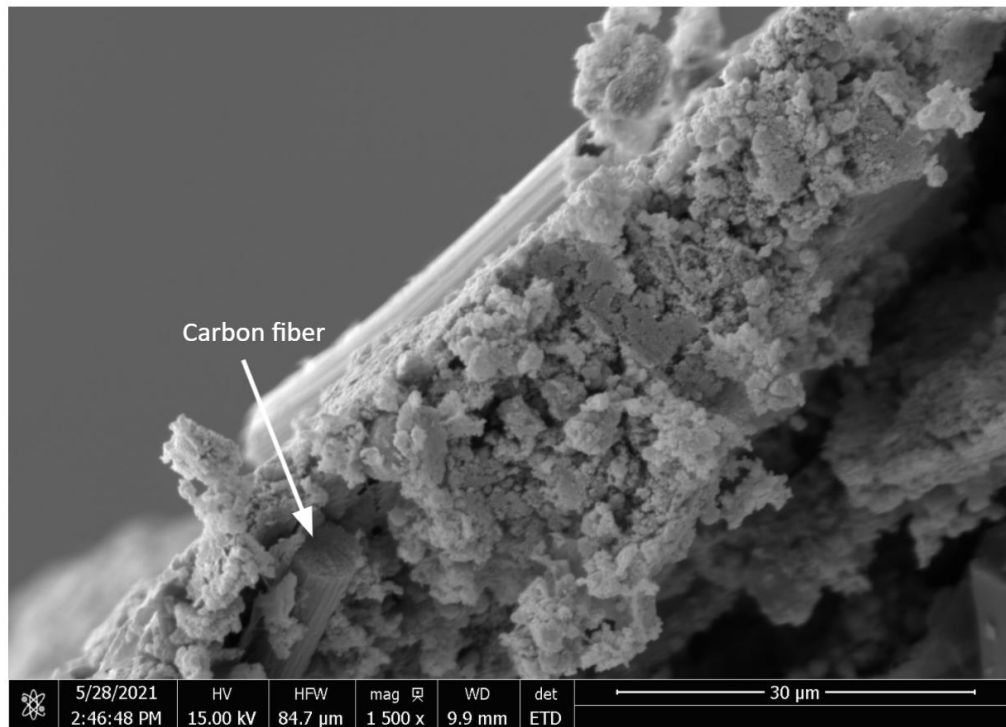


Fig C.2 Cross section of the carbon paper with MnO₂

Appendix D 200 °C Cycle Life

Capacity retention is 8.9 % over 1400 cycles for the 200 °C lignin battery. This battery reaches 80% of its initial capacity in only 13 cycles (Fig D.1), performing worse compared to 175 °C and carbon paper current collectors (see section 5.4 and 5.3.4). This is likely due to the high content of copper on its back (Tab D.1 and Fig D.2).

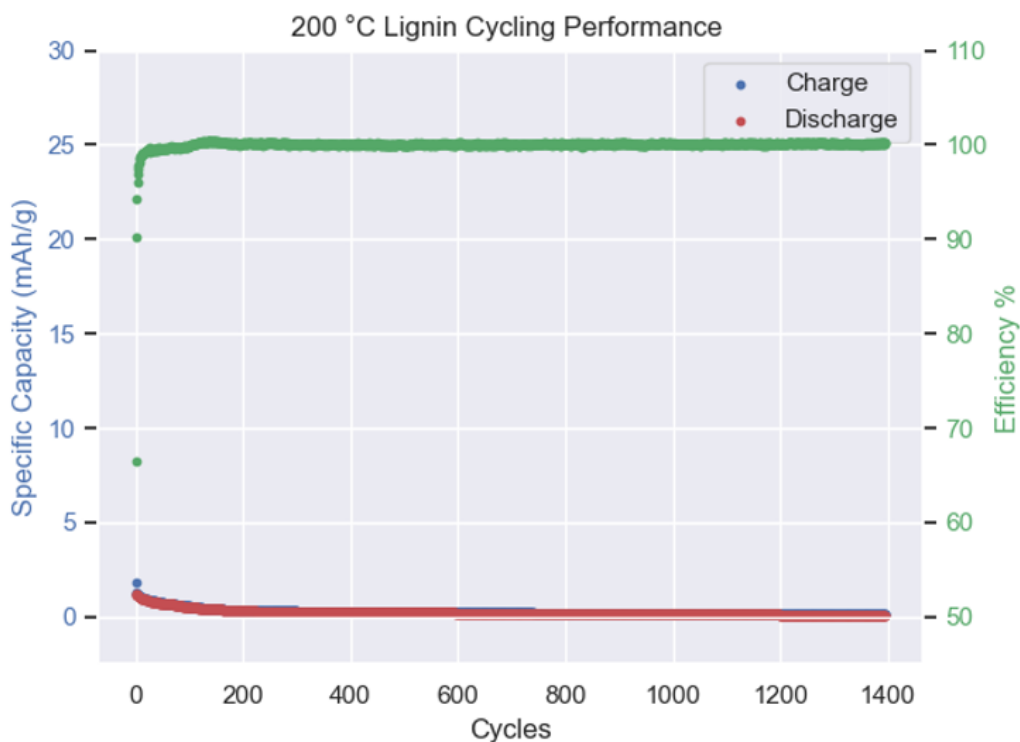


Fig D.1 Cycling performance of 200 °C lignin at 200 mA/g.

Tab D.1 EDS elemental mass % on the back of deposited MnO₂ on copper plated 200 °C lignin.

Elements	Mass % on the back of plated 200 °C lignin brush-coated with MnO ₂
Carbon	0.96
Copper	89.87

Manganese	2.42
Oxygen	5.70
Palladium	1.06

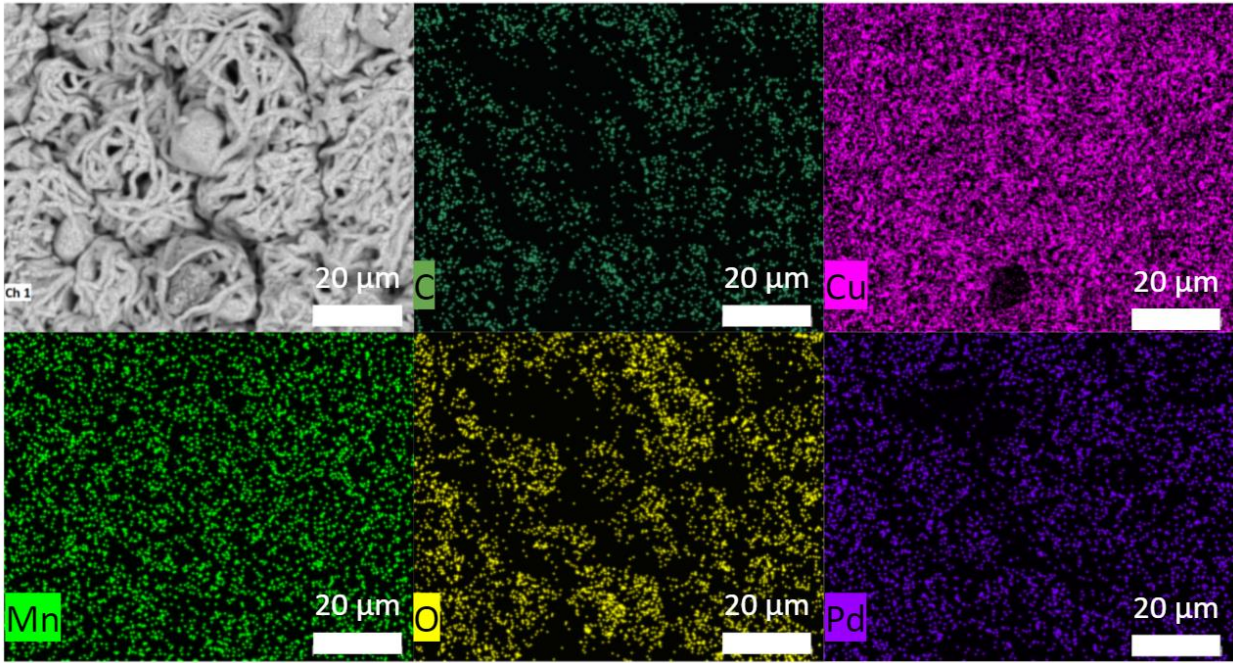


Fig D.2 EDS elemental mapping of deposited MnO₂ on copper plated 200 °C lignin on the back.

Appendix E Control Sample: PAN-co-MA

As a control sample for electroless copper plating solution (see Table 4.4) and the resulting conductivity comparison, polyacrylonitrile-co-methyl-acrylate (PAN-co-MA) is chosen in accordance with ref. [72]. PAN-co-MA is far more flexible than lignin (Fig E.1).

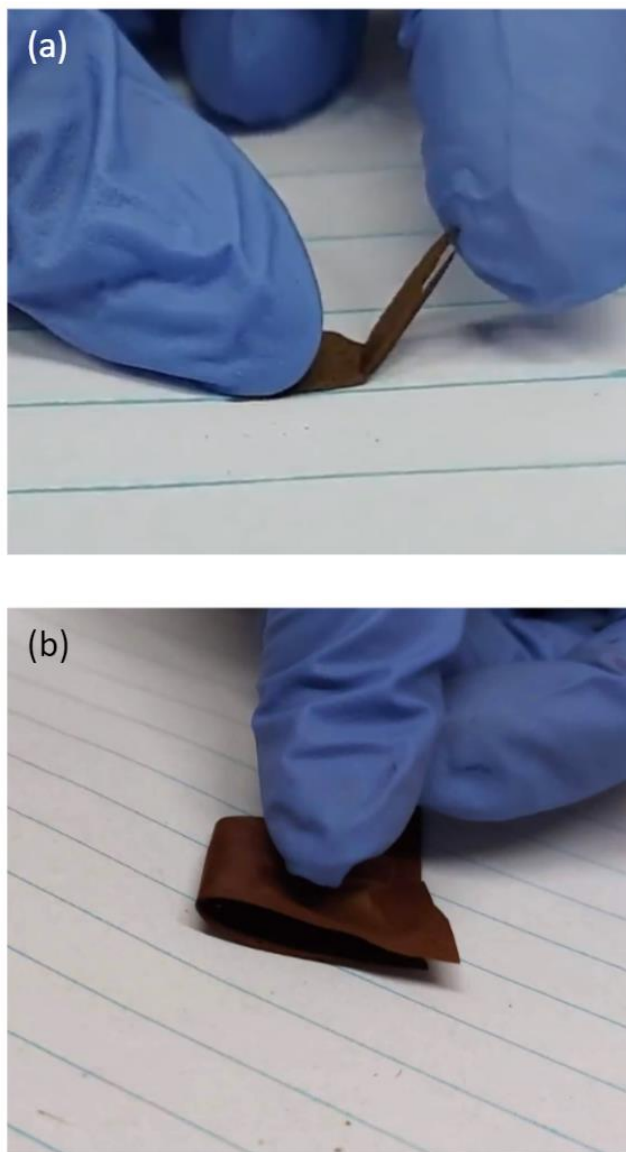


Fig E.1 Flexibility of (a) thermostabilized lignin at 175 °C, and (b) thermostabilized PAN-co-MA at 250 °C.

E.1 Morphology of Copper Plated PAN-co-MA

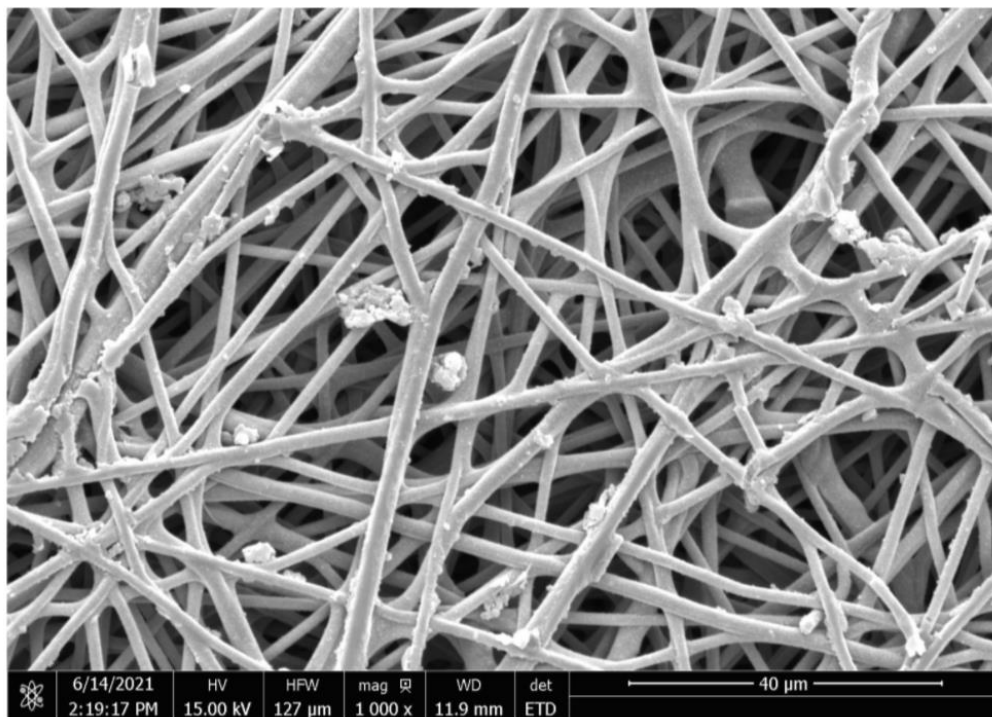


Fig E.2 SEM images of copper plated 250 °C PAN-co-MA (5-min sonication and 0.05 mL/mL solution of formaldehyde after 2.5 hrs).

E.2 Energy Dispersive Spectroscopy of Copper Plated PAN-co-MA

Tab E.1 EDS elemental mass % on the surface of copper plated 250 °C PAN-co-MA.

Element	PAN-co-MA-Pd Plated (2.5 hrs, 5 min sonication, 0.05 mL/mL solution of formaldehyde) Mass %
Carbon	12.08
Oxygen	1.11
Copper	86.81

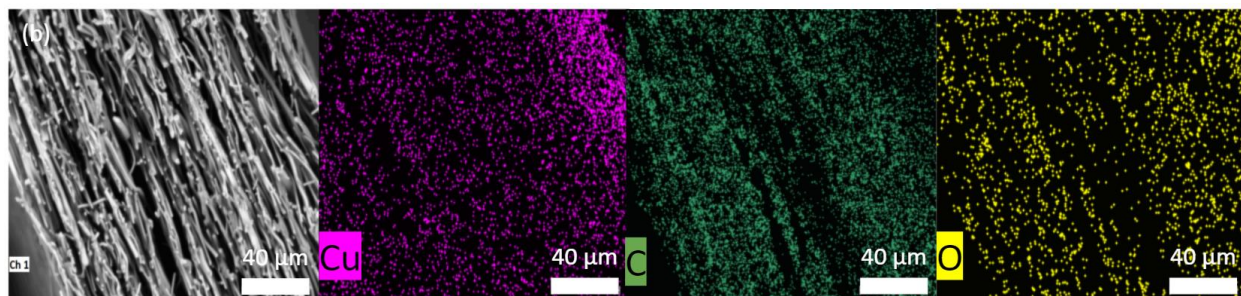
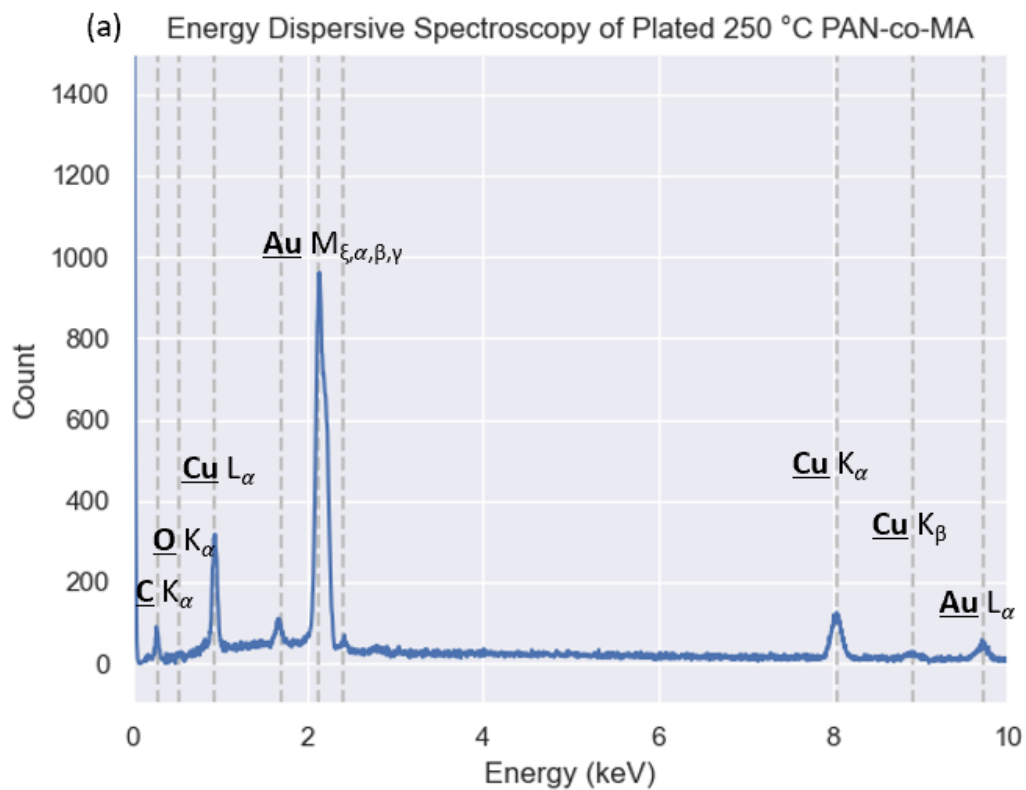


Fig E.3 EDS of copper plated 250 °C PAN-co-MA cross section. (a) spectrum on the surface. (b) elemental mapping. C_K α , O_K α , Cu_L α , Au_M, Cu_K α , Cu_K β , Au_L α values are from ref. [167], [168], [186]

E.3 X-Ray Diffraction of Copper Plated PAN-co-MA

First peak is from (101) plane of PAN-co-MA [231].

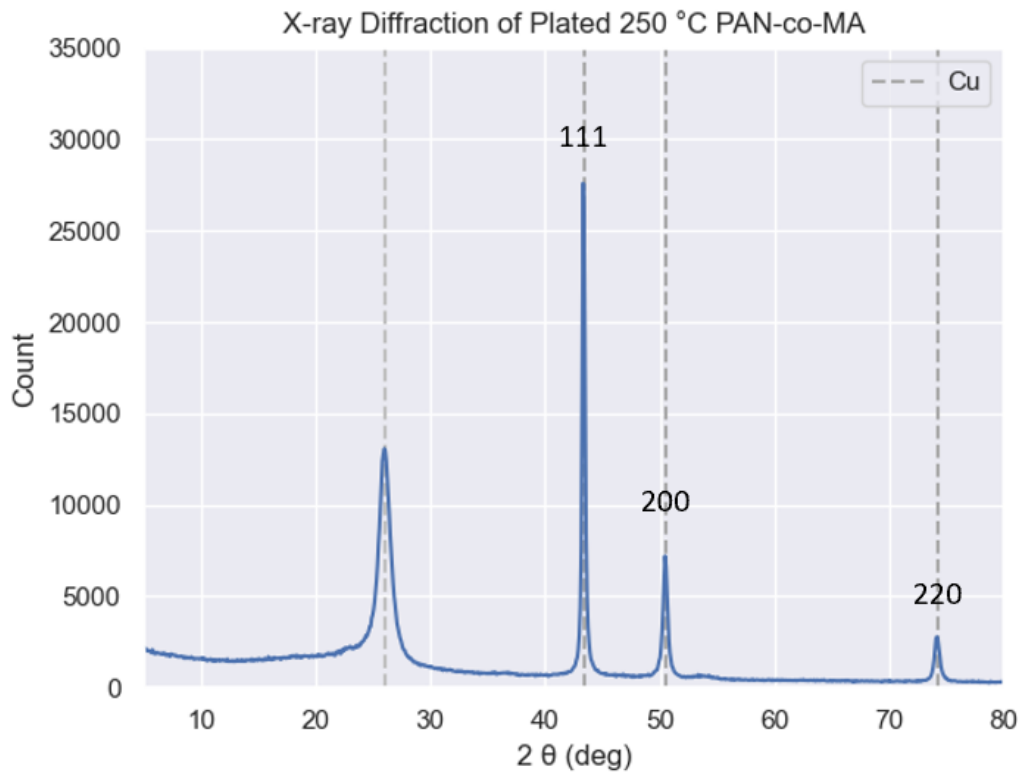


Fig E.4 XRD of plated 250 °C PAN-co-MA.